January 2015

Photonic Metasurfaces for Spatiotemporal and Ultrafast Light Control

Amr Shaltout
Purdue University

Graduate School Form 30
(Revised 08/14)

PURDUE UNIVERSITY
GRADUATE SCHOOL
Thesis/Dissertation Acceptance

This is to certify that the thesis/dissertation prepared

By Amr Shaltout

Entitled:
Photonic Metasurfaces for Spatiotemporal and Ultrafast Light Control

For the degree of Doctor of Philosophy

Is approved by the final examining committee:

VLADIMIR M. SHALAEV

ALEXANDER V. KILDISHEV

ALEXANDRA BOLTASSEVA

EVGUENI E. NARIMANOV

To the best of my knowledge and as understood by the student in the Thesis/Dissertation Agreement, Publication Delay, and Certification/Disclaimer (Graduate School Form 32), this thesis/dissertation adheres to the provisions of Purdue University's "Policy on Integrity in Research" and the use of copyrighted material.

Approved by Major Professor(s): VLADIMIR M. SHALAEV

Approved by: V. Balakrishnan 11/24/2015

Head of the Department Graduate Program Date

PHOTONIC METASURFACES FOR SPATIOTEMPORAL AND ULTRAFAST LIGHT CONTROL

A Dissertation

Submitted to the Faculty

of

Purdue University

by

Amr Mohammad Emadeldin Abdelmaksoud Shaltout

In Partial Fulfillment of the

Requirements of the Degree

of

Doctor of Philosophy

December 2015

Purdue University

West Lafayette, Indiana

To my late father, my mother, and my wife and kids

ACKNOWLEDGEMENTS

First and foremost, I would like to express my sincere gratitudes to my advisor Professor Vladimir Shalaev for his encouragement and immense support. His sound advices and the research environment he builds makes strong independent researchers that can also understand and describe the big picture of the research. I also give my special thanks to Professor Alexander Kildishev for his valuable efforts, detailed supervision, patience and time in reviewing my work. I also would like to thank Professor Alexandra Boltasseva for her strong support, very valuable care and important advices about the work. I also appreciate the role of Prof Evgenii Narimanov in developing innovative approaches in understanding the theory which I used throughout my research.

I would like also to thank all the members of the group for supporting me during these years. Jingjing Liu and Jongbum Kim gave a lot of support in fabrication and experimentation. Xingjie Ni and Satoshi Ishi helped me through learning some of the tools. Gururaj Naik, Naresh Emani, Jieran Fang and Urcan Guler gave me helpful advices in many situations. Nathaniel Kinsey, Rohith Chandrasekar and Clayton Devault proofread many of my manuscripts and provided important comments. Thanks for the rest of the team for helpful good work throughout my thesis work.

Finally and most importantly, I would like to express my appreciation to my parents for their love, support and encouragement all the time, and to my wife and kids for support, patience and for being a joyful part of my life throughout this journey.

TABLE OF CONTENTS

Page

LIST OF TABLES

LIST OF FIGURES

Figure Page

Figure Page

Figure Page

Figure Page

Figure Page

Figure Page

ABSTRACT

Shaltout, Amr M. Ph.D., Purdue University, December 2015. Photonic Metasurfaces for Spatiotemporal and Ultrafast Light Control. Major Professors: Vladimir Shalaev and Alexander Kildishev.

The emergence of photonic metasurfaces - planar arrays of nano-antennas - has enabled a new paradigm of light control through wave-front engineering. Space-gradient metasurfaces induce spatially varying phase and/or polarization to propagating light. As a consequence, photons propagating through space-gradient metasurfaces can be engineered to undergo a change to their momentum, angular momentum and/or spin states.

In our study, we implement metasurface-based devices that break the spin symmetry of light to obtain Photonic Spin Hall Effect (PSHE). We utilized PSHE to design a real-time circular dichroism spectrometer, a device vital in bio-sensing, and an optical rotator used in secure quantum communications. In addition, we developed metasurface based Fabry–Pérot nano-cavities, which go beyond the diffraction limit of light, a requirement to enhance photonic spontaneous emission using the Purcell effect.

In addition, we demonstrate that the field of flat photonics is further empowered by utilizing time-gradient metasurfaces with dynamic responses to propagating light. A new genus of optical devices and physical effects can be realized. Photons experience inelastic interactions with time-varying metasurfaces resulting in a Doppler-like wavelength-shift. Furthermore, Snell's relations are modified to a more universal form not limited by Lorentz reciprocity, hence meeting all the requirements to build magnetic-free optical isolators.

Finally, we construct the concept of ultrafast metasurfaces. We integrate spatial interference methodology delivered by metasurfaces and temporal interference of phase-

locked frequency-comb provided by ultrafast technology. This leads to generation of coherent 4D space-time optical patterns, which is implemented to achieve ultrafast laser beam steering over hundred-picosecond scale.

1. INTRODUCTION

1.1 Optical metamaterials and metasurfaces

Optical metamaterials are artificial materials which are tailored to achieve optical properties that transcend properties of natural materials, by engineering light-matter interaction at the structural level rather than the atomic\molecular level. These include negative index of refraction materials[1-4], metamagnetics[5, 6], perfect lenses[7], invisibility cloaks[8, 9], hyperlenses[10-12], optical black holes[13, 14] and hyperbolic metamaterials[15-17].

There has been a tremendous progress over the last decade to implement these kinds of 3D metamaterials. However, the realization of commercial devices for the hoped-for applications seems a long-way off. The development of full scale technology of metamaterials is highly challenged by the very high dissipative losses, cost-ineffective fabrication and very complicated integration[18]. These factors are delaying industrial production of metamaterial based optical devices.

Two complementary research approaches are recently developed to cope with these challenges on the structural level as well as the material level. For the structural development, the rise of optical metasurfaces (2D metamaterials)[19-22] have dramatically reduced the fabrication complexity for metamaterials being more readily assembled and suitable for on-chip application. In addition, the reduced dimensionality of metasurfaces has enabled the potential for new physical effects which do not have volumetric counterparts, such as the relaxation of Snell's relation[23]. Furthermore, planar structures offer a simpler approach for implementing tunable devices, as it becomes possible to reconfigure the whole structure and implement modulating schemes with planar layers. Simultaneously, a complementary research approach is going on to

---

This thesis contains some text and figures which have been used with permission from the author's research publications especially from references [42, 49, 56, 120, 126] (© 2013, 2014, 2015 OSA), reference [26] (© 2014 ACS), and reference [40] (© 2013 SPIE)

develop new plasmonic materials along with noble metals such as transparent conducting oxides and transition metal nitrides[24]. They provide additional properties such as tolerating difficult operating environment and very high temperatures, and they can be fabricated using CMOS compatible processes. So far, noble metals are used in most of metasurface applications because they provide higher quality of plasmonic resonances in the visible and near infrared wavelength regimes. Nevertheless, recent results have shown that Zirconium Nitride (ZrN) can attain optical properties similar to that of gold [25] which can pave the way to integrate all the benefits of optical metasurfaces and alternative plasmonic materials.

In this work, we are focused on structural development of metasurfaces and their various functional operations. Metasurfaces consist of planar arrays of nano-structured antennas which induce spatially varying phase and/or polarization to propagating light. As a consequence, photons propagating through metasurfaces can be engineered to undergo a change to their momentum, angular momentum and/or spin state. This has led to a relaxation of Snell's law [19], a pivotal relation in optical engineering, and has enabled a whole new family of flat optical devices. Below is a brief discussion of the most common metasurface based applications that are implemented through controlling local phase and/or polarization.

1.2 Phase-gradient metasurfaces

Optical metasurfaces added an extra degree of control over light flow by introducing discontinuous change to the phase of light in contrast to the accumulative volumetric response. The space-gradient of the phase across the metasurface induces a discontinuity in the momentum of reflected and refracted photons. This led to relaxation of Snell's relation according to the following formulas[19]:

$$k_{\mathrm{s},x} = k_{\mathrm{i},x} + \partial\psi_{\mathrm{ms}} \big/ \partial x, \;\; \mathrm{s} = \{\mathrm{r},\mathrm{t}\}, \tag{1.1}$$

where $k_{i,x}$, $k_{r,x}$ and $k_{t,x}$ are the x-components of the wave-numbers of incident, reflected and transmitted waves, respectively. And ψ_{ms} is the phase-shift induced by the metasurface.

These capabilities of modifying such an essential law of optical design unleashed a whole new class of ultrathin flat devices. By judiciously locating nano-antennas with varying phase response across the metasurface, their holographic far field interference can be designed to obtain an optical response at will. They have been successfully implemented to perform light bending[19, 20, 26], flat lenses[27-29] and holographic imaging[30-34]. Their ability to induce tangential photonic momentum to photons enabled the generation of vortex beam which carry orbital angular momentum using deep subwavelength layer[19, 35].

1.3 Polarization-gradient metasurfaces

In addition to space-gradient phase-shift metasurfaces, a lot of other interesting applications are obtained through metasurfaces with a space-gradient polarization discontinuity. Using nano-antenna structures with broken symmetry, successful implementations of these metasurfaces have been demonstrated to obtain various devices including quarter-wave plates[36, 37], half-wave plates[38, 39], as well as bianisotropic[40-42] and chiral metasurfaces[43-49].

Special interest is also given to circular polarizations (optical spins) due to the simplicity of obtaining continuous values of phase-shift ranging from 0 to 2π just using Pancharatnam-Berry phase[50] by adjusting the orientation angle of anisotropic nano-structures or nano-antennas. This method has the advantage of using oriented replicas of a single design of antenna, and hence, the functionality is robust against fabrication's tolerances in dimensions and/or material properties as long as any variation is uniform along the whole antenna array. In addition, the Pancharatnam-Berry phase has opposite signs for left-(LCP) and right-circular polarizations (RCP) which has been utilized to obtain the photonic spin Hall effect (PSHE) – the effect of spatially separating LCP and RCP photons. Metasurfaces utilizing the PSHE have been demonstrated many times in

literature[21, 22, 51-53], and some other devices are developed based on this effect like dual polarity lenses[29]. Additional effects have also been developed based on spin dependent performance like optical rotation[49] which requires differential optical delays between LCP and RCP.

The control of metasurfaces over polarization motivated the implementation of polarization sensing and spectroscopy devices such as the measurement of Stokes' parameters[54, 55] and a circular dichroism spectrometer[56] which measures the spectrum of the differential response between LCP and RCP. These kinds of measurements are important for bio-chemical applications where chiral structures, which have a differential response with respect to the optical spin, are very prominent. Metasurfaces have been shown to provide simple, compact, and efficient platform for these vital applications.

With such a wide variety of impactful devices being demonstrated using space-gradient metasurfaces, there has been a strong interest to optimize these devices in terms of power efficiency so as to push their impact towards obtaining commercial devices.

1.4 Power-efficient metasurfaces

For metasurfaces, there are two figures of interest. One is the phase coverage, and second is the power efficiency. We ideally would like to design metasurfaces with full 2π phase coverage with large power efficiency. 2π phase coverage cannot be achieved by plasmonic resonances since they provide only π phase coverage. V-shaped and geometric phase-shift methods have been used to have 2π phase coverage. However, they are still limited by their power efficiencies. The major part of unused power is not due to metallic losses as in the case of multilayered 3D metamaterials, but mostly due to poor coupling efficiency of the single layered plasmonic antennas to the required phase-controlled mode called the anomalous mode. This results in most of the power being unchanged by the metasurface (called the normal mode).

Different approaches have been used to overcome this problem including Huygens' surfaces[26, 57], gap-plasmonic metasurfaces[37, 58-62], and dielectric metasurfaces[63-

65]. Huygens' surfaces control light directivity by using nanostructures that control electric and magnetic dipoles simultaneously to suppress reflection. Gap-plasmonic metasurfaces use a metal/dielectric/metal sandwich that excites a slow gap-plasmonic wave that induces a phase shift along the nano-antenna dimensions before they couple back to reflected propagating waves. Dielectric metasurfaces avoid using lossy metals by using high-index dielectric nanostructures that can excite both electric and magnetic dipoles that can be independently controlled to minimize reflection and obtain a transmission near unity. As a result, the progress in the metasurface research is going forward towards providing very compact and power-efficient nanophotonic devices.

1.5 Reconfigurable Dynamic metasurfaces

Optical metasurfaces provide a suitable technology platform towards the realization of ultra-compact, two dimensional, reconfigurable optical devices that can be modulated using mechanical, electrical, or optical means. Control over the optical properties of the metasurface will enable applications such as beam steering[66-71], Laser remote sensing[72, 73], axial scanning of focusing lenses[74, 75], tunable selective filtering, and optical modulation. There have been some demonstrations of reconfigurable technologies and efforts are still being carried out in order to obtain stable real-time dynamic operation of metasurfaces.

Technologies that are being developed to control optical operations can be classified into those utilizing mechanical, electrical, or optical modulation techniques. Many technologies are developed for mechanical reconfigurability. These include metasurfaces with structural tunability[76-79] and stretchable substrates. Strechable films[80-88] have been developed in order to enable flexible shaping of the substrate. Another demonstration of flexible metasurfaces has shown tunability of filtering colors[89]. This technology can also be utilized to obtain dynamic beam applications such as beam steering or axial scanning. Metasurfaces fabricated on top of a stretchable substrate can have a variable periodicity upon stretching and relaxing the substrate. By changing the periodicity of a beam bending metasurface[19, 20], the deflection angle of the output

beam is varied. Therefore, by applying an oscillating force to the stretchable substrate, it's possible to get a real-time beam scanning. Similarly, building a meta-lens on a flexible substrate enables axial scanning.

Reconfigurable nanoantennas[90, 91] is an alternative approach to using stretchable substrates. Reconfigurable microfluidic metasurfaces are also obtained either by utilizing channels of liquid polymer[92] or liquid metal[93-95]. Antennas can be reconfigured in a way that is exactly similar to changing the periodicity of the substrate leading to beam steering and other dynamic optical responses. Other morphological nanostructures such as kirigami structures[96-101] can also be used and they provide much larger dynamic range than stretchable metasurfaces.

Using electrical means to tune metasurfaces is of special interest because it easily connects to industrial technologies. Electrically tunable metasurfaces can be obtained through utilizing a tunable varactor based impedance[68, 102-104], but this is limited to radio-frequencies, microwaves and possibly terahertz regimes. There have been demonstrations of modulating optical properties of graphene[105-113] which can operate in the far infrared. Operation in the near infrared and visible regimes can be possible by through free-carrier modulation[114, 115] which went to visible regime through utilizing transparent conducting oxides[116].

Optical modulation is by far the fastest modulation technology. Ultrafast modulation is critical to obtain interesting physical effects to be discussed in the following section. Ultrafast modulation optical modulation of terahertz metamaterials has been successfully implemented[115, 117, 118]. In these regards, recent results have demonstrated that optical modulation of Aluminum-doped Zinc Oxide (AZO) resulted in free carrier modulation with sub-picosecond carrier dynamics[119] at the telecommunications wavelength. The operation was near the epsilon-near-zero (ENZ) wavelength enabling a large optical response for a small change in the optical properties.

So far, most undergoing efforts to obtain dynamic metasurfaces are motivated by implementing tunable versions of static metasurfaces. However, recent studies have shown that time-varying metasurfaces enabled new physical effects not present in static metasurfaces, and new sets of devices are possible only with dynamic metasurfaces.

1.6 Time-gradient metasurfaces and non-reciprocity

The impact of reconfigurable metasurfaces exceeds implementing tunable optical devices. It has been recently demonstrated that the field of flat photonics is further empowered by utilizing time-gradient metasurfaces with dynamic responses to propagating light. A new genus of optical devices and physical effects can be realized provided one can overcome some fundamental limitations of metasurfaces with space-gradient alone[120, 121].

With the inception of metasurfaces with space-gradient phase discontinuity[19], Snell's law has been generalized to include a discontinuity in the tangential momentum of propagating photons. This enabled engineering angles of reflection and refraction at will with flat, ultra-thin metasurfaces. It have been have shown that by introducing a dynamic (i.e. temporal) change to the phase-discontinuity, the photon energy conservation constraint is eradicated, and Snell's law can be modified to an even more universal form not limited by Lorentz reciprocity, hence, meeting all the requirements for building magnetic-free optical isolators[120]. Furthermore, light experiences inelastic interaction with time-gradient metasurfaces, which modifies photonic energy eigenstates and results in a Doppler-like wavelength shift. Another study demonstrated non-reciprocal electromagnetic induced transparency (EIT) effect[121]. A space-gradient metasurface was designed to obtain a narrow EIT transparency window within an opaque bandwidth. Then it's shown that non-reciprocity occurs by utilizing space-time gradient metasurface causing the center frequency of the EIT window to change with different incident directions. This technique can be implemented to build ultrathin optical isolators.

1.7 Overview of the thesis

In this thesis, several topics regarding optical metasurfaces are covered. In Chapter 2, a bianisotropic model for plasmonic nano-antennae is developed. The nano-antenna is the unit structure of the metasurface, and this model provides an in-depth understanding of the light-matter interaction inside the metasurface. The model also accounts for the role

of symmetry breaking inside the nanostructure and its effect on the waves. It can also be used to develop high speed numeric solvers. By replacing the detailed nano-structures of the plasmonic antennae with homogeneous bi-anisotropic tiles, meshing is dramatically reduced. An FDFD solver is developed using the bi-anisotropic material model. A simulation is performed to a phase gradient metasurface with the bi-anisotropic approximation, and good agreement is obtained with a finite element simulation of the exact nano-sturucture.

In Chapter 3, we design and implement spin-dependent metasurfaces to operate as a circular dichroism spectrometer. These operations are obtained through phase gradient metasurfaces which have a differential response to right and left circularly polarized incident light. To overcome the power efficiency limitation, gap-plasmonic antennas are used. Their dimensions are optimized such that all the reflected power of circularly polarized light is controlled by the geometric phase induced by the orientation of the antennas. This has enhanced the power efficiency by an order of magnitude. A circular dichroism spectrometer is also implemented using this technology with 40% power efficiency in the NIR region.

In Chapter 4, we design and implement a metasurface based optical rotator. The chiral response in these metasurfaces is not achieved using chiral antennas, but rather obtained through the coherent response of the array. Successful rotation of linearly polarized light by 45^0 is achieved using a metasurface with $\lambda/50$ thickness. The structure is also implemented using gap-plasmonic antennas to enhance the power efficiency by an order of magnitude. A circular dichroism spectrometer is also implemented using this technology with 40% power efficiency in the NIR region.

In Chapter 5, we design novel nano-cavities with metasurface based mirrors. This novel approach dramatically changes the constraints on the size and capabilities of conventional cavities. In conventional Fabry–Pérot cavities, a resonance is obtained through constructive interference of waves circling back and forth inside the cavity. It is required that the round trip phase propagation be an integer multiple of 2π to exhibit resonant behavior. This means that the minimum size of the cavity cannot go below $\lambda/2$. It also allows resonances only at higher frequencies which are integer multiple of the

fundamental frequency. Replacing one of the Fabry–Pérot mirrors with a reflecting metasurface totally changes the resonance condition. The metasurface can cause a large abrupt change in the phase shift of the reflected wave, decreasing the amount of required phase accumulated by propagation inside the cavity. As a result, the length of the cavity can easily go below $\lambda/2$. Furthermore, by tailoring the dimensions of the metasurface elements, the nano-cavities can be designed to resonate at multiple wavelength which need not be integer multiples of each other, and are possible to be tailored to any values.

In Chapter 6, the impact of time-gradient metasurfaces in developing non-reciprocal Snell's relation of light flow is studied. Snell's law relates the angles of incidence and refraction for light passing through an interface between two media. It is built on two fundamental constraints: the conservation of tangential momentum and the conservation of energy. By relaxing the classical Snell's law photon momentum conservation constraint when using space-gradient phase discontinuities, optical metasurfaces enabled an entirely new class of ultrathin optical devices. Here, we show that by eradicating the photon energy conservation constraint when introducing time-gradient phase discontinuities, we can further empower the area of flat photonics and obtain a new genus of optical devices. With this approach, classical Snell's relations are developed into a more universal form not limited by Lorentz reciprocity, hence, meeting all the requirements for building magnetic-free optical isolators. Furthermore, photons experience inelastic interaction with time-gradient metasurfaces, which modifies photonic energy eigenstates and results in a Doppler-like wavelength shift. Consequently, metasurfaces with both space- and time-gradients can have a strong impact on a plethora of photonic applications and provide versatile control over the physical properties of light.

In Chapter 7, we study integrating metasurface based devices with ultrafast technology to enable ultrafast laser beam steering. We integrate spatial interference methodology delivered by metasurfaces and temporal interference of phase-locked frequency-comb provided by ultrafast technology to obtain a time-dependent metasurface

response which is ultrafast. This methodology enables beam steering with a hundred picosecond period which is four orders of magnitude faster than state-of-the-art beam steering technologies based on phase-modulating array elements.

2. BIANISOTROPIC HOMOGENIZATION OF METASURFACES

In this work, ultrathin metamaterial layers are modeled by a homogeneous bi-anisotropic film to represent various kinds of broken symmetries in photonic nanostructures, and specifically in optical metamaterials and metasurfaces. Two algorithms were developed to obtain the electromagnetic (EM) wave response from a metasurface (direct solver) or the metasurface parameters from the EM wave response (inverse solver) for a bi-anisotropic, subwavelength-thick nanostructured film. The algorithm is applied to two different metasurfaces to retrieve their effective homogeneous bi-anisotropic parameters. The effective layer of the same physical thickness is shown to produce the same response to plane wave excitation as the original metasurface.

2.1 Introduction

Metasurfaces have been used for manipulating light in a controllable manner using flat structures rather than 3D complicated structures. They provide their intended functionality through a 2D array of nano-antennae that change the phase and/or polarization of light passing through them. This technique has been used to implement important applications such as light bending [20, 23], flat lenses [27], circular polarizers [122], half-wave plates [38, 123], quarter wave plates [124, 125] and optical rotators[43, 44, 126]. In order to develop metasurfaces and fully analyze their functionalities, it is important to have an accurate and efficient model to describe the unit cell of the surface nanostructure. In this work, we have developed a model for metasurface layers with a thin, homogeneous, equivalent film. Using this framework, metasurface designers can then obtain insight on how best to use the unit-cell structures.

Most of metasurface designs depend on symmetry breaking in the nanostructure, such as rotational symmetry, mirror symmetry or directional symmetry. A bi-anisotropic model would be quite general and useful option for the homogenization of metasurface designs. The goal is to obtain a homogenous bi-anisotropic film that will generate the same values of the complex coefficients for reflection and transmission as those obtained by the real metamaterial structure. Homogenization using reflection and transmission coefficients has been used for permittivity and permeability retrieval [127], but non-physical dispersion relations may occur due to limitation of the model, and lack of representation of bi-anisotropy, chirality and spatial dispersion [128]. Bi-anisotropy has been used to account for directional asymmetry[129], and in this work a general bi-anisotropic tensor is used to account for bi-anisotropy, chirality and linear spatial dispersion. The model is only limited by higher order spatial dispersion terms, however, their effect will significantly decrease in thin films and the linear spatial dispersion term will dominate. Detailed discussions on the physical meaning of metamaterial constitutive parameters can be found in [128, 130]. The work is done by first solving for the transmission and reflection coefficients of a bi-anisotropic layer developing *a direct solver*. Then, it is solved for a bi-anisotropic film that accurately represents our structure, thus developing *an inverse solver*. After explaining the details of the process, the algorithm is implemented to homogenize two specific structures that are commonly used in metasurface applications.

2.2 Direct and Inverse Solvers

The first step in the homogenization process is to compute the complex reflection and transmission coefficients for a thin, bi-anisotropic film of known parameters. Table 1 clarifies the complex reflection and transmission coefficients (4-port S-parameters).

As shown in Table 2.1 and further illustrated in Fig. 2.1, the subscripts of S-parameters represent the output and input sides respectively (1 – superstrate, 2 – substrate), while their superscripts represent the polarization of the output and input

waves respectively. There also exist the other set of eight coefficients for the waves incident at the substrate side (side 2).

Table 2.1. Complex reflection and transmission coefficients.

			incidence side			
			superstrate		Substrate	
			E_{1+}^{x}	E_{1+}^{y}	E_{2-}^{x}	E_{2-}^{y}
scattering side	superstrate	E_{1-}^{x}	S_{11}^{xx}	S_{11}^{xy}	S_{12}^{xx}	S_{12}^{xy}
		E_{1-}^{y}	S_{11}^{yx}	S_{11}^{yy}	S_{12}^{yx}	S_{12}^{yy}
	substrate	E_{2+}^{x}	S_{21}^{xx}	S_{21}^{xy}	S_{22}^{xx}	S_{22}^{xy}
		E_{2+}^{y}	S_{21}^{yx}	S_{21}^{yy}	S_{22}^{yx}	S_{22}^{yy}

The co-polarized reflection relation is described by $S_{jj}^{qq}E_{j\pm}^{q} = E_{j\mp}^{q}$ using the complex co-polarized transmission coefficient S_{jj}^{qq}, where $q = \{\mathrm{x},\mathrm{y}\}$. In contrast, the cross-polarized reflection relation is described by $S_{jj}^{pq}E_{j\pm}^{q} = E_{j\mp}^{p}$ using the complex co-polarized reflection coefficient S_{jj}^{pq}, where $p = \{\mathrm{x},\mathrm{y}\}$ for $q = \{\mathrm{y},\mathrm{x}\}$. In the both cases (of co- or cross-polarized) reflections $j = 1$, for '+', or $j = 2$, for '-'. The co-polarized transmission relation is described by $S_{ij}^{qq}E_{j\pm}^{q} = E_{i\mp}^{q}$, where $q = \{\mathrm{x},\mathrm{y}\}$. The cross-polarized transmission is defined by $S_{jj}^{pq}E_{j\pm}^{q} = E_{j\mp}^{p}$, where $p = \{\mathrm{x},\mathrm{y}\}$ for $q = \{\mathrm{y},\mathrm{x}\}$. In both cases (either co- or cross-polarized) reflections $j = 1$, for '+', or $j = 2$, for '-'.

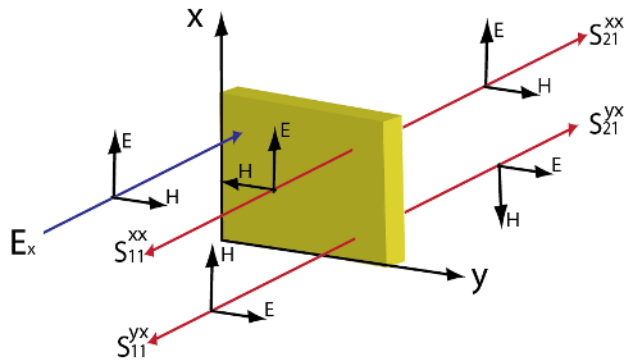

Fig. 2.1. Demonstration of co-polarized and cross-polarized reflection and transmission coefficients for an x-polarized input plane wave from the front size. The incident wave is indicated in blue, and the reflected and transmitted waves are in red. The direction of **E** and **H** fields are shown by arrows.

The electromagnetic (EM) waves propagating inside the bi-anisotropic structure satisfy the following material equation for the field components of a normally incident plane wave:

$$\begin{pmatrix} \mathbf{D} \\ \mathbf{B} \end{pmatrix} = \begin{pmatrix} \varepsilon_0 \boldsymbol{\varepsilon} & c^{-1}\boldsymbol{\xi} \\ c^{-1}\boldsymbol{\zeta} & \mu_0 \boldsymbol{\mu} \end{pmatrix} \begin{pmatrix} \mathbf{E} \\ \mathbf{H} \end{pmatrix} \tag{2.1}$$

where $\mathbf{D} = \begin{pmatrix} D_x & D_y \end{pmatrix}^T$, $\mathbf{E} = \begin{pmatrix} E_x & E_y \end{pmatrix}^T$, $\mathbf{B} = \begin{pmatrix} B_x & B_y \end{pmatrix}^T$, $\mathbf{H} = \begin{pmatrix} H_x & H_y \end{pmatrix}^T$, $\boldsymbol{\varepsilon} = \begin{pmatrix} \varepsilon_{xx} & \varepsilon_{xy} \\ \varepsilon_{yx} & \varepsilon_{yy} \end{pmatrix}$, $\boldsymbol{\mu} = \begin{pmatrix} \mu_{xx} & \mu_{xy} \\ \mu_{yx} & \mu_{yy} \end{pmatrix}$, $\boldsymbol{\xi} = \begin{pmatrix} \xi_{xx} & \xi_{xy} \\ \xi_{yx} & \xi_{yy} \end{pmatrix}$, $\boldsymbol{\zeta} = \begin{pmatrix} \zeta_{xx} & \zeta_{xy} \\ \zeta_{yx} & \zeta_{yy} \end{pmatrix}$. The parameters $\boldsymbol{\varepsilon}, \boldsymbol{\mu}$ are the relative permittivity and relative permeability tensors, and $\boldsymbol{\xi}, \boldsymbol{\zeta}$ are the bi-anisotropic tensors. The free space constants of permittivity ε_0, permeability μ_0 and speed of light c are used to normalize the model. We use tensors to represent the rotational asymmetry (anisotropy). The diagonal terms of $\boldsymbol{\xi}, \boldsymbol{\zeta}$ model the mirror asymmetry effect (chirality) and their off-diagonal terms are responsible for breaking the directional symmetry of the propagating wave. The eigenmodes excited inside the bi-anisotropic medium are in general elliptically polarized [131], and we cannot decouple the transverse-electric (TE) and the transverse-magnetic (TM) waves inside the film.

To solve for the eigenmodes of the system, we start from Maxwell's equations:

$$\nabla \times \begin{pmatrix} \mathbf{H} \\ -\mathbf{E} \end{pmatrix} = -\iota\omega \begin{pmatrix} \varepsilon_0 \boldsymbol{\varepsilon} & c^{-1}\boldsymbol{\xi} \\ c^{-1}\boldsymbol{\zeta} & \mu_0 \boldsymbol{\mu} \end{pmatrix} \begin{pmatrix} \mathbf{E} \\ \mathbf{H} \end{pmatrix} \tag{2.2}$$

using a time dependence of $e^{-\iota\omega t}$. Equation (2.2) can be formally rewritten as:

$$\frac{d}{dz}\mathbf{V} = \iota \mathbf{A}\mathbf{V} \tag{2.3}$$

where $\mathbf{V} = \begin{pmatrix} \mathbf{E} \\ \mathbf{H} \end{pmatrix}$, $\mathbf{A} = \omega \mathbf{N} \begin{pmatrix} \varepsilon_0 \boldsymbol{\varepsilon} & c^{-1}\boldsymbol{\xi} \\ c^{-1}\boldsymbol{\zeta} & \mu_0 \boldsymbol{\mu} \end{pmatrix}$, where $\mathbf{N} = \begin{pmatrix} \mathbf{0} & -\mathbf{n} \\ \mathbf{n} & \mathbf{0} \end{pmatrix}$, and $\mathbf{n} = \begin{pmatrix} 0 & -1 \\ 1 & 0 \end{pmatrix}$; it has a straightforward solution of:

$$\mathbf{V}(z) = e^{\iota \mathbf{A} z}\, \mathbf{V}\big|_{z=0} \tag{2.4}$$

which is used to directly obtain the field components $\mathbf{V}(z)$ at any location inside the biansiotropic media using the components at the origin $\mathbf{V}\big|_{z=0}$.

The eigendecomposition of the transfer matrix $\mathbf{T}(z) = e^{\iota \mathbf{A} z}$ yields

$$\mathbf{T} = \mathbf{U}\mathbf{P}\mathbf{U}^{-1}, \tag{2.5}$$

where $\mathbf{P} = \exp \iota[\mathbf{K}z]$, $\mathbf{K} = \mathrm{diag}(k_\mathrm{a}, k_\mathrm{b}, k_\mathrm{c}, k_\mathrm{d})$, and $\mathbf{U} = (\mathbf{V}_\mathrm{a} \mid \mathbf{V}_\mathrm{b} \mid \mathbf{V}_\mathrm{c} \mid \mathbf{V}_\mathrm{d})$ is the matrix of four eigenvectors $\mathbf{V}_i$, corresponding to a matching eigenvalue k_i, $i = \{\mathrm{a,b,c,d}\}$ of matrix $\mathbf{A}$.

The eigenvectors $\mathbf{V}_\mathrm{a}$, $\mathbf{V}_\mathrm{b}, \mathbf{V}_\mathrm{c}, \mathbf{V}_\mathrm{d}$ represent four possible *wavefronts* propagating through the bi-anisotropic medium, and the eigenvalues are the wavenumbers corresponding to each eigenmode. Typically, two of the eigenvalues are positive and two are negative corresponding to forward and backward propagation, respectively. Thus, in

$\mathbf{V}(z) = \mathbf{UPU}^{-1}\,\mathbf{V}\big|_{z=0}$ which combines (2.4) and (2.5), the term $\mathbf{U}^{-1}$ decomposes $\mathbf{V}\big|_{z=0}$ as a superposition of the four eigenvectors. Then the matrix $\mathbf{P}$ applies a propagation term to each eigenvector. Finally, the matrix $\mathbf{U}$ sums all four propagated eigenvector components of $\mathbf{V}(z)$.

The reflection and transmission coefficients are obtained as we apply an x-polarized and a y-polarized wave. First, we apply an x-polarized input wave at the front-side (superstrate- side) with the normalized values $E_{\mathrm{x,inc}} = 1$ and $H_{\mathrm{y,inc}} = 1/z_1$, where z_1 and z_2 are respectively the intrinsic impedances of the superstrate and substrate. Then, we have the input-side vector due to the addition of incident and reflected wave in the following form $\mathbf{E}_1 = \mathbf{I}_{\mathrm{x}} + \mathbf{S}_{11}^{\mathrm{x}}$, $\mathbf{H}_1 = z_1^{-1}\mathbf{n}\left(\mathbf{I}_{\mathrm{x}} - \mathbf{S}_{11}^{\mathrm{x}}\right)$, and the output vectors being $\mathbf{E}_2 = \mathbf{S}_{21}^{\mathrm{x}}$, $\mathbf{H}_2 = z_2^{-1}\mathbf{n}\mathbf{S}_{21}^{\mathrm{x}}$, where $\mathbf{I}_{\mathrm{x}} = \begin{pmatrix}1 & 0\end{pmatrix}^{\mathrm{T}}$, and $\mathbf{S}_{11}^{\mathrm{x}} = \begin{pmatrix}S_{11}^{\mathrm{xx}} & S_{11}^{\mathrm{yx}}\end{pmatrix}^{\mathrm{T}}$ and $\mathbf{S}_{21}^{\mathrm{x}} = \begin{pmatrix}S_{21}^{\mathrm{xx}} & S_{21}^{\mathrm{yx}}\end{pmatrix}^{\mathrm{T}}$ are the complex reflection and transmission coefficients.

Therefore, after partitioning the transfer matrix $\mathbf{T}(l) = \exp \iota\mathbf{A}l = \begin{pmatrix}\mathbf{T}_{11} & \mathbf{T}_{12} \\ \mathbf{T}_{21} & \mathbf{T}_{22}\end{pmatrix}$ (l is the thickness of the BA layer) and writing

$$\mathbf{E}_2 = \mathbf{T}_{11}\mathbf{E}_1 + \mathbf{T}_{12}\mathbf{H}_1 \quad \text{and} \quad \mathbf{H}_2 = \mathbf{T}_{21}\mathbf{E}_1 + \mathbf{T}_{22}\mathbf{H}_1, \tag{2.6}$$

we arrive at

$$\mathbf{S}_{21}^{\mathrm{x}} = \mathbf{M}_1^{+}\mathbf{I}_{\mathrm{x}} + \mathbf{M}_1^{-}\mathbf{S}_{11}^{\mathrm{x}},\ z_2^{-1}\mathbf{n}\mathbf{S}_{21}^{\mathrm{x}} = \mathbf{M}_2^{+}\mathbf{I}_{\mathrm{x}} + \mathbf{M}_2^{-}\mathbf{S}_{11}^{\mathrm{x}}, \tag{2.7}$$

so that the complex reflection $\mathbf{S}_{11}^{\mathrm{x}} = \begin{pmatrix}S_{11}^{\mathrm{xx}} & S_{11}^{\mathrm{yx}}\end{pmatrix}^{\mathrm{T}}$ and transmission $\mathbf{S}_{21}^{\mathrm{x}} = \begin{pmatrix}S_{21}^{\mathrm{xx}} & S_{21}^{\mathrm{yx}}\end{pmatrix}^{\mathrm{T}}$ coefficients for an x-polarized superstrate-side illumination, are finally defined through the linear combinations of the partitions of $\mathbf{T}$ ($\mathbf{M}_1^{\pm} = \mathbf{T}_{11} \pm z_1^{-1}\mathbf{T}_{12}\mathbf{n}$, and $\mathbf{M}_2^{\pm} = \mathbf{T}_{21} \pm z_1^{-1}\mathbf{T}_{22}\mathbf{n}$) as

$$\mathbf{S}_{11}^{\mathrm{x}} = \left[\mathbf{M}_2^- - z_2^{-1}\mathbf{n}\mathbf{M}_1^-\right]^{-1}\left[z_2^{-1}\mathbf{n}\mathbf{M}_1^+ - \mathbf{M}_2^+\right]\mathbf{I}_{\mathrm{x}} \tag{2.8}$$

$$\mathbf{S}_{21}^{\mathrm{x}} = \left[\left(\mathbf{M}_1^-\right)^{-1} - z_2^{-1}\left(\mathbf{M}_2^-\right)^{-1}\mathbf{n}\right]^{-1}\left[\left(\mathbf{M}_1^-\right)^{-1}\mathbf{M}_1^+ - \left(\mathbf{M}_2^-\right)^{-1}\mathbf{M}_2^+\right]\mathbf{I}_{\mathrm{x}} \tag{2.9}$$

In a similar way, for y-polarized input $\mathbf{I}_{\mathrm{y}} = \begin{pmatrix}0 & 1\end{pmatrix}^{\mathrm{T}}$, we can obtain the complex reflection $\mathbf{S}_{11}^{\mathrm{y}} = \begin{pmatrix}S_{11}^{\mathrm{xy}} & S_{11}^{\mathrm{yy}}\end{pmatrix}^{\mathrm{T}}$ and transmission $\mathbf{S}_{21}^{\mathrm{y}} = \begin{pmatrix}S_{21}^{\mathrm{xy}} & S_{21}^{\mathrm{yy}}\end{pmatrix}^{\mathrm{T}}$ coefficients for y-polarized superstrate-side illumination:

$$\mathbf{S}_{11}^{\mathrm{y}} = \left[\mathbf{M}_2^- - z_2^{-1}\mathbf{n}\mathbf{M}_1^-\right]^{-1}\left[z_2^{-1}\mathbf{n}\mathbf{M}_1^+ - \mathbf{M}_2^+\right]\mathbf{I}_{\mathrm{y}}, \tag{2.10}$$

$$\mathbf{S}_{21}^{\mathrm{y}} = \left[\left(\mathbf{M}_1^-\right)^{-1} - z_2^{-1}\left(\mathbf{M}_2^-\right)^{-1}\mathbf{n}\right]^{-1}\left[\left(\mathbf{M}_1^-\right)^{-1}\mathbf{M}_1^+ - \left(\mathbf{M}_2^-\right)^{-1}\mathbf{M}_2^+\right]\mathbf{I}_{\mathrm{y}} \tag{2.11}$$

For back illumination (substrate illumination), using same route, we get $\mathbf{E}_2 = \mathbf{I}_{\mathrm{x}} + \mathbf{S}_{22}^{\mathrm{x}}$, $\mathbf{H}_2 = z_2^{-1}\mathbf{n}\left(\mathbf{S}_{22}^{\mathrm{x}} - \mathbf{I}_{\mathrm{x}}\right)$, with the output vectors being $\mathbf{E}_1 = \mathbf{S}_{12}^{\mathrm{x}}$, $\mathbf{H}_1 = -z_1^{-1}\mathbf{n}\mathbf{S}_{12}^{\mathrm{x}}$. Using (6), we get:

$$\mathbf{I}_{\mathrm{x}} + \mathbf{S}_{22}^{\mathrm{x}} = \mathbf{M}_1^-\mathbf{S}_{12}^{\mathrm{x}},\ \ z_2^{-1}\mathbf{n}\left(\mathbf{S}_{22}^{\mathrm{x}} - \mathbf{I}_{\mathrm{x}}\right) = \mathbf{M}_2^-\mathbf{S}_{12}^{\mathrm{x}}, \tag{2.12}$$

$$\mathbf{S}_{22}^{\mathrm{x}} = \left[z_2^{-1}\left(\mathbf{M}_2^-\right)^{-1}\mathbf{n} - \left(\mathbf{M}_1^-\right)^{-1}\right]^{-1}\left[\left(\mathbf{M}_1^-\right)^{-1} + z_2^{-1}\left(\mathbf{M}_2^-\right)^{-1}\mathbf{n}\right]\mathbf{I}_{\mathrm{x}} \tag{2.13}$$

$$\mathbf{S}_{12}^{\mathrm{x}} = 2\left[\mathbf{M}_1^- + z_2\mathbf{n}\mathbf{M}_2^-\right]^{-1}\mathbf{I}_{\mathrm{x}} \tag{2.14}$$

Similarly for y-polarized input, we get:

$$\mathbf{S}_{22}^{\mathrm{y}} = \left[z_2^{-1}\left(\mathbf{M}_2^-\right)^{-1}\mathbf{n} - \left(\mathbf{M}_1^-\right)^{-1}\right]^{-1}\left[\left(\mathbf{M}_1^-\right)^{-1} + z_2^{-1}\left(\mathbf{M}_2^-\right)^{-1}\mathbf{n}\right]\mathbf{I}_{\mathrm{y}} \tag{2.15}$$

$$\mathbf{S}_{12}^{\mathrm{y}} = 2\left[\mathbf{M}_1^- + z_2\mathbf{n}\mathbf{M}_2^-\right]^{-1}\mathbf{I}_{\mathrm{y}} \tag{2.16}$$

And hence, all the complex reflection and transmission coefficients described in Table 1 are obtained. One major advantage of this direct solver is that it depends on simple matrix operations, which are reversible. This makes the development of the inverse solver straightforward as described in the following section.

The inverse problem uses the complex reflection and transmission coefficients to obtain the corresponding material dyadics described in Eq. (2.1). This is accomplished in two steps. First the linear operator $\mathbf{T}$ is retrieved; then it is used to obtain all the material constants. For x- and y-polarized inputs used at the front '+' and back '–' side illumination, there are four sets of fields $\mathbf{V}_j = \begin{pmatrix}\mathbf{V}_j^+ & \mathbf{V}_j^-\end{pmatrix}$, $j = \{1,2\}$ that can be used to form the equation:

$$\mathbf{V}_2 = \mathbf{T}\mathbf{V}_1 \tag{2.17}$$

where all four illumination states are grouped together as:

$$\begin{aligned}\mathbf{V}_2 &= \begin{pmatrix}\mathbf{S}_{21}^{\mathrm{x}} & \mathbf{S}_{21}^{\mathrm{y}} & \mathbf{I}_{\mathrm{x}} + \mathbf{S}_{22}^{\mathrm{x}} & \mathbf{I}_{\mathrm{y}} + \mathbf{S}_{22}^{\mathrm{y}} \\ z_2^{-1}\mathbf{n}\mathbf{S}_{21}^{\mathrm{x}} & z_2^{-1}\mathbf{n}\mathbf{S}_{21}^{\mathrm{y}} & z_2^{-1}\left(\mathbf{S}_{22}^{\mathrm{x}} - \mathbf{I}_{\mathrm{x}}\right) & z_2^{-1}\left(\mathbf{S}_{22}^{\mathrm{y}} - \mathbf{I}_{\mathrm{y}}\right)\end{pmatrix}, \\ \mathbf{V}_1 &= \begin{pmatrix}\mathbf{I}_{\mathrm{x}} + \mathbf{S}_{11}^{\mathrm{x}} & \mathbf{I}_{\mathrm{y}} + \mathbf{S}_{11}^{\mathrm{y}} & \mathbf{S}_{12}^{\mathrm{x}} & \mathbf{S}_{12}^{\mathrm{y}} \\ z_1^{-1}\mathbf{n}\left(\mathbf{I}_{\mathrm{x}} - \mathbf{S}_{11}^{\mathrm{x}}\right) & z_1^{-1}\mathbf{n}\left(\mathbf{I}_{\mathrm{y}} - \mathbf{S}_{11}^{\mathrm{y}}\right) & -z_1^{-1}\mathbf{n}\mathbf{S}_{12}^{\mathrm{x}} & -z_1^{-1}\mathbf{n}\mathbf{S}_{12}^{\mathrm{y}}\end{pmatrix}.\end{aligned} \tag{2.18}$$

From Eq. (2.17) and the connection between $\mathbf{T}$ and $\mathbf{A}$ given by $\mathbf{T} = \exp \iota\mathbf{A}l$, an immediate result is that

$$\mathbf{A} = \tfrac{1}{\iota l}\ln\left(\mathbf{V}_2\mathbf{V}_1^{-1}\right). \tag{2.19}$$

Moreover, as we recall from Eq (2.3) that $\mathbf{A} = \omega\mathbf{N}\begin{pmatrix}\varepsilon_0\boldsymbol{\varepsilon} & c^{-1}\boldsymbol{\xi} \\ c^{-1}\boldsymbol{\zeta} & \mu_0\boldsymbol{\mu}\end{pmatrix}$

$$\begin{pmatrix} \varepsilon_0\boldsymbol{\varepsilon} & c^{-1}\boldsymbol{\xi} \\ c^{-1}\boldsymbol{\zeta} & \mu_0\boldsymbol{\mu} \end{pmatrix} = \frac{1}{\iota\omega l}\mathbf{N}^{-1}\ln\left(\mathbf{V}_2\mathbf{V}_1^{-1}\right). \tag{2.20}$$

This concludes the retrieval of the BA parameters from a given set of complex reflection and transmission coefficients obtained upon four distinct illumination states.

It is important to note that the eigendecomposition of $\mathbf{A} = \frac{1}{\iota l}\ln(\mathbf{T})$, which is $\mathbf{A} = \frac{1}{\iota l}\mathbf{U}\left(\ln(\mathbf{P})\right)\mathbf{U}^{-1}$ where $\mathbf{P}$ is the diagonal matrix carrying the eigenvalues of $\mathbf{T}$, could suffer from phase ambiguity if one of the phase terms which are real parts of $k_{\mathrm{a}}l$, $k_{\mathrm{b}}l$, $k_{\mathrm{c}}l$ or $k_{\mathrm{d}}l$ is above π or below $-\pi$, This should not be the case for a metasurface of sub-wavelength thickness. Some techniques have been developed to overcome phase ambiguity for the retrieval of bulk media such as the one in [132] which performs the retrieval over a spectral range where there is no ambiguity at the largest wavelength. The technique then utilizes phase unwrapping along the remaining spectral range to remove the ambuguity. This can be implemented to our technique by applying phase unwrapping to the elements of the diagonal matrix $\mathbf{P}$, but we don't need it in our work with metasurfaces.

2.3 Homogenization of nano-structures

In this section, the algorithm is implemented to homogenize two different metasurfaces. One metasurface is an array of V-shaped, gold antennae with a thickness of 30 nm fabricated on top of a silicon substrate. Figure 2.2(a) a unit-cell of structure with dimensions of 200 nm x 200 nm, and a V-shape angle of 60^0 between the two arms. Each arm has a length of 160 nm, and a width of 40 nm. The second structure, shown schematically in Fig. 2.2(b), has a unit-cell size of 300 nm x 300 nm and is composed of 2 gold rods, each of a 250-nm length, a 40-nm width, a 30-nm thickness, a vertical separation of 80 nm, and an orientation angle of 45^0. These rods are embedded in a 200-nm-thick polymer layer. Both structures will have a broken rotational symmetry (anisotropy).

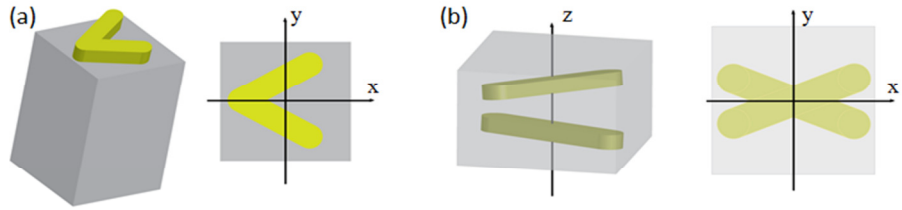

Fig. 2.2. The unit cell of the two nanostructures used as examples for the homogenization algorithm. A top view is presented for each to describe the x and y directions.

The diagonal terms of ξ and ζ cause coupling between x- and y-polarized waves as demonstrated in the studies done to the bi-isotropic case [133], while their off-diagonal terms affect the relation between the electric and magnetic fields while keeping x- or y-polarization, but causing the waves to experience different wave impedances for propagation in +z or –z direction. The structure of Fig 2.2(a) also has a broken directional symmetry due to the difference between superstrate and substrate plasmonic resonances, but the structure keeps its mirror symmetry with respect to x-axis causing negligible coupling between x- and y-polarized waves. Therefore, the model of this structure should contain only the off-diagonal terms of ξ and ζ and the diagonal terms should be negligible. However, the structure in Fig 2.2(b) lacks mirror symmetry with respect to x- or y-axis but has directional symmetry with respect to z-direction. Therefore its model should contain only the diagonal terms of ξ and ζ. The inverse solvers were applied to transmission and reflection coefficients of both structures (obtained using FEM) and the results were as expected. Figure 2.3 shows the results of implementing the homogenization algorithm with the V-antenna structure.

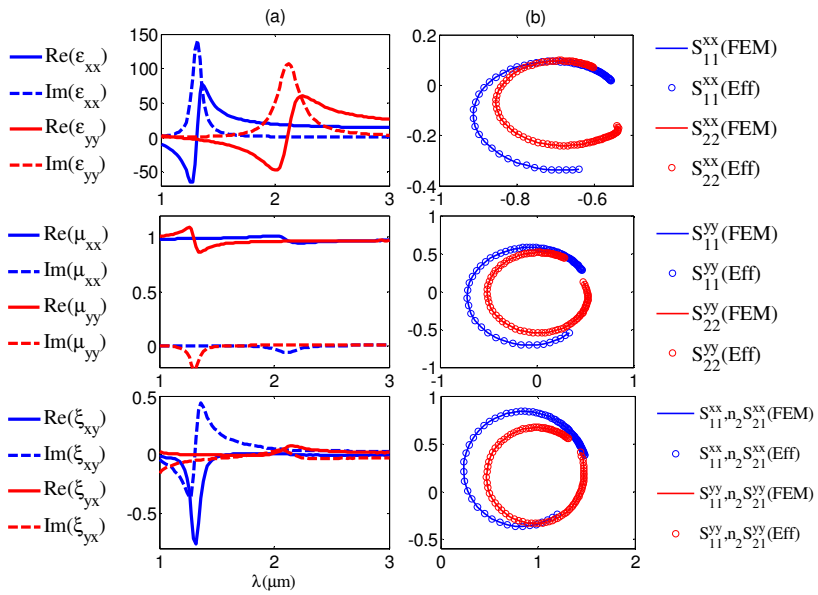

Fig. 2.3. (a) Effective slab parameters of the V-antenna structure. (b) Spectral phasor of *reflection and transmission coefficients* using FEM and effective Bi-anisotropic layer model. For all of them, the lower end point corresponds to 1 μm and the upper end point corresponds to 3 μm.

The V-antenna structure is modeled as a 30-nm-thick, homogeneous slab. First, the FEM solver is used to obtain the complex reflection and transmission coefficients for a spectral domain of 1μm – 3μm. Then the inverse solver is applied to obtain the effective parameters of the slab. The retrieved results of the effective slab parameters are shown in Fig 2.3(a). This design has been used to achieve large phase shifts [20, 23] from operation near the plasmonic resonance wavelength, and indeed the effect of the resonance is clear in the retrieved effective parameters. Both the FEM simulation and the effective bi-anisotropic model reproduce the same reflection and transmission coefficients as shown in Fig 2.3(b).

In this structure, we obtain only co-polarized reflection and transmission coefficients, with negligible values for cross-polarization coefficients. The directional asymmetry is noticed in the difference between reflection coefficients for the two sides of illumination. Still the transmission coefficients are symmetric (i.e. $S_{12}^{\mathrm{xx}} = n_2 S_{21}^{\mathrm{xx}}$ and $S_{12}^{\mathrm{yy}} = n_2 S_{21}^{\mathrm{yy}}$, where n_2 is the refractive index of the backward substrate [129]) , and this

would result in having $\zeta_{xy} = -\xi_{yx}$ and $\zeta_{yx} = -\xi_{xy}$ as mathematically proved in [129], so we needed only to show ξ_{xy} and ξ_{yx} in Fig 2.3(a).

Now the algorithm is applied to the two rod structure which is modeled as a homogeneous bi-anisotropic slab with a thickness of 200 nm. The FEM solver is used to obtain the complex reflection and transmission coefficients for the spectral domain of 2μm – 3μm. The retrieval algorithm is then applied to these data, and as in the previous case, the complex reflection and transmission coefficients obtained from the effective model match with these obtained from FEM simulation. The retrieval results are shown below in Fig 2.4. This structure has a mirror asymmetry or parity asymmetry and this results in the existence of the diagonal elements of the tensors ξ and ζ.This structure is exactly the same from both sides, and this directional symmetry causes the off-diagonal terms of ξ and ζ to be zero.

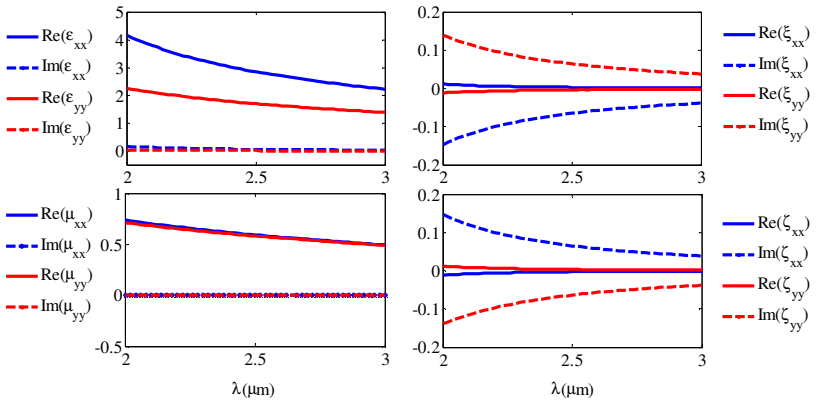

Fig. 2.4: Retrieval results of the two rod structure.

2.4 Application in Numerical solvers

Another important application of the homogenized model of the metasurface units is to develop fast full-wave solvers. By replacing the detailed nano-structures with homogenized tiles, the required meshing and time of simulation are dramatically reduced. The model is applied to replace a periodic array of eight antennae which are shown in figure 2.5, with their equivalent bianisotropic tiles. Then FDFD solver that incorporate bi-anisotropic terms is developed to simulate the simpler bianisotropic structure, and results are compared to FEM simulations of the exact nano-structures.

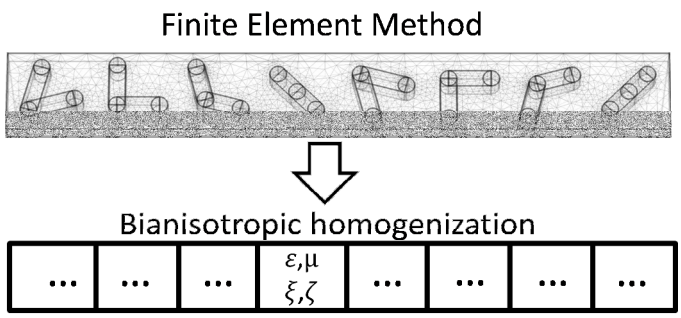

Fig. 2.5. Bianisotropic homogenization replaces the fine meshing on the antenna structures with effective bianisotropic tensors.

Equipped with FDFD, we are able to combine the compact descriptions of each constitutive antenna to describe a fully functional metasurface. Since the structures of V-shape antennae only vary in one direction, the bianisotropic homogenization simplifies the full-wave FDFD simulation to a two-dimension problem (Figure 2.8).

The formulation of the FDFD based on Maxwell's equations for two-dimensional structures is presented as follows:

$$\frac{i}{k_0}\frac{\partial}{\partial z}\begin{pmatrix} E_x \\ H_y \\ E_y \\ H_x \end{pmatrix} = \begin{pmatrix} \varsigma_{yx} & z_0(\mu_{yy} + \frac{1}{k_0^2}\frac{\partial}{\partial x}\left(\frac{1}{\varepsilon_z}\frac{\partial}{\partial x}\right)) & \varsigma_{yy} & z_0\,\mu_{yx} \\ \frac{1}{z_0}\varepsilon_{xx} & \xi_{xy} & \frac{1}{z_0}\varepsilon_{xy} & \xi_{xx} \\ -\varsigma_{xx} & -z_0\mu_{yx} & -\varsigma_{xy} & -z_0\,\mu_{xx} \\ -\frac{1}{z_0}\varepsilon_{yx} & -\xi_{yy} & -\frac{1}{z_0}(\varepsilon_{yy} + \frac{1}{k_0^2}\frac{\partial}{\partial x}\left(\frac{1}{\mu_z}\frac{\partial}{\partial x}\right)) & -\xi_{yx} \end{pmatrix}\begin{pmatrix} E_x \\ H_y \\ E_y \\ H_x \end{pmatrix} \tag{2.21}$$

Here k_0 and z_0 are the wave number and impedance of free space, correspondingly. The notation of FDFD is completed in the framework of matrix operators on a Yee grid [134]. Column vectors represent the electric and magnetic fields parallel to the metasurface. Square matrices represent linear mathematical operations performed on the column vectors. Four algebraic equations are written for every cell.

First, we test the FDFD solver on a single V-shape antenna (60° splitting angle) and verify it through a comparison with the full structure simulation using FEM (COMSOL Multiphysics). For both the FDFD and FEM methods, periodic boundary conditions are applied on two sides of the V-shape antenna. The plane wave is excited at one port and exits the computation domain at the other port. From Figure 2.7, we can see that our approach converges well in both principal polarization (x) and secondary polarization (y) spectra, and the differences between FEM results and FDFD results are negligible. After validating the FDFD solver, we simulate the metasurface composed of arrays of eight effective bianisotropic tiles, where the total-field/scattered-field formulation is implemented. The scattered-field region is bounded by perfectly match layers. Periodic boundary conditions are applied to repeat the array of eight antennae. Figure 2.7 clearly shows that the anomalous field (under the y polarization) is propagating in a single direction which is determined by the generalized Snell's law[23]. We also extract the zero-order diffraction mode of the normal fields and the first-order diffraction of the anomalous fields to obtain the power transmission percentage as shown in Figure 2.7. FDFD and FEM results are well matched in the regular antenna arrays, while some discrepancies show up in the complementary arrays. This discrepancy can be attributed to the stronger near-field interactions between neighboring antennae, which are ignored in the process of bianisotropic retrieval.

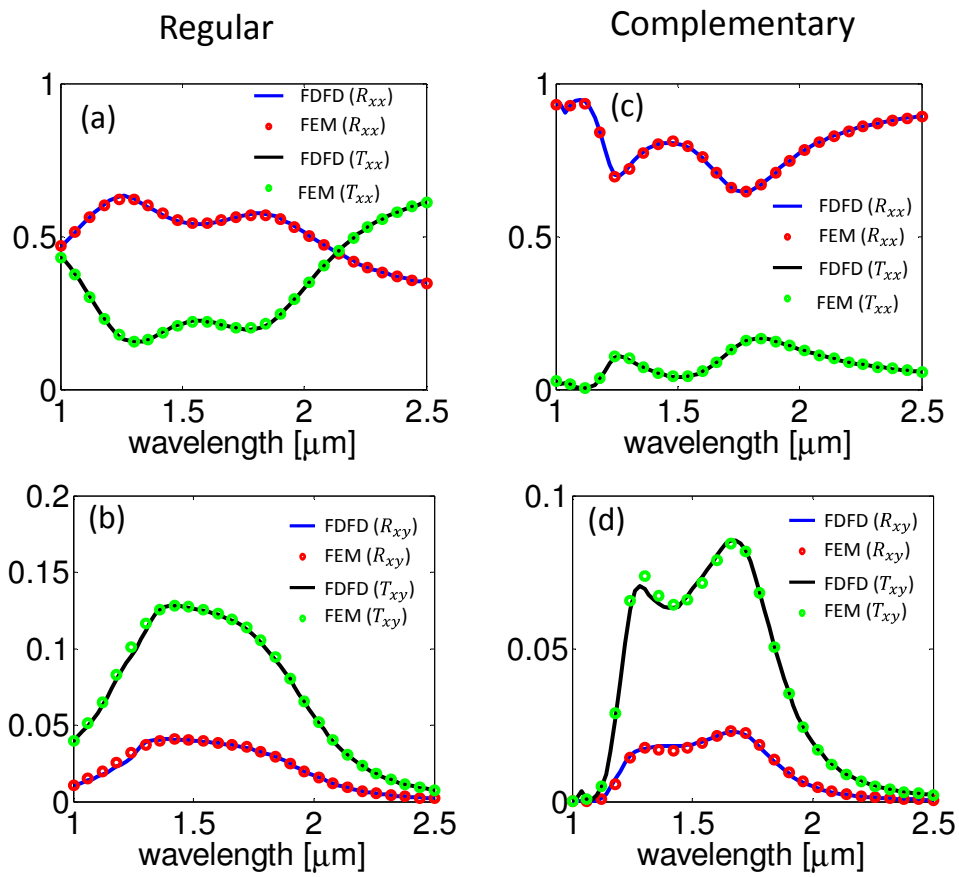

Fig. 2.6. Implement the FDFD simulation on a single V-shape antenna (60° splitting angle) and verify it by comparison with the full structure simulation using FEM.

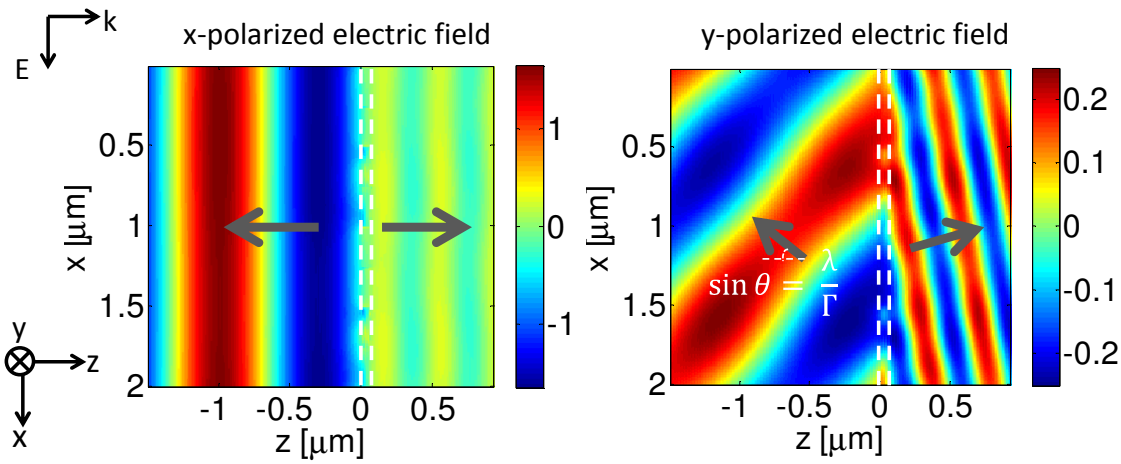

Fig. 2.7. (a,b) FDFD simulation of arrays of eight regular antennae represented by bianisotropic properties. Light is incident from the left with the electric field polarized in the x direction. White dashed lines indicate the position of the antenna array. The size of each antenna is 250 nm. The pitch of the antenna array (Γ) is 2 μm. The thickness is 60nm. The wavelength ($\boldsymbol{\lambda}$) is 1.36 μm.

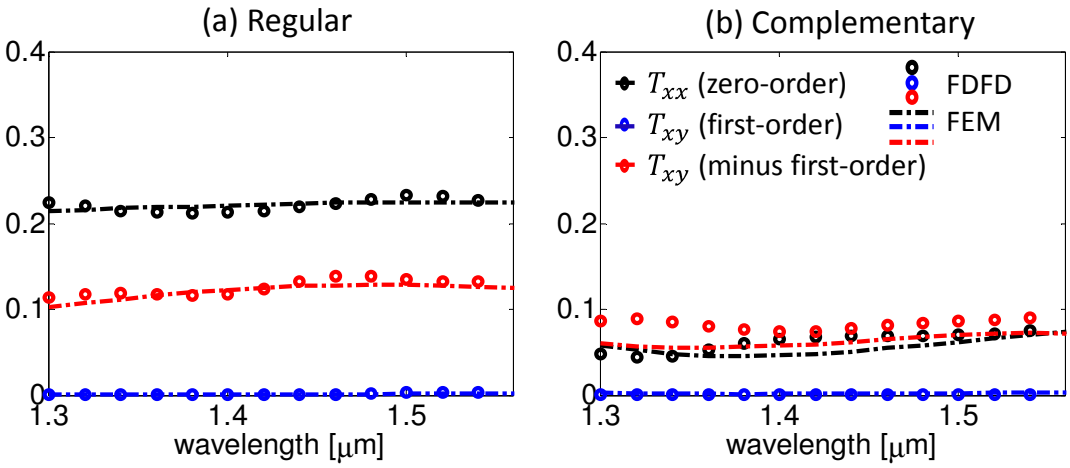

Fig. 2.8. The normal and anomalous power transmission percentage are computed using both FDFD and COMSOL. Zero-order mode and first-order diffracted mode are extracted using Fourier transform of the transmitted fields.

The proof-of-concept FDFD formulation is implemented in MATLAB in our tests. The compiling and testing environment is dual 12-core AMD Opteron 6172 processors with 100 GB memory and 10 Gigabit Ethernet. For the 10 nm uniform grid size (as used

in Figure 4.7 and Figure 4.8), the memory consumption is 2.4 GB. The grid size is currently limited by the thickness of the antenna. The non-uniform rectangular grids could be applied to further reduce the memory and computation time. For the FEM solver (COMSOL Multiphysics), 3D simulation is implemented in a direct solver, under the same dimension of computation domain with 80 nm maximum meshing size and 10 nm minimum meshing size. The memory consumption is 60 GB. Thus, modeling the metasurface by effective bianisotropic tiles no longer requires the fine meshing on the detailed structures of antennae and greatly reduces the computation load.

2.5 Conclusion

A new approach has been presented for the homogenization of optical metamaterials. An algorithm was developed which included a direct and an inverse solver based on an eigenwave analysis and a transfer matrix approach. This method of modeling and characterizing a metamaterial is useful for the design and use of metasurfaces. In addition, it provides insight into how these metamaterial layers affect an incident light beam. The used model is the most general bi-anisotropic model for normal incident illumination. This model can be extended to include effects on oblique incident waves.

3. PHOTONIC SPIN HALL EFFECT AND METASURFACE BASED CHIROPTICAL SPECTROMETERS

3.1 Introduction

Chiral structures possessing differential optical response to light circular polarization are very recurrent in biological and organic compounds. Attaining chiroptical effects is of immense bio-chemical importance, yet requires complicated structures. Circular dishroism (CD) spectrometers measuring the differential absorption between left- (LCP) and right-circular polarizations (RCP) involve complex hardware to switch laser polarization and manage data acquisition sequentially. Here, we present compact and power-efficient metasurface-based chiroptical spectroscopy solutions based on gap-plasmon metasurfaces (GPMS). First, a minimalistic design of a real-time CD spectrometer is obtained by using the photonic spin Hall effect (PSHE) in a single GPMS which spatially separates LCP and RCP spectra. It is the smallest CD spectrometer to our knowledge. Another GPMS-based device built with the same approach rotates light polarization by 45^0 through adding a phase-shift between LCP and RCP. Thus, PSHE in GPMS can provide efficient solutions to vital applications including bio-sensing, DNA structural analysis, and stereochemistry.

Circular Dichroism (CD) spectrometer is an important tool in sensing chiral molecules possessing differential optical response to light circular polarization. These molecules are very recurrent in biological and organic compounds, and hence, CD spectrometer is used in biological material studies[135], protein and DNA structural analysis[136], and stereochemical detection[137]. Typical CD spectrometers perform sequential measurements of left- (LCP) and right-circular polarizations (RCP) [138, 139]. They are large in size and involve complex hardware to switch laser polarization and manage sequential data acquisition. Here, we seek an alternative chiroptical spectroscopy

technique that performs spatial separation of LCP and RCP. This can dramatically reduce the size of CD spectrometers and provide real-time sensing.

Chiroptical spectroscopy built on the differential response between LCP and RCP requires chiral structures to obtain the L/RCP beams. With the advent of nanotechnology, multi-layer metamaterial structures with strong chirality have been demonstrated[140-143]. Generally, the design and fabrication of such bulk chiral structures is complicated because they require layer-by-layer fabrication with each layer oriented and aligned with respect to the previous layer. The complexity can be drastically reduced by using metasurfaces[19].

In this work, we introduce a metasurface that exhibits the photonic spin Hall effect (PSHE)[51, 52, 144, 145]. It reflects different spins (circular polarizations) in opposite directions exhibiting mirror-symmetric reflection angle dispersion depicted in figure 3.1, and hence, generates separate spectra for LCP and RCP. Thus, by using a single, deeply subwavelength scale and lightweight metasurface, we eliminate the need of using a tunable light source that switches from LCP to RCP, a bulky natural chiral medium, and other more complicated detection schemes. This unique functionality can be obtained by using a broadband source, such as a xenon lamp or LED, which includes equal components of LCP and RCP, which are then spatially separated by the metasurface for straightforward detection. Not only does this metasurface enable a very compact device (130-nm thickness), but it also allows for a real time sensing due to simultaneous collection of the LCP & RCP data at all the wavelengths. First, we explain the methodology of the metasurface design, followed by experimental results of the device implementation. Then, we describe a projection of the proposed design principles onto another metasurface device that performs optical rotation of incident light.

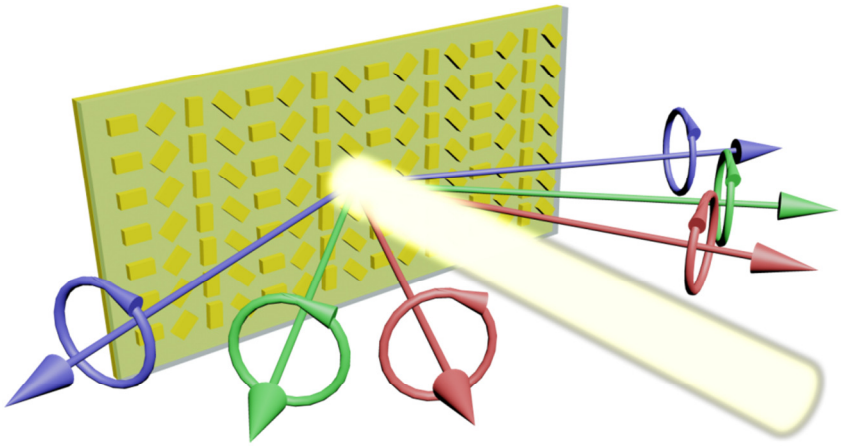

Fig. 3.1. Illustration of the metasurface used as a CD spectrometer using the photonic spin Hall effect. The spin components of the incident broadband source are reflected in opposite directions, and each wavelength component is reflected at a different angle. As a result, LCP and RCP spectra are obtained simultaneously. Colors are used for illustration and do not represent the wavelength values used in this work.

3.2 Methodology

To obtain a spin-dependent response, an array of anisotropic elements is used to achieve different phase gradients in response to LCP and RCP light, so that these circularly polarized components are reflected in different directions. This technique was introduced using polarization gratings [21, 22] with thick layers to achieve a π phase delay between the major and minor axes. Later, it was proposed to use anisotropic subwavelength aperture antennas [146], which are much thinner but have a poor power efficiency (only a few percent). Using gap-plasmon [30, 60, 61, 147-149] (GP) NA instead, it is possible to obtain the same function with a compact subwavelength structure and dramatically improved power efficiency. With this design we're overcoming the poor power efficiency of single layered plasmonic metasurfaces such as those made with v-antennas[20]. There have been also earlier demonstrations of effective GP structures in the microwave regime [58, 150]. The unit cell of a gap-plasmon structure is shown in figure 3.2(a). It has a bottom gold layer that works as a reflecting mirror, a top 30-nm

thick gold NA, and a 50-nm thick dielectric (alumina, Al_2O_3) spacer. The metal/dielectric/metal sandwich enables the excitation of a compact GP wave[60]. The incident plane wave couples to this slow GP wave which accumulates a large optical phase over the very short length of the NA. By tuning the aspect ratio (L_x/L_y) of the antennas geometry, we can indeed achieve a phase delay of π between the reflection coefficients of the GP NA along its major and minor axes.

To present the operation of the entire device, we begin with analysis of a single NA. Let the complex coefficient of reflection for a single NA as shown in figure 3.2(b) in the x- and y-axis be r_x and r_y, respectively. Then, for the NA tilted at an angle α in figure 3.2(c), it is straightforward to obtain its reflection matrix in circular basis using the Jones calculus[151] as:

$$R(\alpha)_{circular} = \begin{bmatrix} \frac{1}{2}(r_x - r_y)e^{-i2\alpha} & \frac{1}{2}(r_x + r_y) \\ \frac{1}{2}(r_x + r_y) & \frac{1}{2}(r_x - r_y)e^{i2\alpha} \end{bmatrix} \tag{3.1}$$

So, for an RCP incident wave, the reflected wave E_{ref} takes the form:

$$E_{ref} = \frac{1}{2}(r_x - r_y)e^{-i2\alpha}\begin{pmatrix} 1 \\ 0 \end{pmatrix} + \frac{1}{2}(r_x + r_y)\begin{pmatrix} 0 \\ 1 \end{pmatrix} \tag{3.2}$$

And for LCP incidence, we obtain:

$$E_{ref} = \frac{1}{2}(r_x - r_y)e^{i2\alpha}\begin{pmatrix} 0 \\ 1 \end{pmatrix} + \frac{1}{2}(r_x + r_y)\begin{pmatrix} 1 \\ 0 \end{pmatrix} \tag{3.3}$$

Therefore, we have two reflection terms, a co-polarized term with an abrupt phase term of $e^{-i2\alpha}(e^{i2\alpha})$ for RCP (LCP) incidence, and a cross-polarized term with no phase gradient. We are interested in the first term only where the phase shift can be controlled by tuning α. Therefore, we tailor our NA dimensions to minimize $r_x + r_y$ and maximize $r_x - r_y$, which imposes the out-of-phase requirement for r_x and r_y. The dimensions of the

NA in fig 3.2(b) are chosen to optimize the performance of the structure in the near infra-red (NIR) region. Figure 3.2(d) shows the simulation results of the co-polarized reflected power component $\left|r_x - r_y\right|^2 \big/ 4$ and the cross-polarized component $\left|r_x + r_y\right|^2 \big/ 4$ using a finite element solver with the Johnson-Christy material values for gold [152]. Simulation reveals that we have a broadband NIR range where the majority of the reflected power (up to ~50%) is in the co-polarized term which can be controlled by α according to equations (3.2) and (3.3). In our structure, we use a periodic array of four antennas rotated at angles $\alpha = 0^0, 45^0, 90^0, 135^0$, as shown in figure 3.2(e) which is the field emission scanning electron microscope (FE SEM) image of the metasurface. The four NAs form a linear phase distribution from 0 to $2\pi\,(-2\pi)$ for reflected LCP (RCP) beam across a period of $P = 1.8\mu\mathrm{m}$. Therefore, by applying the generalized law of reflection [19], we obtain the angle of reflection from the metasurface as:

$$\sin\theta_r = \begin{cases} -\lambda \big/ P, \text{ for RCP} \\ \lambda \big/ P, \text{ for LCP} \end{cases} \tag{3.4}$$

The metasurface is fabricated on top of a silicon substrate, where the bottom 50 nm gold and the 50 nm alumina layers are implemented using electron beam deposition, and the 30 nm thick gold antennas are patterned using a standard electron beam lithography and lift off process. The experimental setup used to test the metasurface is shown in figure 3.3(a). It consists of a tunable monochromatic source, a polarizer, and a retarder to obtain circularly polarized incident beams.

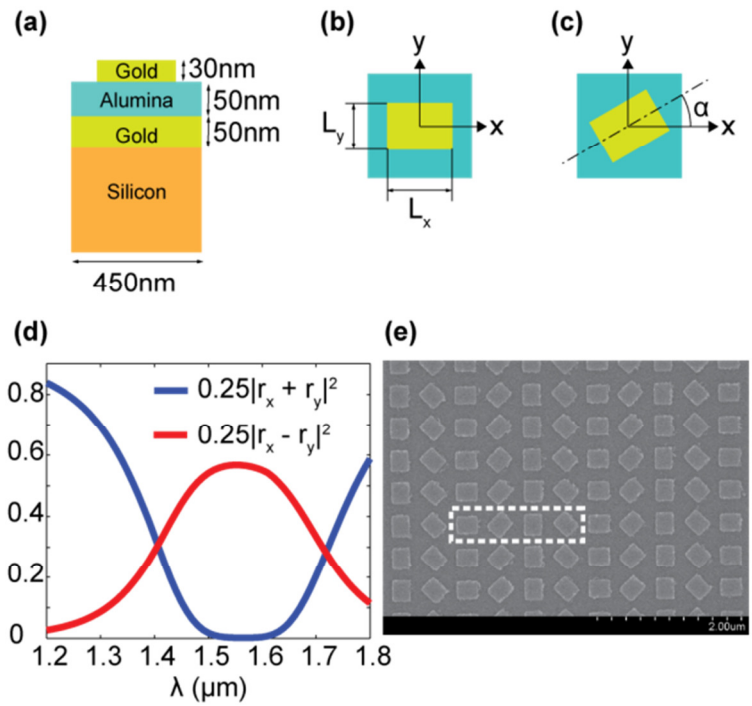

Fig 3.2**.** (a) Schematic of a unit cell of a gap-plasmon based antenna structure consisting of gold/alumina/gold structure. Silicon substrate carries the metasurface and plays no role in the operation. (b) Top view of the unit cell, with nano-antenna dimensions $L_x = 280\ \mathrm{nm}$ and $L_y = 230\ \mathrm{nm}$. (c) Top view of the unit cell, with the nano-antenna tilted at an angle α. (d) Simulation results of circular co-polarized reflection power (red) and cross-polarized reflected power (blue). (e) Field emission scanning electron microscope (FE SEM) image of the metasurface, with dashed rectangle to demonstrate one period of the structure.

Measurements are taken using a spectroscopic ellipsometer device which allows rotation of the detector to collect the reflected ray as a function of reflection angle θ_r. Figure 3.3(b) shows the measurement taken for both LCP and RCP for different values of wavelengths in the range $\lambda = 1.2 - 1.7\mu\mathrm{m}$ plotted as a function of reflected angle θ_r. The reflected power is 40% at $\lambda = 1.5\mu\mathrm{m}$, and decreases gradually on both sides as predicted by simulation in figure 3.2(d). Complete separation of LCP and RCP spectra is demonstrated. Lithographical patterning of gold nano-structures increases the Au effective losses due to electron scattering at finer polycrystalline grain boundaries and additional surface roughness features. Efficiency can be enhanced with encapsulated

thermal annealing, which could significantly reduce the electron damping factors, and at the same time preserve the shape of nanostructures [153].

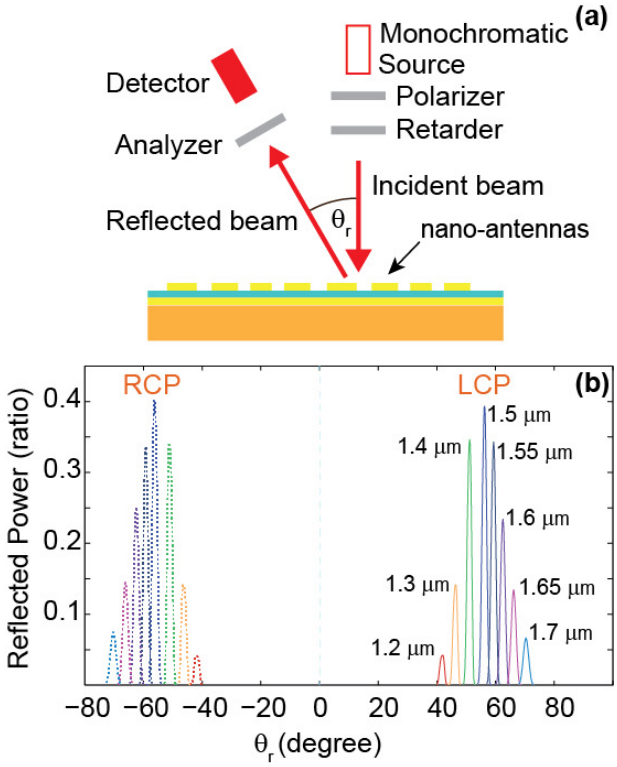

Fig. 3.3. (a) Schematics of the experimental setup for testing the metasurface. A tunable monochromatic source, a polarizer, and a retarder are used to obtain circularly polarized incident beams for different wavelengths. Measurements are taken using a rotating arm device which allows rotation of detector to collect the reflected ray as a function of reflection angle θ_r. (b) Experimental results of reflected power for LCP and RCP incident beams at different wavelengths as a function of reflected angle showing discrimination of LCP and RCP spectra.

3.3 Conclusion

In conclusion, a metasurface is designed and implemented to work as an extremely thin and small CD spectrometer in NIR. The photonic spin Hall effect is used for real time spatial separation of LCP and RCP spectra of an unpolarized source such as a lamp.

It eliminates the need for switching the light source polarization and any necessary hardware required for this operation. With a GP NA, the power efficiency of the metasurface is up to 40% - an order of magnitude larger than similar structures - because it can be optimized to focus the reflected energy in the required mode of operation.

4. OPTICALLY ACTIVE METASURFACES

4.1 Introduction

We design, fabricate, and experimentally demonstrate an optically active metasurface of λ/50 thickness which rotates linearly polarized light by 45^0 over a broadband wavelength range in the near IR region. The rotation is achieved through the use of a planar array of plasmonic nano-antennas which generates a fixed phase-shift between the left circular polarized and right circular polarized components of the incident light. Our approach is built on a new supercell metasurface design methodology: by judiciously designing the location and orientation of individual antennas in the structural supercells, we achieve *an effective chiral metasurface* through *a collective operation of non-chiral antennas*. This approach simplifies the overall structure when compared to designs with chiral antennas and also enables a chiral effect which *quantitatively* depends solely on the supercell geometry. This allows for greater tolerance against fabrication and/or temperature effects.

An optically active material produces a different response to right circularly polarized (RCP) and left circularly polarized (LCP) light[154], thereby rotating the angle of linearly polarized light along the propagating direction. The importance of optical activity transcends optical applications and is of immense value to sensing applications in stereochemistry[155], molecular biology[156], crystallography[157], and secure quantum communications[158]. It is typically obtained using chiral structures, which do not superimpose onto their mirror image, lifting the degeneracy of LCP and RCP. The effect is generally weak in natural materials and detectable only when strong phase differences between LCP and RCP accumulate over a long optical path. With the advent of nanotechnology, strong optical activity using artificially structured materials have been demonstrated. To achieve the rotation of the electromagnetic field vectors, structures are

designed to rotate with angular offset along the propagation direction and possess directional mirror asymmetry. Design and fabrication of such chiral structures[45, 133, 140-142, 159-161] is complicated because they require multiple fabrication steps to complete the angular rotations assigned for successive layers in a third dimension. Complexity can be reduced using optical metasurfaces, which have also been used to obtain optical activity (OA) using planar chiral structures[43, 44, 46-48], where optical activity was obtained either through intrinsic or extrinsic chirality of antennas. Intrinsic chiral antennas do not superimpose onto their mirror image, while extrinsic antennas only break mirror symmetry under oblique incidence and cannot obtain chiral properties if light is normally incident. For both cases, there has been no clear strategy to design a metasurface with a specific OA angle.

4.2 Methodology

In this work, a desired OA is obtained using an optical metasurface with a different approach other than the intrinsic or extrinsic chirality of nanoantennas. Here, we present an array of nanoantennas, which individually are non-chiral, but where chirality is obtained through the collective contribution of the entire array, or more specifically through the array of supercells. This avoids both the complex structure of intrinsic chiral antennas and the incident angle dependence of extrinsic chiral antennas. Additionally, a design methodology is introduced to realize a rotation of polarization angle (PA) to any specific value - 45^0 in our case – accurately determined by the geometry of structure rather than the intrinsic properties of composite materials. In previous 2D and 3D chiral structures, there was no quantitative formula between the introduced chiral effect and the geometry of the structure. The typical procedure was to design an asymmetric structure with a handedness that relates qualitatively to the required chiral effect, and then to optimize it quantitatively through simulation and experimentation. Having a quantitative formula relating the chiral effect to the structure's geometry facilitates the designer's work and secures stability against fabrication and/or temperature effects. Our goal is achieved through splitting the circular components of the incident beam and introducing

an optical phase delay between the opposite polarizations. The rotation of PA is related to the introduced phase difference as will be explained below, and based on this relation, it will be shown how our metasurface is designed to achieve its determined functionality.

A linearly polarized (LP) light with an angle of polarization φ as shown in inset of figure 4.1 can be written as a superposition of its circular components as follows:

$$\mathbf{E} = E_0\left(\hat{\mathbf{x}}\cos\varphi + \hat{\mathbf{y}}\sin\varphi\right) = \frac{E_0}{\sqrt{2}}\left(\hat{\mathbf{r}}e^{-i\varphi} + \hat{\mathbf{l}}e^{i\varphi}\right) \tag{4.1}$$

where $\hat{\mathbf{r}} = \left(\hat{\mathbf{x}} + i\hat{\mathbf{y}}\right)/\sqrt{2}$ and $\hat{\mathbf{l}} = \left(\hat{\mathbf{x}} - i\hat{\mathbf{y}}\right)/\sqrt{2}$ are the unit vectors of the RCP and LCP respectively. Equation (4.1) indicates that a phase delay of 2φ introduced to the RCP component with respect to the LCP component, this will cause a rotation of PA by a value of φ, and the PA will reverse from φ to $-\varphi$, if the RCP and the LCP coefficients are switched.

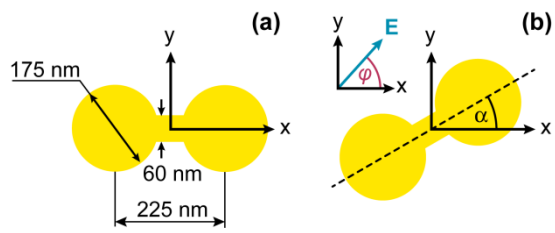

Fig. 4.1. Top-view schematic geometry of a single nano-antenna. (a) Designed dimensions of an elemental 30-nm thick nanoantentenna; (b) nano-antenna tilted at angle α with respect to x-axis. Inset: PA φ between the E-field and the horizontal (x-) axis. Light propagates perpendicular to the xy-plane (out of the figure plane).

Hence, the role of the proposed metasurface is to introduce a required phase shift between the LCP and RCP components. Our approach is to split the circular components, and then introduce optical path delay between them to obtain the required phase shift. To split the LCP and the RCP, we use the metasurface design shown in figure 4.2 which is made of an antenna array with a period of 8 antennas (shown in figure 1) such that any two adjacent antennas have a difference in α of 22.5^0. The individual antennas are

separated by 500 nm, hence forming a periodic supercell with a lattice constant (p) of 4 μm. It has been demonstrated[31] that such a metasurface, upon excitation with circularly polarized light, transmits two beams. A circular co-polarized beam is normally transmitted, while another cross-circular-polarized component is deflected in an anomalous direction by an angle $\theta = \sin^{-1}(\lambda/p)$ (direction of the first-order diffraction). A more detailed explanation of this effect is in the supporting information. It has also been shown[31] that the cross-circular-polarized term is deflected in the opposite direction when the incident beam is reversed from LCP to RCP, as shown in figure 4.2(a). Figure 4.2(b) shows the effect of exciting the metasurface with a linearly polarized light. By superposition of the cases in figure 4.2(a), the normal beams will add up to the same polarization state as the input, and the anomalous portion of the linearly polarized input beam is split into its circular components in two opposite diffraction directions. This is a very simple circular beam splitting structure supporting background-free circular components in two distinct diffraction directions.

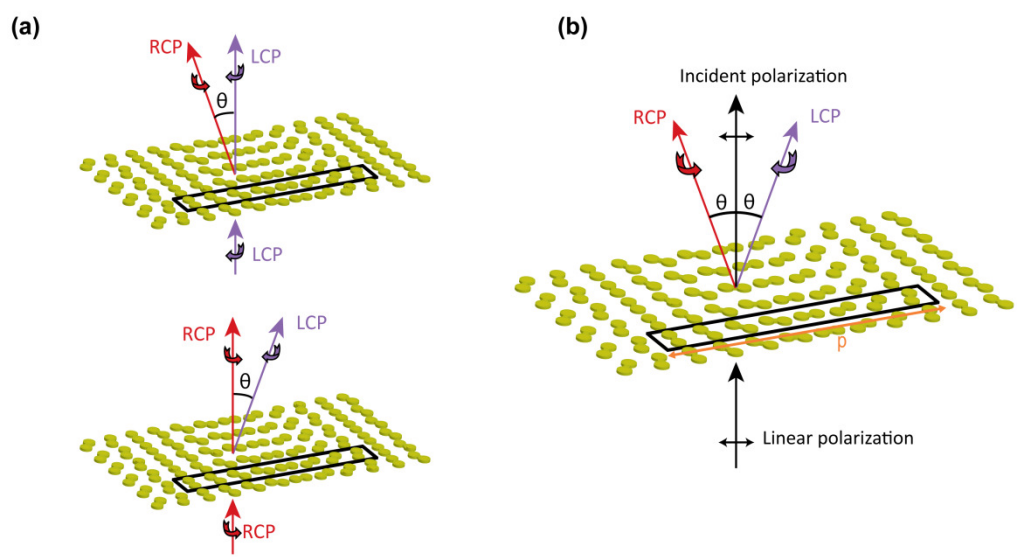

Fig. 4.2. Metasurface structure for circular beam splitting: (a) Effect of the metasurface on circularly polarized incident light, (b) Applying superposition to obtain circular beam splitting effect for linearly polarized incident light; a part of the beam is transmitted normally with no change.

The optical effect that is implemented in this work is the optical rotation of linearly polarized light, and to obtain it, we must take the structure described in figure 4.2 one step further. To retrieve linearly polarized light in the output in the anomalous direction, we use two sub-arrays of anisotropic nano-antennas rotating in opposite directions as shown in figure 4.3 (two sub-arrays in blue and red). This will cause the RCP from one sub-array to be directed parallel to the LCP obtained from the other one, and the two rays effectively retrieve a linearly polarized output ray. The two output rays are deflected at opposite angles of $\theta = \sin^{-1}(\lambda/p)$. An offset distance $d = p/4$ is introduced between the two sub-units to cause a π/2 phase shift between RCP and LCP, leading to a 45^0 rotation of the output angle of polarization according to equation (4.1). The value of the phase shift is π/2 because for the first order diffraction, the phase shift varies linearly with offset distance taking the value of $2\pi d/p$. The technique of using the offset distance to obtain a phase shift has been used before in different application to form a quarter wave plate[36]. The rotation of the PA is related then to the geometry by the formula:

$$Rotation\ Angle = 180^0 \times d/p \tag{4.2}$$

Equation (4.2) guarantees that the optical effect can be accurately determined by the designer and is immune against effects that could deteriorate the operation like changes to material properties due to temperature or fabrication.

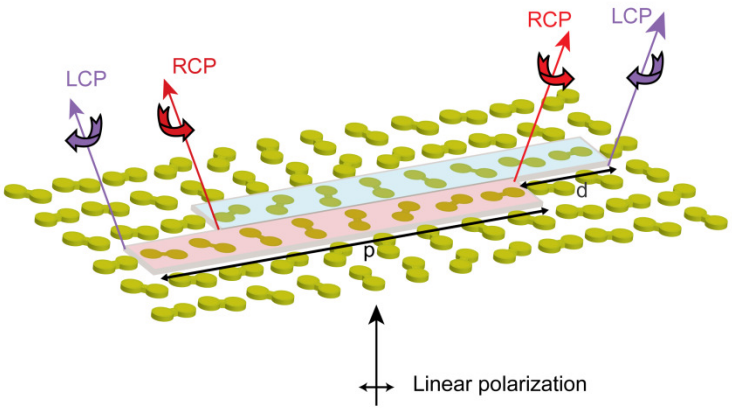

Fig. 4.3. The metasurface structure that performs optical rotation. It consists of two sub-arrays (in blue and red) causing circular polarization splitting in two opposite diffraction directions. In each diffraction direction, LCP and RCP add up to retrieve linear polarization. The two sub-arrays are separated by an offset distance *p*, causing a phase shift between the LCP and the RCP, which results in rotation of angle of polarization for the linearly polarized output light.

This concludes that we obtain a normally transmitted beam with unchanged state of polarization and other two anomalously transmitted beams deflected in opposite directions with the required state of rotation of PA by 45^0. Figure 4.4(a) demonstrates the overall performance of the metasurface subject to linearly polarized incident light.

Standard electron-beam lithography and lift-off processes are used to fabricate the array of gold nanoantennas on top of indium-tin-oxide coated glass substrate. Figure 4.4(b) is a field emission scanning electron microscope (FE SEM) image of the sample (a top view image taken from the gold nanoantenna side). Details of fabrication process are discussed in supporting information.

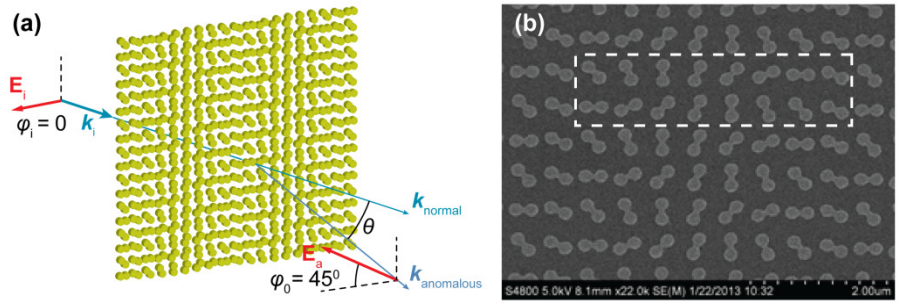

Fig. 4.4. (a) The overall action of metasurface structure that performs optical rotation. There is a normal output beam with the same polarization as the input, and one of two anomalous output beams of interest deflected by an angle θ and optical rotation occurs to that beam by an angle 45^0. (b) FE SEM top image of the fabricated sample with dashed rectangle to demonstrate the supercell.

The operation of the metasurface is first tested in the transmission direction as shown in figure 4.5(a). The incident ray is shown in black, the normally transmitted ray in blue, and the anomalously transmitted ray in red. The anomalous transmission is the ray of interest and it occurs at some deflection angle θ_t. The experimental setup contains a tunable monochromatic source providing signal in the near IR regime, a polarizer to control the PA of the incident light (φ_i), and a rotating analyzer which filters the output power at different PA's (φ_0) to determine its polarization state. More details about experimental setup are shown in supporting information. Measurements are taken using an ellipsometer device which allows rotation of detector to detect the anomalous ray as a function of deflection angle θ_t. The output and input PA's of this structure are related by the formula:

$$\varphi_0 = 45^0 - \varphi_i \tag{4.3}$$

The negative sign in equation (4.3) is coming from the switching from RCP to LCP and vice-versa in anomalous transmission with respect to incident beam as shown in figure 2(a), and this results in changing the sign of φ as discussed after equation (4.1). To test the rotation of the PA, we checked it with four specific values of incident PA which are φ_i = 0, 45^0, 90^0, 135^0 (-45^0). This is because these particular set of PA's uniquely

defines any state of linear polarization from Stokes' parameters. Figures 4.5(b) and 4.5(c) show a sample of the results at $\varphi_i = 0$, 45^0 and the total set of results are presented in the supporting information.

These measurements are taken at $\lambda = 1.5$ μm and the anomalous output beam intensity is plotted as a function of the scattering angle θ_t. The validity of equation (3) is verified by measuring the output without polarization filtering, and then filtering the output at two different PA's (φ_0) which are the polarization directions defined by equation (3) and the orthogonal direction. The results show that the power at the expected value of φ_0 coincides with the total power, and the power in orthogonal direction is almost zero verifying the required operation. The ratio between the power in the desired and orthogonal directions is about 20 dB.

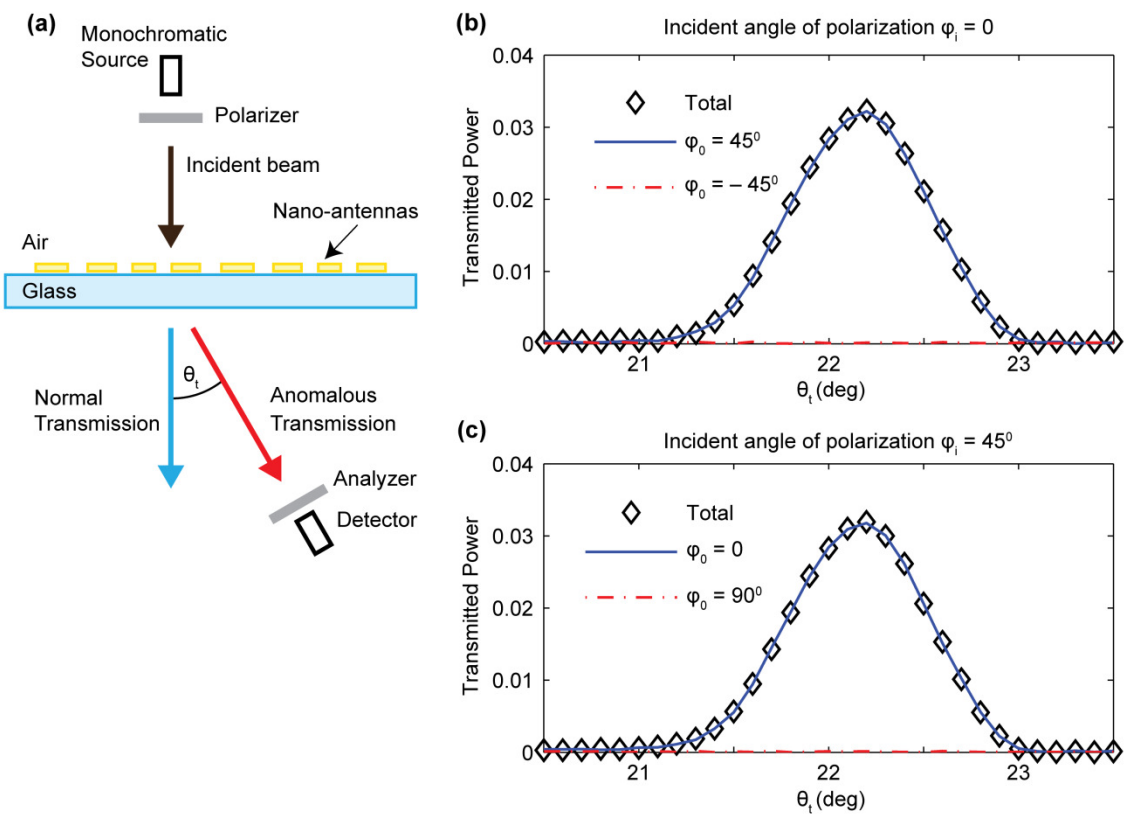

Fig. 4.5. (a) Schematics of the experimental setup for testing the metasurface in the transmission mode. (b) Experimental results for incident PA $\varphi_i = 0$ showing that output power is at $\varphi_0 = 45^0$. (c) Experimental results for incident PA $\varphi_i = 45^0$ showing that output power is at $\varphi_0 = 0$.

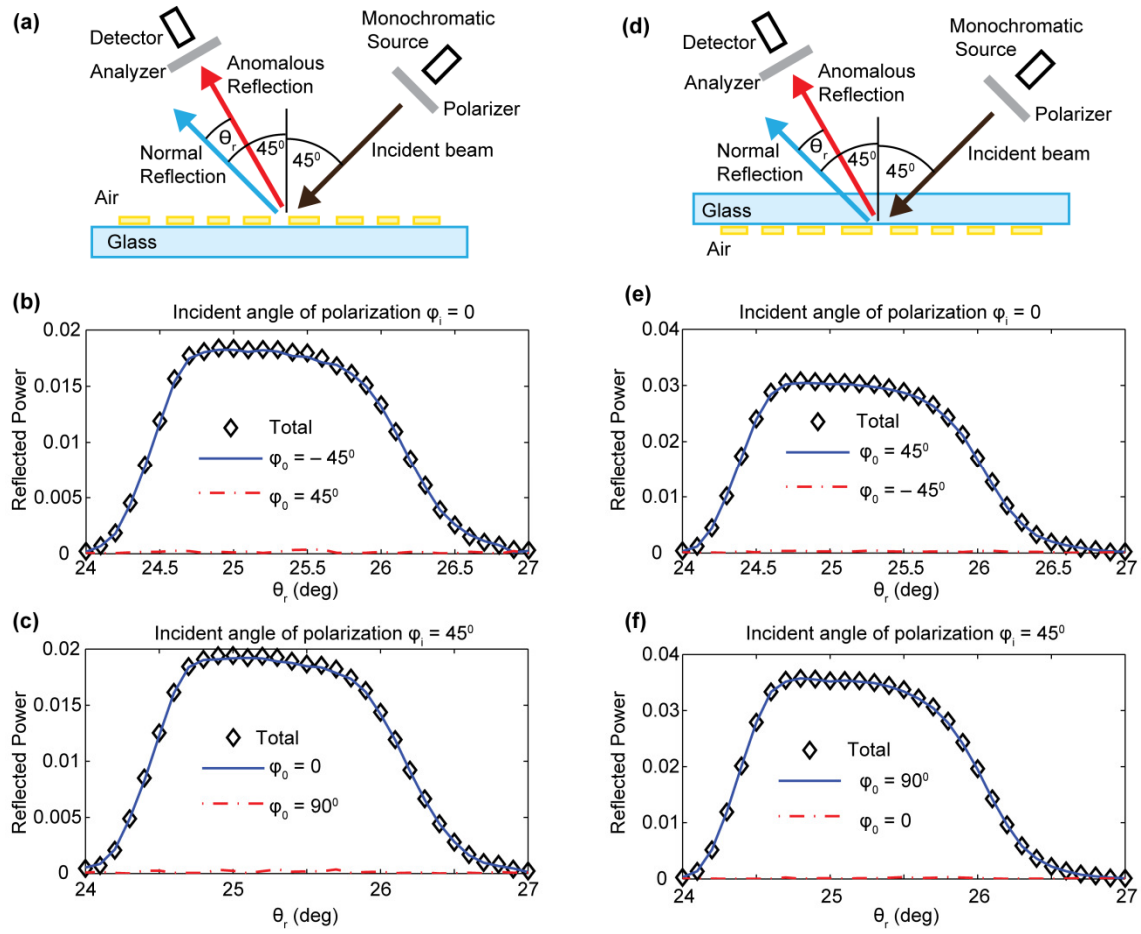

Fig. 4.6. (a-c) Experimental setup and results for testing the metasurface in the reflection mode from the nanoantenna side. For $\varphi_i = 0$, the output power is at $\varphi_0 = -45^0$, and for $\varphi_i = 45^0$, the output power is at $\varphi_0 = 0$. (d-f) The setup and observed results in the reflection mode from the glass side. For $\varphi_i = 0$, the output power is at $\varphi_0 = 45^0$, and for $\varphi_i = 45^0$, the output power is at $\varphi_0 = 90^0$.

The operation of the metasurface is then tested in the reflection direction as shown in figures 4.6(a) and 4.6(d). We need two sets of measurements from both the nanoantennas side and the glass side because the handedness of the antenna array in figure 4.3 is going to be flipped causing rotation of PA in opposite directions.

Since the reflected and transmitted circular components of light are of opposite polarizations, φ_0 of the anomalous reflected light incident from the nanoantenna side will

be opposite to the one of the anomalous transmitted light in equation (4.3), and is given by:

$$\varphi_0 = \varphi_i - 45^0 \tag{4.4}$$

Hence for the anomalous reflection from glass side, different handedness of the array will cause φ_0 to obey the formula:

$$\varphi_0 = \varphi_i + 45^0 \tag{4.5}$$

For the transmission case, it will be redundant to show results for light incident from both sides of metasurface owing to the reciprocity of transmission operation. Figure 6 shows the validity of equations (4.4) and (4.5) at $\lambda = 1.5$ μm for $\varphi_i = 0, 45^0$ – additional results are found in the supporting information. The output power in the desired anomalous beam was about 4%. It has been successfully demonstrated though that by utilizing metasurfaces in reflection mode, their output could be enhanced by an order of magnitude, and such designs are also applicable in our case.

To analyze how broadband is the effect, we test it for the case of transmission from nanoantennas side with the input angle of polarization $\varphi_i = 0$, which is the same case as in figure 5, but it's done for a set of wavelengths ranging from 1.05 μm to 1.7 μm. Outside this wavelength range, the performance deviates from the required functionality. Figure 4.7 shows the results for different wavelength values.

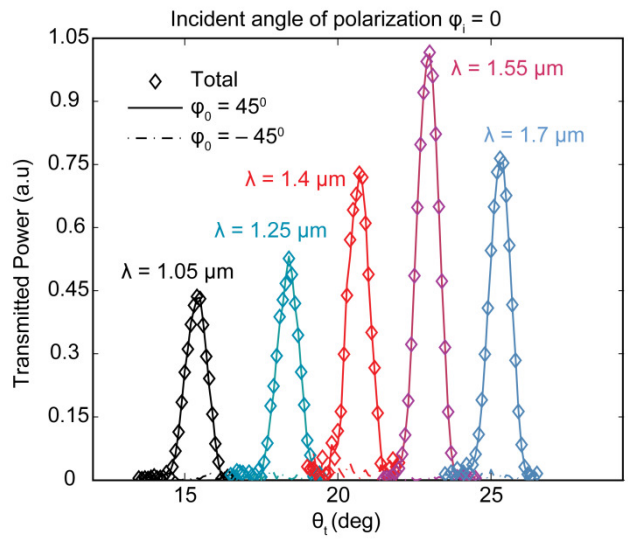

Fig. 4.7. Experimental results for transmitted power at different wavelengths, with normally incident light for incident PA $\varphi_i = 0^0$. The output power is at $\varphi_0 = 45^0$ similar to fig 4.5(b) for a broadband wavelength range from 1.05μm to 1.7μm. For each wavelength, the peak intensity occurs at a diffraction angle of $\theta = \sin^{-1}(\lambda/p)$.

4.3 Power Efficiency

Now, we implement similar polarization rotator using gap-plasmonic metasurface structure to obtain an order of magnitude enhancement in power efficiency. Using gap-plasmon [30, 60, 61, 147-149] (GP) nano-antennas NA instead, it is possible to obtain the same function with a compact subwavelength structure and dramatically improved power efficiency. With this design we're overcoming the poor power efficiency of single layered plasmonic metasurfaces such as those made with v-antennas[20]. There have been also earlier demonstrations of effective GP structures in the microwave regime [58, 150]. The unit cell of a gap-plasmon structure is shown in figure 4.8(a). It has a bottom gold layer that works as a reflecting mirror, a top 30-nm thick gold NA, and a 50-nm thick dielectric (alumina, Al_2O_3) spacer. The metal/dielectric/metal sandwich enables the excitation of a compact GP wave[60]. The incident plane wave couples to this slow GP wave which accumulates a large optical phase over the very short length of the NA. By tuning the aspect ratio (L_x/L_y) of the antennas geometry, we can indeed achieve a phase

delay of π between the reflection coefficients of the GP NA along its major and minor axes.

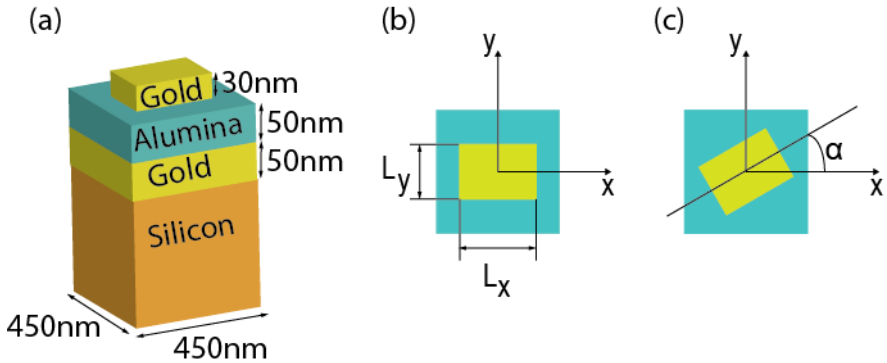

Fig. 4.8. (a) Schematic of a unit cell of a gap-plasmon based antenna structure consisting of gold/alumina/gold structure. Silicon substrate carries the metasurface and plays no role in the operation. (b) Top view of the unit cell, with nano-antenna dimensions $L_x = 280\ \mathrm{nm}$ and $L_y = 230\ \mathrm{nm}$. (c) Top view of the unit cell, with the nano-antenna tilted at an angle α.

Now, we design the metasurface with two intertwined sub-arrays as shown in fig 4.9(a). Each sub-array reflects LCP and RCP components in opposite directions, but due to the opposite antenna orientation of the two sub-arrays, they reflect opposite spins to the same side. At each reflection side, LCP and RCP from different sub-arrays add-up together to retrieve linearly polarized light. The two sub-arrays are spatially shifted with respect to each other to make a phase delay of $\pi/2$ to the RCP with respect to LCP, causing PA rotation by 45^0. Fig 4.9(b) presents a schematic of the whole metasurface demonstrating that, upon excitation with linearly polarized light, it reflects two different beams with rotated PA's.

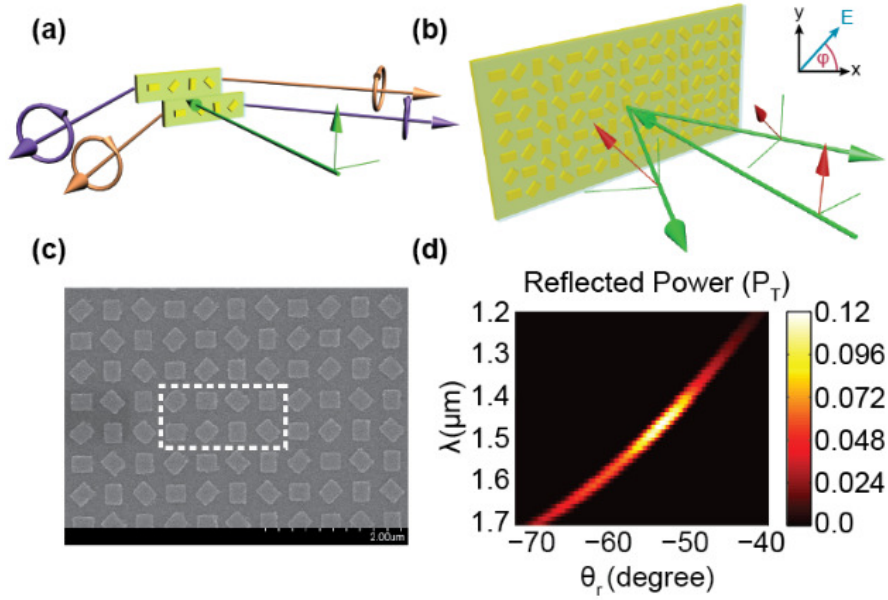

Fig. 4.9. Inset: PA φ between the E-field and the horizontal (x-) axis. (a) Schematics of one period of the metasurface consisting of two rows, where each row splits the incident beam by reflecting LCP (orange color) and RCP (purple color) into opposite sides. Alternating rows reflect opposite spins on the same side due to opposite gradient of antennas orientations. Displacement of alternating rows by quarter a period causes RCP phase delay with respect to LCP in both sides of reflections by $\pi/2$. (b) Schematics of the whole metasurface which performs optical rotation to the reflected beams by 45^0due to induced phase-shift between different spin components. (c) FE SEM of the metasurface with dashed lines representing one period. (d) Reflected Power from metasurface for the left reflected beam as a function of wavelength and reflection angle θ_r, showing that for each wavelength, maximum intensity occurs at $\sin\theta_r = -\lambda/P$.

The metasurface is fabricated on top of a silicon substrate, where the bottom 50 nm gold and the 50 nm alumina layers are implemented using electron beam deposition, and the 30 nm thick gold antennas are patterned using a standard electron beam lithography and lift off process. The experimental setup used to test the metasurface is shown in figure 4.10(a). It consists of a tunable monochromatic source, a polarizer, and a retarder to obtain circularly polarized incident beams. Measurements are taken using a

spectroscopic ellipsometer device which allows rotation of the detector to collect the reflected ray as a function of reflection angle θ_r.

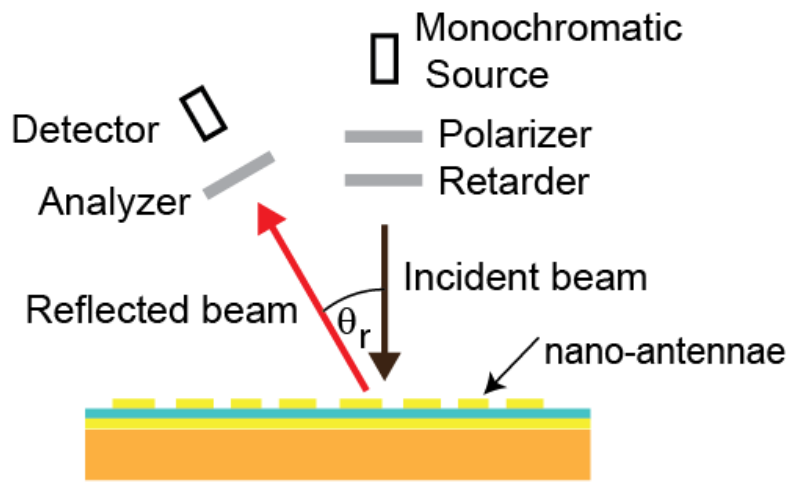

Fig. 4.10. Schematics of the experimental setup for testing the metasurface. A tunable monochromatic source, a polarizer, and a retarder are used to obtain circularly polarized incident beams for different wavelengths. Measurements are taken using a rotating arm device which allows rotation of detector to collect the reflected ray as a function of reflection angle θ_r.

The metasurface is tested using the same experimental setup in figure 4.10(a). The polarizer is used to provide incident beams with PA values of $\varphi_{\mathrm{i}} = 0^0, 45^0, 90^0, -45^0$. Then the analyzer is used to obtain the reflected power filtered at the PA φ_0 defined by equation (4.5) and at the orthogonal polarization state. Figures 4.11(a-d) show that the power ratio of the data filtered at the required PA is almost 100%, and nearly no power at the orthogonal PA. The ratio between power at the required polarization state to the orthogonal state is around 20 dB at $\lambda = 1.5\mu\mathrm{m}$, and the ratio deteriorates at the edge of the bandwidth due to a decrease in the output power.

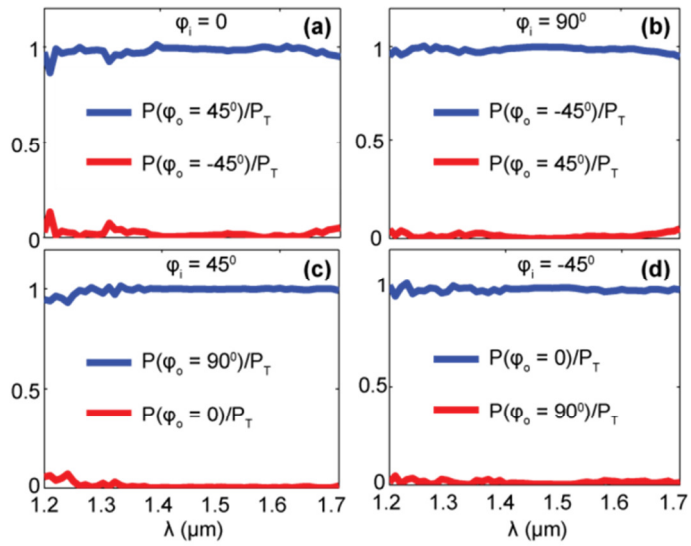

Fig. 4.11. (a-d) Polarization state results for incident PA values of $\varphi_i = 0^0, 45^0, 90^0, -45^0$ respectively. For each case, the ratio of the power at both the required polarization state and its orthogonal state with respect to the total power are plotted. Almost all the power is in the polarization state confirming the relation $\varphi_0 = \varphi_i + 45^0$, and almost no power at the orthogonal state. For each wavelength, polarization measurement was obtained at the angle of maximum reflected power of $\sin\theta_r = -\lambda / P$.

4.4 Conclusion

In conclusion, a broadband chirality effect using ultrathin metasurface has been demonstrated. The structure is simple because it does not utilize complicated chiral meta-atoms, but rather chirality is obtained through the specific arrangement of non-chiral elements in periodic supercells. A methodology of metasurface supercell design to manipulate helical components of light is presented, which enables quantitative description of chiral effects as a function of geometrical dimensions of the structure. Dependence on the supercell geometry rather than the intrinsic properties of the individual antennas provides functional immunity against fabrication and/or temperature effects. Utilizing gap-plasmonic metasurfaces enhances power efficiency by an order of magnitude. There is a possibility to obtain tunable chiral effects in the future using the presented approach by incorporating michro-electro-mechanical-systems (MEMS)

technology to allow control of the geometrical distances responsible for the effective chirality of metasurface.

5. METASURFACE BASED NANO-CAVITIES

5.1 Introduction

Semiconductor electronic devices are approaching their fundamental bandwidth and speed limitations, which is a serious problem that impedes further advances in many areas of modern sciences [162]. One solution is believed to be in replacing electronic signals with light, which is the ultimate means of sending information to and from the interior structure of materials — it packages data in a signal of zero mass and unmatched speed [163]. However, the major problem of using light as an information carrier is the low level of miniaturization and integration caused by the diffraction limit [162], and therefore, research in nano-photonics has been focusing on solving this obstacle. Several solutions involve surface plasmon polariton (SPP) waves. However, plasmonic waves suffer from high losses, and poor coupling efficiency with radiating plane electromagnetic waves due to mode mismatch [162]. In this work, cavities with reflective metasurface claddings are proposed as a compromise between plasmonic and conventional photonic resonators regarding size-losses tradeoff. This is attributed to the fact that these cavities carry hybrid modes; plasmonic modes at the reflecting metasurface and photonic modes in the rest of the cavity body. The proposed nano-cavities are compact and sub-wavelength, and at the same time they match with the conventional photonic devices for the end-user. In the following sections, we give a description of how the metasurface claddings can be used to decrease cavity thickness. And then we show that the potential of these metasurface based nano-cavities exceeds the ability to miniaturize the cavity size, and can be tailored to resonate at multiple wavelengths.

In addition to the goal of scaling down the size of optical components, minimizing the cavity size below the diffraction limit has other numerous applications including

realization of nano-lasers, and spontaneous emission rate enhancement due to the Purcell effect[164]. This effect, which is inversely proportional to the volume of the cavity, is useful in single photon sources, and in thresholdless lasing[165]. This has motivated researchers in nanophotonics to search for solutions to minimize cavity size[166, 167].

We propose a method to achieve subwavelength dimensions of cavities using reflecting metasurfaces. We change the constraints for cavity resonance by replacing the conventional mirrors with reflecting metasurfaces that introduce an arbitrary phase shift to the reflected wave. This changes the roundtrip phase condition. Here, we present design of metasurface based nano-cavities based on gap plasmon resonances. These cavities have a thickness of 100 nm and support resonances in the wavelength range of 0.6 – 1.1 μm. Then we develop the technique to make the nano-cavities resonate at two different wavelength values which can be tailored independently through adjusting the geometry of the metasurface.

5.2 Compact Nano-cavities

Light confinement in conventional cavities, such as Fabry-Pérot cavities made of parallel mirrors, should satisfy a resonant condition of having a round trip phase shift of an integer multiple of 2π. This implies that the cavity should have a thickness equal to an integer number of half the wavelength, setting a lower limit of the thickness of the cavity to $\lambda/2$. Fig 5.1 shows a comparison between a conventional Fabry-Pérot resonator (fig 4.1a) and the proposed structure where one or both mirrors are coupled to a metasurface (fig 5.1b) which add an arbitrary phase shift of φ_{ms}. In the conventional case, the resonance condition is $4\pi L/\lambda = 2m\pi$ imposing a minimum limit of $\lambda/2$ on the value of L, while for the proposed structure, the resonance condition will become $4\pi L/\lambda + \varphi_{ms} = 2m\pi$. Since φ_{ms} can be designed to take any value from 0 to 2π, there is no constraint on L and it can be made arbitrary small.

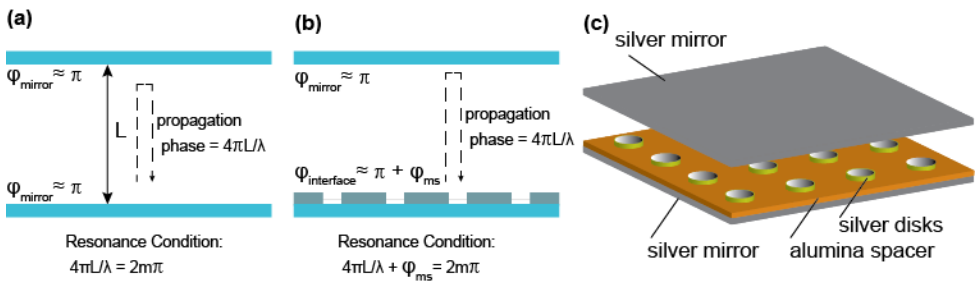

Fig. 5.1. Comparison in phase and resonance conditions between: (a) conventional resonator (b) resonator with reflecting metasurface. (c) 3D view of a specific cavity design based on gap plasmon resonance.

One of the options to implement the design in fig 5.1(b) is to use gap-plasmon resonance structure[59, 60]. Gap plasmon metasurfaces can be used to introduce any phase shift from 0 to 2π. Fig 5.1(c) shows a 3D view of our cavity structure and fig 5.2(a) shows its cross-section. The cavity structure consists of a bottom reflecting metal layer having a thickness *t* which is on the order of 20 – 30 nm, and an array of metal disks of diameters *D*, periodicity *P*, and thickness *h*, separated from lower mirror by a dielectric spacer layer of thickness *s*. Thicknesses *h* and *s* typically range over a few tens of nanometers. Periodicity *P* and diameter D ranges depend on the wavelength of operation. Working in the visible and Near IR range would make typical values of *P* from 100 - 300 nm, and *D* about 30 – 70% of the value of *P*.

Below are FEM simulation results for the cavity structure with the materials shown in fig 5.1(c) and fig 5.2(a), where P = 100 nm, h = 20 nm, L = 60 nm, s = 20 nm, and t = 25 nm, and all the metals are silver and the spacer is alumina and the rest of the cavity is filled with PMMA. Changing the value of *D* results in changing the wavelength of the gap plasmon resonance, and hence, changes the cavity resonance wavelength as shown in fig 5.2(b).

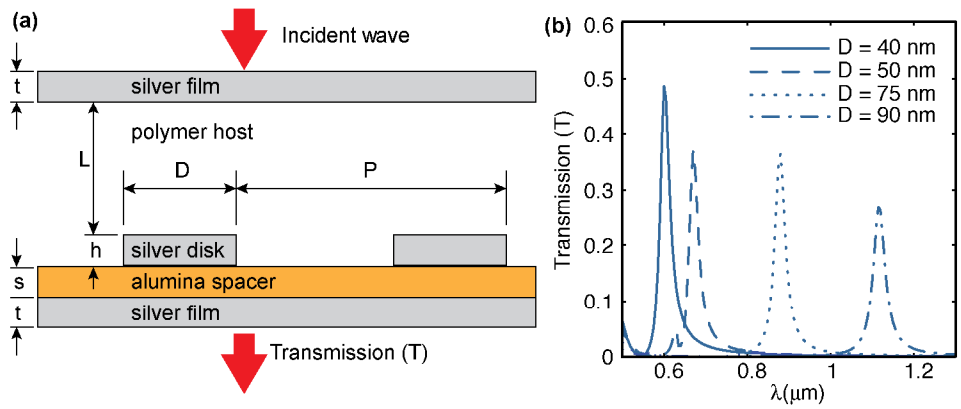

Fig. 5.2. (a) Cross-section of cavity structure and demonstration of the plane-wave excitation used in simulation (b) simulation results for the diameter of silver disk D = 40, 50, 75, and 90 nm.

Cavities with distance between mirrors of 100 nm have shown the ability to support resonances in visible and Near IR wavelengths.

Similarly, we can obtain similar response with using nano-stripes instead of nano-disks. It work with one polarization direction only, but it enhances power efficiency of the structure. Figure 5.3(a) shows a schematic of the structure, and figure 5.3(b) shows simulation results for different dimensions of nano-stripes. The thicknesses of all layers are the same as the previous isotropic structures, and the stripes are repeated at a period of 125 nm.

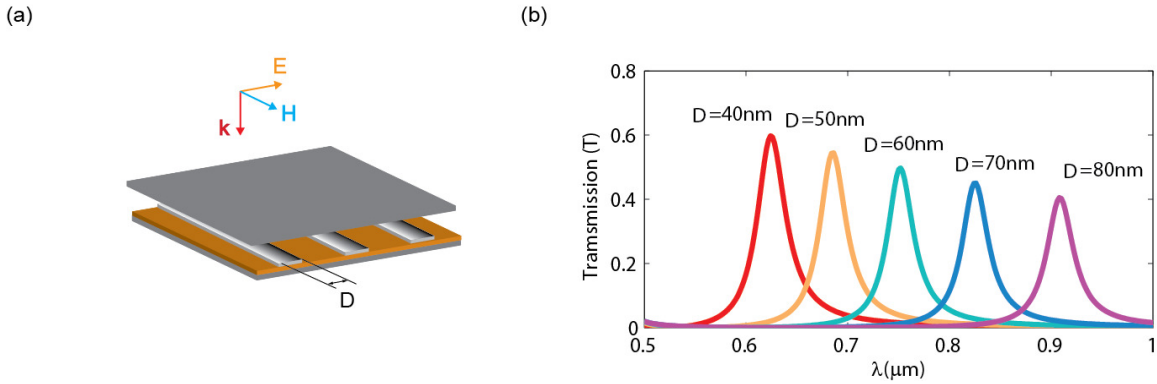

Fig. 5.3. (a) Nano-cavity structure with nano-stripes and demonstration of the plane-wave excitation used in simulation (b) simulation results for the width of silver stripes D = 40, 50, 60, 70 and 90 nm.

5.3 Dual-Band Nano-cavities

The capabilities of the metasurface based nano-cavities exceed the ability of building nano-photonic devices below the diffraction limit. The heart of these class of cavities lies in changing the resonant phase condition to $4\pi L/\lambda + \varphi_{ms} = 2m\pi$. In the previuos cavities, the metasurface induced phase term φ_{ms} go through large variations around the gap-plasmon resonance wavelength determined by the dimension D. If we use two different stripe widths D_1 and D_2, we can have two resonances at different wavelengths. Figure 5.4 demonstrates that we can tune the two resonant wavelengths independently by tuning either D_1 or D_2.

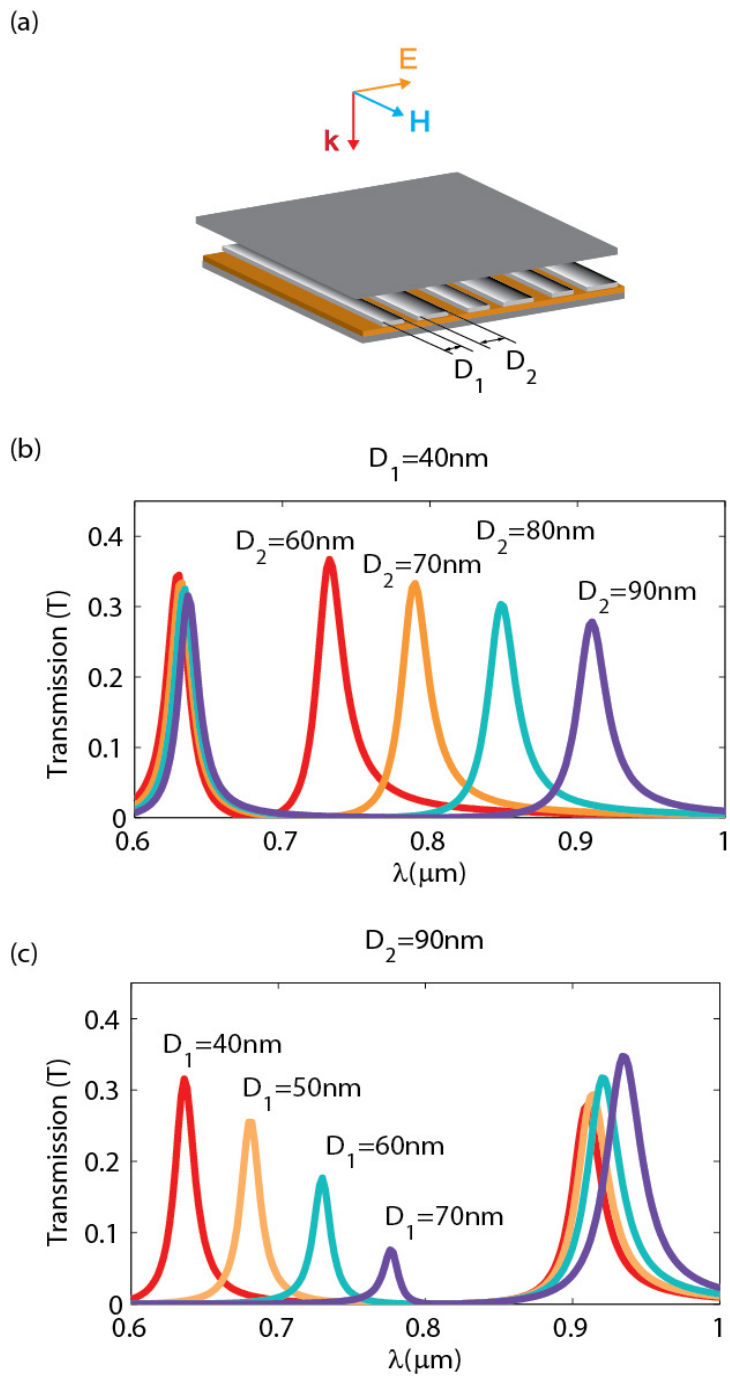

Fig. 5.4. (a) Nano-cavity structure with nano-stripes of two different width D_1 and D_2 tailored to resonate at two wavelength. (b) Simulation results while fixing the smaller width D_1 and varying D_2. (c) Results with different D_1 for same D_2.

5.4 Conclusion

Subwavelength cavities are obtained using reflecting metasurfaces. 100 nm thick cavities are shown to support resonances in visible and Near IR wavelengths using gap plasmon resonators attached to cavity walls. The effect can be used in many applications, including but not limited to, spontaneous emmision enhancement, single photon sources, nano-lasers, thresholdless lasing and in development of subwavelength cavity-based optical devices like interferometers, optical parametric oscillators, and pulse shapers.

By adjusting the nano-structures inside the metasurface, it can be tailored to resonate at multiple wavelengths . Metasurface based nano-cavities where designed to operate at dual wavelength bands. In contrast to the case of conventional cavities, the two resonant wavelength can be tailored independently and don't need to be integer multiples of each other.

The metasurface nano-structures also have the potential to be tailored to resonate only at specific polarizations, spin or angular momentum modes. Metasurface based nano-cavities can perform new operations not familiar with conventional cavities like spin-dependent cavities that resonate for only a specific spin or resonating at a specific laser mode profile.

6. TIME-GRADIENT METASURFACES AND LORENTZ NON-RECIPROCITY

6.1 Introduction

A cornerstone equation of optics – Snell's law – relates the angles of incidence and refraction for light passing through an interface between two media. It is built on two fundamental constrains: the conservation of tangential momentum and the conservation of energy. By relaxing the classical Snell's law photon momentum conservation constrain when using space-gradient phase discontinuity, optical metasurfaces enabled an entirely new class of ultrathin optical devices. Here, we show that by eradicating the photon energy conservation constrain when introducing time-gradient phase discontinuity, we can further empower the area of flat photonics and obtain a new genus of optical devices. With this approach, classical Snell's relations are developed into a more universal form not limited by Lorentz reciprocity, hence, meeting all the requirements for building magnetic-free optical isolators. Furthermore, photons experience inelastic interaction with time-gradient metasurfaces, which modifies photonic energy eigenstates and results in a Doppler-like wavelength shift. Consequently, metasurfaces with both space- and time-gradients can have a strong impact on a plethora of photonic applications and provide versatile control over the physical properties of light.

Optical metasurfaces have produced a strong impact on nanophotonic devices resulting from the generalization of Snell's relation**[19]**, which has always played a primary role in the design of optical devices. Snell's law relates the angles of incidence and refraction for light passing through an interface between two distinct isotropic media and it is a direct result of two fundamental laws**[168]** for reflected and refracted photons dealing with the conservation of (i) tangential momentum, and (ii) energy. With the

inception of space-gradient metasurfaces, created using nano-antennas that introduce spatially dependent phase-discontinuities along the interface, Snell's law has been generalized to include a discontinuity in the tangential momentum. Consequently, it has already become possible to engineer angles of reflection and refraction at will with flat, ultra-thin metasurfaces.

By introducing a dynamic (i.e. temporal) change to the phase-discontinuity, Snell's law can be modified to an even more universal form, which is expected to lead to other new and exciting physical impacts. As we will show, photons interacting with time-gradient metasurfaces do not conserve their energy. As a result, there is a change in the normal momentum component induced by the energy-momentum dispersion relation in the media on both sides of the metasurface. Therefore, using both space and time variation of phase induced by metasurfaces, it is possible to control both the tangential and normal momentum components. Beside the extra degree of freedom of controlling the normal momentum, the modification to Snell's law contributed by a time variation of the phase-shift breaks Lorentz reciprocity[169]. This enables the implementation of optical devices, such as optical isolators, which require breaking time-reversal reciprocity[170, 171] and thus are unachievable with space-gradient metasurface alone.

First, we derive the mathematical apparatus for the generalized reflection and refraction using space and time phase-shift variation along metasurfaces. Then, the non-reciprocity of a new form of Snell's law is highlighted, and possible schematics for designing optical isolators using time-varying metasurfaces are proposed. Finally, new physical effects induced by the time variation of phase discontinuity are discussed and possible implementation techniques are proposed.

6.2 Mathematical Formulation

Snell's law is a geometric optics approximation, which is exact when we are dealing with ideal plane waves. It still is very accurate, however, if the wave amplitude is slowly varying in space with respect to wavelength scale, and in time with respect to the period.

In this case, electromagnetic waves can be viewed as a collection of local rays in space and time. The wave approximation corresponding to geometric optics is given by[169]:

$$\mathbf{E} = \mathbf{a}e^{i\psi} \tag{6.1}$$

where $\mathbf{a}$ is a slowly varying function of space and time (constant in case of plane waves), and the phase term ψ(also called the eikonal in geometric optics) is a fast varying function of space and time. The spatial and temporal derivatives of ψ give the frequency and wave vector of the wave, respectively[169]:

$$\omega = -\frac{\partial \psi}{\partial t} \tag{6.2}$$

$$\mathbf{k} = \nabla \psi \tag{6.3}$$

We study the most general case shown in figure 1, when a wave with a phase of ψ_i is incident on a metasurface, which induces a space-time varying phase-shift of $\psi_{ms,r}$ for a reflected wave and $\psi_{ms,t}$ for refracted (transmitted) wave. This means that the phases of the reflected and transmitted waves are given by:

$$\psi_{\mathrm{s}} = \psi_{\mathrm{i}} + \psi_{\mathrm{ms,s}},\ \mathrm{s} = \{\mathrm{r,t}\}. \tag{6.4}$$

By applying equations (6.2) and (6.3) to both sides of equations (6.4), we obtain:

$$\omega_{\mathrm{s}} = \omega_{\mathrm{i}} - \partial\psi_{\mathrm{ms,s}}/\partial t,\ \mathrm{s} = \{\mathrm{r,t}\}; \tag{6.5}$$

$$k_{\mathrm{s},x} = k_{\mathrm{i},x} + \partial\psi_{\mathrm{ms,s}}/\partial x,\ \mathrm{s} = \{\mathrm{r,t}\}, \tag{6.6}$$

where ω_i, ω_r, ω_t, $k_{i,x}$, $k_{r,x}$ and $k_{t,x}$ are the frequencies and the x-components of the wave-numbers of incident, reflected and transmitted waves, respectively. Equation (6.6) can be rewritten in terms of the wavenumbers' amplitudes k_i, k_r, and k_t as follows:

$$k_r \sin\theta_r = k_i \sin\theta_i + \frac{\partial\psi_{ms,r}}{\partial x} \tag{6.7}$$

$$k_t \sin\theta_t = k_i \sin\theta_i + \frac{\partial\psi_{ms,t}}{\partial x} \tag{6.8}$$

where $k_i = n_i\omega_i / c$ and

$$k_{\mathrm{s}} = \frac{n_s\omega_{\mathrm{s}}}{c} = \frac{n_s}{c}\left(\omega_{\mathrm{i}} - \frac{\partial\psi_{\mathrm{ms,s}}}{\partial t}\right), \ \mathrm{s} = \{\mathrm{r,t}\}, \tag{6.9}$$

with $n_i\left(= n_r\right)$ and n_t being the refractive indices of the incident and transmissive media, respectively. The forms of equations (6.7) and (6.8) which calculate angles of reflection and refraction are very similar to the equations introduced by space-gradient metasurfaces, but there is an important difference illustrated by formula (6.9). This equation implies that the amplitude of the wavenumbers is changing with the change of frequency (resulting from time variations of phase).

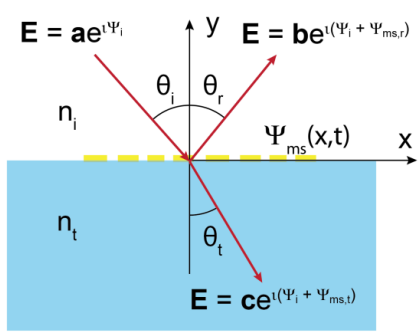

Fig. 6.1. Schematic of a light beam incident on a space-time gradient metasurface with angle of incidence θ_i, reflected beam with angle of reflection θ_r, and transmitted (refracted) beam with angle of transmission (refraction) θ_t.

The above equations clearly indicate that the space-gradient phase-shift introduces an abrupt change to the photonic momentum with a value of $\Delta p_x = \hbar \Delta k_x = \hbar\, \partial \psi_{ms} / \partial x$, and similarly, a time-gradient phase-shift causes a photonic energy change of $\Delta E = \hbar \Delta \omega = -\hbar\, \partial \psi_{ms} / \partial t$. This Doppler-like shifting of the wavelength in time-varying metasurfaces enables alternative approaches that could be advantageous over mechanical movement. They can also be integrated with mechanical systems to modify or compensate the Doppler effect. Interesting and useful developments can be also related to cavity optomechanics[172], where time-varying metasurfaces could be utilized to expand the control over the inelastic photonic interactions with vibrating mirrors. Here the exchange of energy with photons could be used for laser cooling[173] or heating. Figure (6.2) illustrates a basic paradigm for the universal Snell's law with space-gradient and time-gradient metasurfaces. For the sake of simplicity and clarity, we discuss reflection from gradient metasurfaces in free space. A similar analysis can be extended to transmittance and for arbitrary media. Figure 6.2(a) demonstrates the photonic interaction with a space-gradient metasurface, where a discontinuity of tangential momentum (or wavenumber) is added to the reflected photons. Conservation of energy requires the amplitude of the total momentum to remain on the same isofrequency curve $\sqrt{k_x^2 + k_y^2} = \omega / c$ (or iso-energy curve $\sqrt{p_x^2 + p_y^2} = E / c$). The tangential and total momenta together define the new angle of reflection (solid line) which is different than the reflection angle with no metasurface (dashed line). Figure 6.2(b) demonstrates another degree of freedom to control the reflection of the beam using a time-gradient metasurface which, according to equation (6.5), introduces a change to the iso-frequency curve of the reflected photons. If there is no space-gradient phase shift introduced, then the tangential momentum would not change; however, the variation in frequency results in a change in the normal component of the momentum (solid line) compared to the case when the photon energy is conserved (dashed line). Figures 6.2(c-d) compare two examples of reflection tests upon time-reversal and demonstrate that unlike space-gradient metasurfaces, time-varying metasurfaces can provide non-reciprocal reflectance. Figure 6.2(c) illustrates that the variations induced in the tangential momentum by the space-

gradient metasurface for the forward and reverse directions compensate each other. Thus, if a space-gradient metasurface adds a tangential momentum to the forward beam (Fig 6.2(a)), it subtracts the same amount in the reverse beam (Fig 6.2(c)), restoring the original incident direction. This is not the case for time-varying metasurfaces where the changes in the isofrequency curve are additive for both directions and do not negate each other. If the amplitude of the wavenumber is increased for the forward beam (Fig 6.2(b)), it is further increased to a higher value for the reversed beam (Fig 6.2(d)), leading to a deviation of the time-reversed reflected beam from the incident beam.

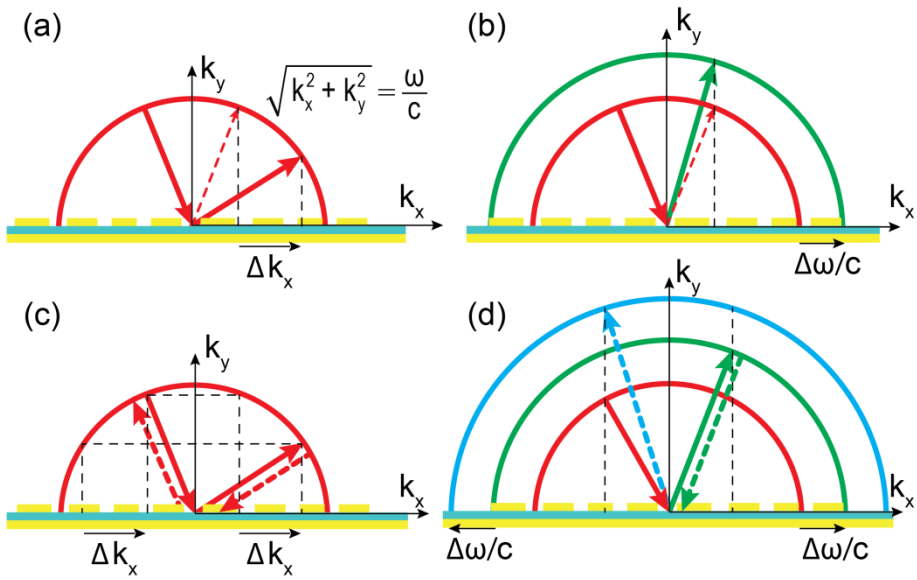

Fig. 6.2. (a) Light reflected from a space-gradient metasurface inducing tangential momentum discontinuity. The dashed red line represents the reflected beam without the metasurface effect. (b) Light reflected from a time-gradient metasurface inducing energy discontinuity and changing the isofrequency curve. The dashed red line represents the reflected beam without the metasurface effect. (c) Time-reversal test of a space-gradient metasurface. Red dashed line denotes reciprocal propagation of light. (d) Performance of a time-gradient metasurface in time-reversal with the dashed green and blue lines denoting the nonreciprocal traces of the incident and reflected beams respectively.

6.3 Lorentz Non-Reciprocity and Optical Isolation

Now, we quantify the amount of non-reciprocal deviation in the propagation direction for the case illustrated in Fig 6.2(d). For simplicity, we assume that there is no space-varying phase-shift ($\partial\psi_{ms}/\partial x = 0$), and that there is a linear variation of ψ_{ms} with respect to time with a derivative value of $\Delta\omega = -\,\partial\psi_{ms}/\partial t$. This can be obtained by introducing a periodic phase shift that changes linearly from π to $-\pi$ during a period $T = 2\pi/\Delta\omega$. Let the angles of incidence and reflection to this metasurface be θ_1 and θ_2 as shown in Fig 6.3(a). By applying equations (6.5) and (6.9), we derive that if the frequency and the wavenumber of the incident beam are ω and $k = \omega/c$, respectively, then the frequency and the wavenumber of the reflected beam are $\omega + \Delta\omega$ and $k + \Delta k = (\omega + \Delta\omega)/c$. Then, from equation (6.7), we obtain:

$$k \sin\theta_1 = (k + \Delta k)\sin\theta_2 \tag{6.10}$$

Using the same analysis for the time-reversal case shown in Fig 6.3(b) we find:

$$(k + \Delta k)\sin\theta_2 = (k + 2\Delta k)\sin\theta_3 \tag{6.11}$$

From equations (6.10) and (6.11) it follows that:

$$\sin\theta_3 = \frac{\sin\theta_1}{1 + \dfrac{2\Delta k}{k}} = \frac{\sin\theta_1}{1 + \dfrac{2\Delta\omega}{\omega}} \tag{6.12}$$

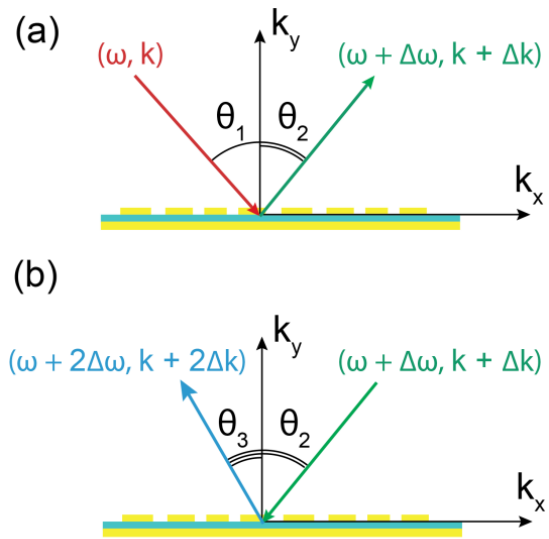

Fig. 6.3. (a) Schematics of reflection angle from a time-gradient metasurface. (b) reflection angle in time-reversal.

From equation (6.12) it can be concluded that the back reflected beam in time-reversal is not propagating in the same direction as the incident beam. Consequently, this type of metasurface can be used as a unidirectional isolator with two ports 1 and 2 placed along the directions of the incident beam at θ_1 and the reflected beam at θ_2, respectively. Light is allowed to propagate in the forward direction from port 1 to port 2, while light backscattered from port 2 is redirected at an angle away from port 1, enabling scattering parameters of $S_{21} > 0$ and $S_{12} \approx 0$, which is required for optical isolation[171]. Equation (6.12) demonstrates that the separation between θ_1 and θ_3 is proportional to the ratio $\Delta\omega/\omega$ which is very easy to control while operating in the radio frequency and possibly terahertz. For operation in the infrared and visible bands, considerable ratios of $\Delta\omega/\omega$ can be obtained when, for example, time-varying metasurfaces are modulated optically. We note that non-reciprocity attributed to the difference in photonic energy levels (frequencies) between the incident and back-scattered beams can be completely decoupled using trivial optical filtering with a high-quality-factor optical cavity. In this case even a small change in the frequency would provide an observable effect. Figures 6.4(a) and 6.4(b) depict the schematic of an optical isolator based on a metasurface with a

frequency shift of $\Delta\omega = -\ \partial\psi_{ms}/\partial t$ and two optical resonators with center frequencies of ω and $\omega + \Delta\omega$. Figure 6.4(a) shows the allowed forward propagation for an incident beam of frequency ω and the reflected beam of frequency $\omega + \Delta\omega$, where both beams pass through the optical resonators. Figure 6.4(b) presents the backward propagation of the time-reversed $\omega + \Delta\omega$ beam, which is reflected at a shifted frequency of $\omega + 2\Delta\omega$ and hence, the reversed beam is blocked by the resonator.

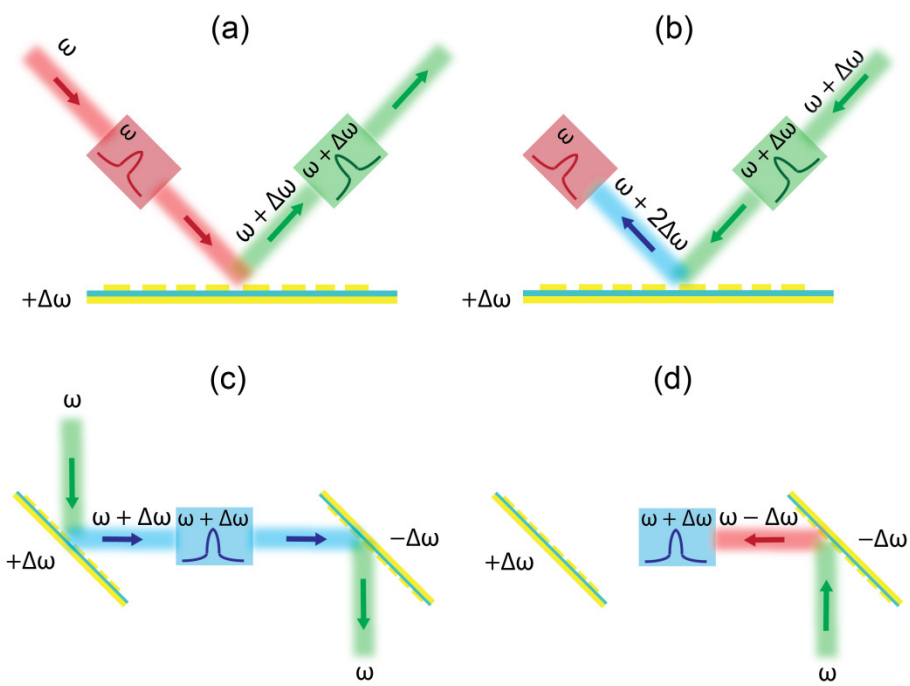

Fig. 6.4. (a,b) Schematics of an optical isolator with uni-directional light flow using a time-varying metasurface and two high quality resonators. (c,d) An optical isolator with same input/output frequency using two time-varying metasurfaces and a high quality resonator.

To build an isolator with the same input and output frequencies, one can use two metasurfaces with the same magnitude but opposite in sign phase-shifts. Thus, one achieves frequency shifts of $+\Delta\omega$ and $-\Delta\omega$, respectively, which compensate and restore the same frequency in the output. Inserting a resonator tuned at $\omega + \Delta\omega$ in the path of light between the two metasurfaces, would allow forward propagation of light (Figure 6.4(c)) and block its backward propagation (Figure 6.4(d)).

The examples proposed in Fig 6.4 demonstrate straightforward approaches to designing compact, magnetic-free optical isolators with time-varying metasurfaces. Generally, these isolators would require either the utilization of non-linear or time-varying materials[171]. Due to some limitations on nonlinear isolators[174] such as intensity dependent operation, there is interest in developing isolators based on time-varying structures[175-178]. We believe that ultra-thin metasurfaces with dynamically induced phase-shift can be advantageous over bulk time-varying structures.

6.4 Conclusion

In conclusion, time-varying metasurfaces bring a new degree of freedom in controlling light with flat photonic devices that further broadens the scope of applications for metasurfaces. While space-gradient metasurfaces enable the control of the tangential momentum, space-time-gradient metasurfaces are capable of controlling both the photonic energy (normal momentum) and the tangential momentum. As a result, time-gradient metasurfaces go beyond the physical limitations imposed on space-gradient metasurfaces like reciprocity and 'elasticity' of the reflected and refracted photons. We illustrated that time-gradient metasurfaces can break Lorentz reciprocity, enabling the development of optical isolators, and derived a universal non-reciprocal form of Snell's law. Photons interacting with time-varying metasurface exhibit Doppler-like wavelength shift causing exchange of energy. This is similar to the effect induced by vibrating mirrors in opto-mechanical cavities, where energy exchange with photons is used, for example, for laser cooling. Additionally, time-varying metasurfaces can be integrated with time-reversal mirrors[179-181] and used for subwavelength focusing[182] enabling the mapping of backward-signals or far-field images. For radio-frequency and microwave applications, the temporal modulation of metasurfaces can be achieved for example by using an array of varactor-based phase-shift elements. Optical implementations are possible by using, for example, electroptic and photoacoustic effects as well as other available modulation techniques.

7. ULTRAFAST LASER BEAM STEERING

7.1 Introduction

In the previous chapters, many demonstrations of metasurface based devices have been accomplished through *spatial engineering* of properties of a medium. And in the previous chapter, it has been demonstrated that the field of metasurfaces can be further empowered by utilizing *time-varying* structures with a dynamic response to propagating light. A new genus of optical devices and physical effects can be realized provided one can overcome some fundamental limitations of metasurfaces which only utilize spatial variations of structures. Nano-structured metasurfaces exhibit spatial variation of a structure over small scales which are subwavelength, and this is a prime cause for achieving their functionalities. It is, therefore, a sensible approach to utilize ultrafast technology to obtain dynamic response on a short time scale to obtain considerable effects of dynamic devices.

Metasurfaces achieve their functionalities through spatial interference of light emitted from an array of antennas. Similar interference effects are implemented in pulse shaping of ultrashort pulses, but in time-domain instead. In this chapter, a new approach is introduced to integrate the spatial interference methodology of metasurfaces with the temporal interference methodology from ultrafast pulse shaping to enable a new spatiotemporal interference effect. This effect is utilized to demonstrate ultrafast beam steering within a time period of hundred picoseconds.

7.2 Spatiotemporal Interference

Metasurface based applications like light bending[23] and holograms[34] depend on spatial interference from an array of antennas to produce a far field holographic pattern.

The requirement for spatial coherence typically imposes a monochromatic source, but this leads only to static far field patterns (i.e. we can achieve beam bending to a fixed angle, not a dynamic beam steering). On the other hand, pulse shaping of ultrafast optical pulses is performed using similar interference technique but in time-domain. It's done by controlling their spectral components of light such that the coherent interference of these components in time generates the required temporal pulse. The spectral components of ultrashort pulses consist of a frequency comb which is a series of discrete equally spaced spectral lines. The art of pulse shaping[183] is accomplished through Fourier synthesis by judiciously adjusting the complex coefficients (phase and/or amplitude) of these spectral components such that their temporal interference will compose the predesigned pulse shape.

Here, we demonstrate that if we incorporate spatial variation of spectral components in addition to time control, we can obtain ultrafast space-time beam shaping which can generate dynamic far-field patterns. Using this methodology, steering of laser beams becomes possible with the same period of ultrafast pulses repetition rate, which is 3-4 orders of magnitude faster than state-of-the-art beam steering. Fig. 7.1 demonstrates a conceptual image of spatiotemporal interference devices, where ultrashort pulses are being utilized to provide phase-locked frequency combs which are demultiplexed, then are used to feed a metasurface with nano-slits or nano-holes. The metasurface acts as a new source of phase locked waves that coherently interfere in the far field to generate dynamic optical patterns.

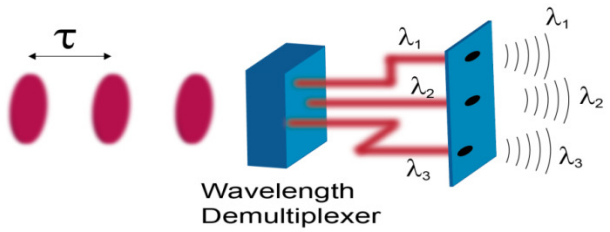

Fig. 7.1. Conceptual demonstration of an ultrafast metasurface. An ultrashort pulse is applied and demultiplexed. Its phase locked frequency components are fed to the nano-hole metasurface which acts as a secondary source of the frequency components. Far field interference of these waves generates an ultrafast beam pattern.

Dynamic patterns were typically obtained through modulating the spatial phase distribution of the holographic plate using liquid crystal modulators[67, 184] or acousto-optic modulators[185] whose speeds are limited by the modulating speed of each technology. Here, we provide an alternative ultrafast approach through interference of sources of multiple frequencies (frequency comb) as long as they are mode-locked to keep the required coherence. We will demonstrate the concept using a very simple case used to achieve ultrafast beam steering, then we will propose a scheme for implementation and experimentation.

7.3 Mathematical Formulation

We demonstrate a simplistic case of using a linear array of frequency combs, each of them acts as a cylindrical source of waves generated from a nano-slit as shown in Fig 7.2. These sources are placed at discrete locations with *d* separation, and each two consecutive sources has a change in frequency Δf. The coordinate system used in the mathematical formulation is shown in Fig. 7.3. The far field generated from this array takes the form:

$$E = \sum_{n=-N}^{N} \frac{e^{i(\omega_n t - k_n |r - r_n|)}}{\sqrt{|r - r_n|}} \tag{7.1}$$

where $r_n = (x_n, y_n) = (nd, 0)$, $\omega_n = \omega_0 + n\Delta\omega$ and $k_n = \frac{\omega_n}{c} = k_0 + n\Delta k$.

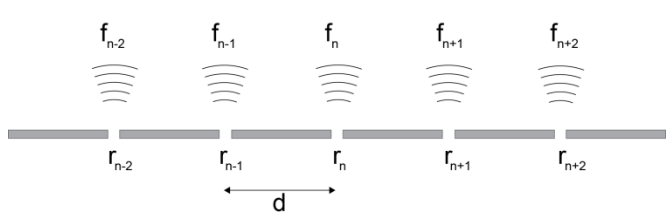

Fig 7.2. Demonstration of phase-locked array of cylindrical waves.

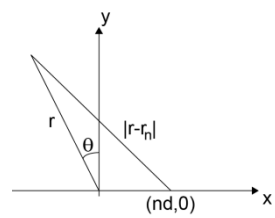

Fig 7.3. Coordinate system used in mathematical formulations.

Using these valid approximations: $\Delta f \ll f_0$, $\Delta\omega \ll \omega_0$, $\Delta k \ll k_0$ and $Nd \ll r$, and by substituting $\left|r - r_n\right| = \sqrt{(r\sin\theta + nd)^2 + r^2\cos^2\theta} \approx r + nd\sin\theta$, we obtain:

$$E \approx \frac{1}{\sqrt{r}} \sum_{n=-N}^{N} e^{i(\omega_n t - k_n(r + nd\sin\theta))} \approx \frac{e^{i(\omega_0 t - k_0 r)}}{\sqrt{r}} \sum_{n=-N}^{N} e^{in(\Delta\omega t - \Delta kr - k_0 d\sin\theta)}$$

The summation on the right hand side is a very famous summation in discrete signal processing[186]:

Let $\Omega = \Delta\omega t - \Delta kr - k_0 d\sin\theta$ and using $\sum_{n=-N}^{N} e^{in\Omega} = \dfrac{\sin\left(\dfrac{(2N+1)\Omega}{2}\right)}{\sin\left(\dfrac{\Omega}{2}\right)}$, we obtain:

$$E \approx \frac{e^{i(\omega_0 t - k_0 r)}}{\sqrt{r}} \frac{\sin\left(\dfrac{\left(2N+1\right)\Omega}{2}\right)}{\sin\left(\dfrac{\Omega}{2}\right)} \tag{7.2}$$

This function has a maximum at $\Omega = 0$ and at integer multiples of 2π. Now we can show that the value at which the summation is maximized corresponds to a rotating beam, and the Ω period of 2π corresponds to a beam steering repetition time of 1/Δf.

$\Omega = 0$ leads to $\Delta\omega t - \Delta kr - k_0 d\sin\theta = 0 \Rightarrow \sin\theta = \left(\dfrac{\Delta\omega}{k_0 d}\right)t - \left(\dfrac{\Delta kr}{k_0 d}\right)$.

The previous equation demonstrates the beam steering action through the time-variation of sinθ with respect to t. The term ($\Delta kr/k_o d$) is due to the time delay between the

source and the distance of measurement *r*. We can always define the time frame such that sinθ = 0 at *t* = 0 by substituting $t \equiv t - \frac{r}{c}$. Therefore, we can modify it as follows:

$$\sin\theta = \left(\frac{\Delta\omega}{k_0 d}\right)t \tag{7.3}$$

Fig. 7.4 shows a specific plot of Eq (7.2) with respect sinθ and *t*. This plot explains the beam steering effect, and also demonstrates important periodicity patterns in time. There is also a periodicity pattern in sinθ. But it should be noticed that sinθ takes only values between -1 and 1, however, in specific cases several values of sinθ can be achieved simultaneously. This corresponds to achieving multiple beams at the same time. All these cases will be explained below.

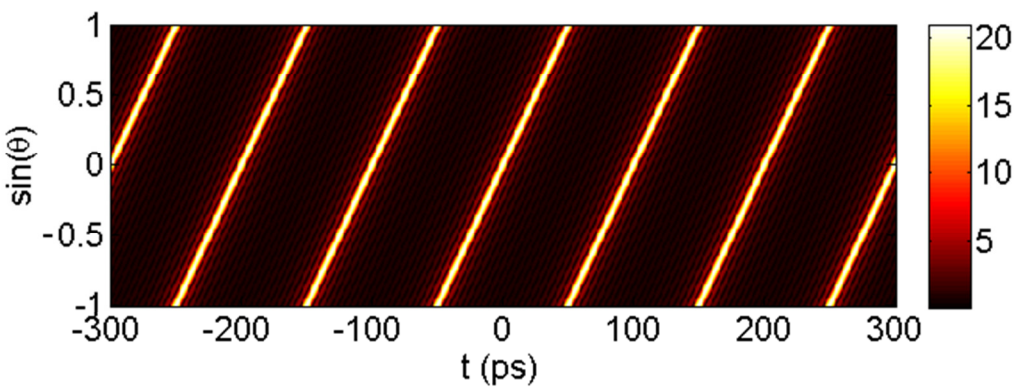

Fig. 7.4. Plot of Eq (7.2) with respect to sinθ and *t*. We have substituted $\lambda_0 = 1.5\mu m$, $d = 750nm$, $\Delta f = 10GHz$, and used 21 frequency comb lines $(2N + 1 = 21)$.

The periodicity of 2π with respect to Ω imposes a temporal periodicity τ where:

$$\Delta\omega\tau = 2\pi$$

and hence,

$$\tau = \frac{2\pi}{\Delta\omega} = \frac{1}{\Delta f} \tag{7.4}$$

Also, the period of 2π in Ω may cause multiple values of θ corresponding to multiple beams. We can guarantee that we have a single beam if only a single value of sinθ lies in the interval [-1,1]. This requires:

$$2k_0 d < 2\pi$$

Or equivalently,

$$d < \frac{\lambda_0}{2}$$

As a result, we obtain the following relation for the angle of beam with respect to time given by:

$$\sin\theta = \left(\frac{\Delta\omega}{k_0 d}\right)t \text{ for } -\frac{\tau}{2} < t < \frac{\tau}{2} \tag{7.5}$$

and the function is periodic with a period of τ = 1/Δf. If sinθ reaches 1 at t< τ/2, then the angle of view covers all the angles, but we get a dead time zone. The curves below demonstrate these different cases:

Case 1: $\frac{\Delta\omega\tau}{2k_0 d} > 1 \Rightarrow d < \frac{\lambda_0}{2}$

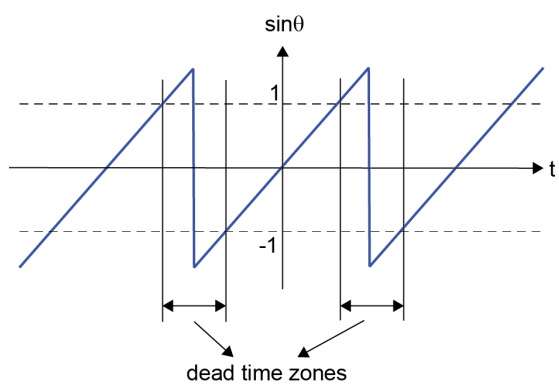

Fig. 7.5. Beam steering with $d < \lambda_0 / 2$. In this case, the angle of view is 180^0, and we get a dead time zone with no beam.

Case 2: $\frac{\Delta\omega\tau}{2k_0 d} = 1 \Rightarrow d = \frac{\lambda_0}{2}$

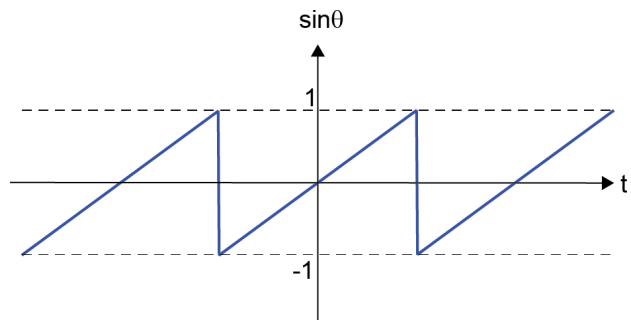

Fig. 7.6. Beam steering with $d = \lambda_0 / 2$. In this case the beam is adjusted to exist at all the times with an angle of view 180^0.

We are not interested in the case where $d > \lambda_0 / 2$ since we have already shown that it doesn't correspond to a case where we have a single beam.

Now, we demonstrate simulation results for these different cases. In the following figures, we simulate the response of an array of cylindrical sources describes by Eq (7.1)

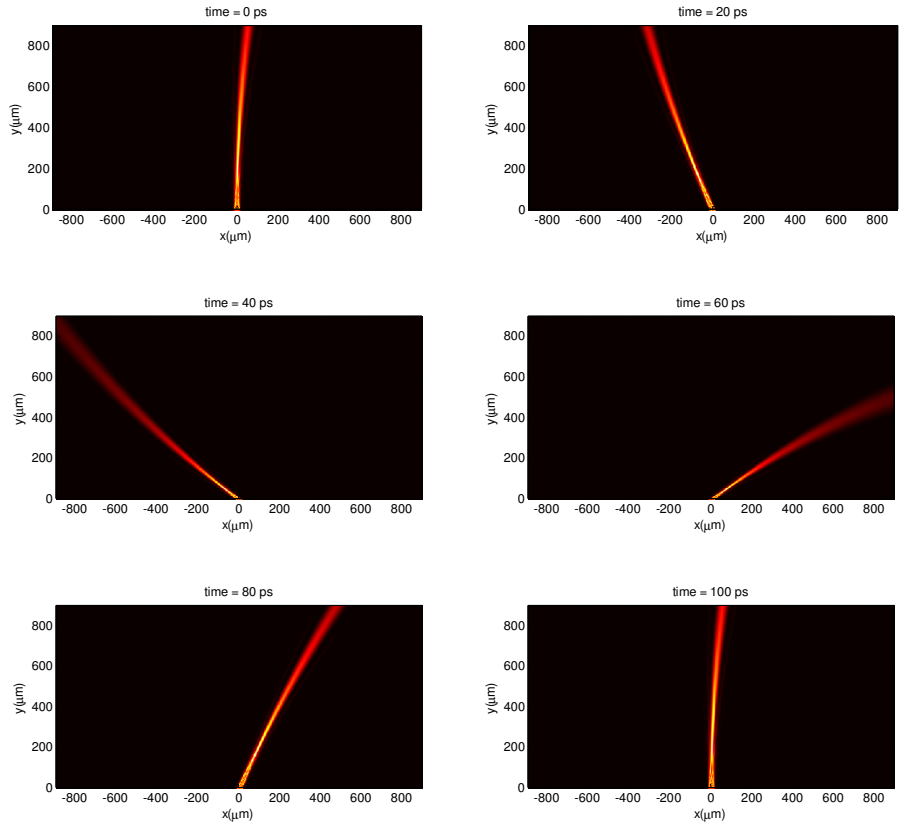

Fig. 7.7. Simulation result for beam steering with $d = \lambda_0 / 2$. In this case the beam is adjusted to exist at all the times with an angle of view 180^0. We have substituted $\lambda_0 = 1.5\mu m$, $d = 750nm$, $\Delta f = 10GHz$, and used 41 frequency comb lines ($2N + 1 = 41$). Simulation results show light intensity at various time instants calculated according to Eq (7.1).

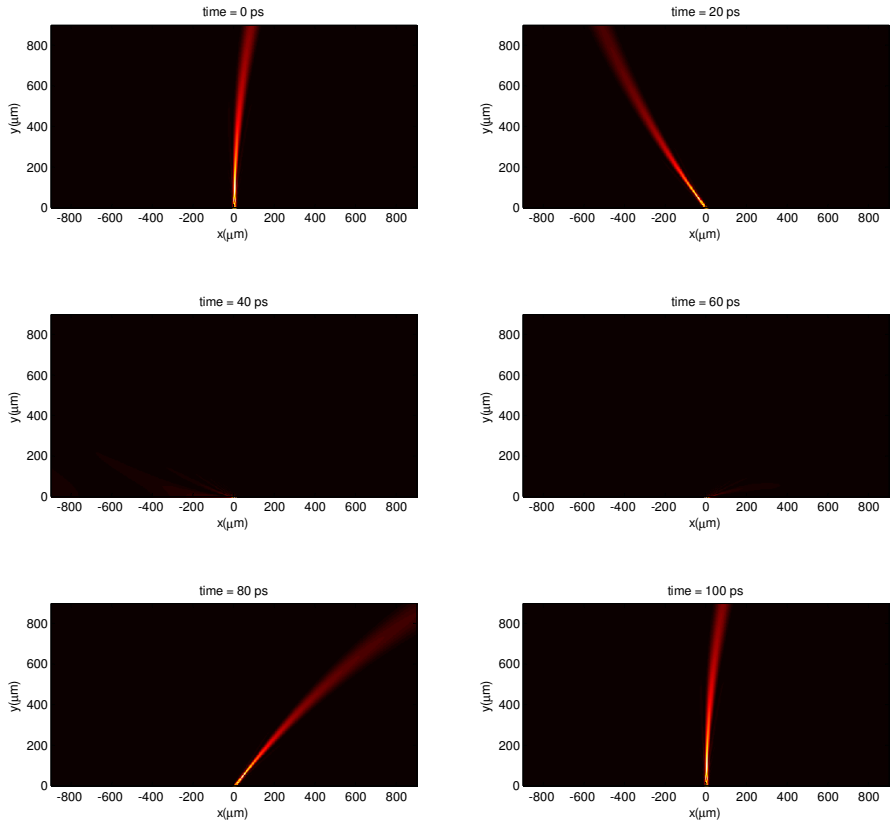

Fig. 7.8. Simulation result for beam steering with $d < \lambda_0 / 2$. In this case, the angle of view is 180^0, and we get a dead time zone with no beam. We have substituted $\lambda_0 = 1.5\mu m$, $d = 500nm$, $\Delta f = 10GHz$, and used 41 frequency comb lines $(2N + 1 = 41)$. Simulation results show light intensity at various time instants calculated according to Eq (7.1).

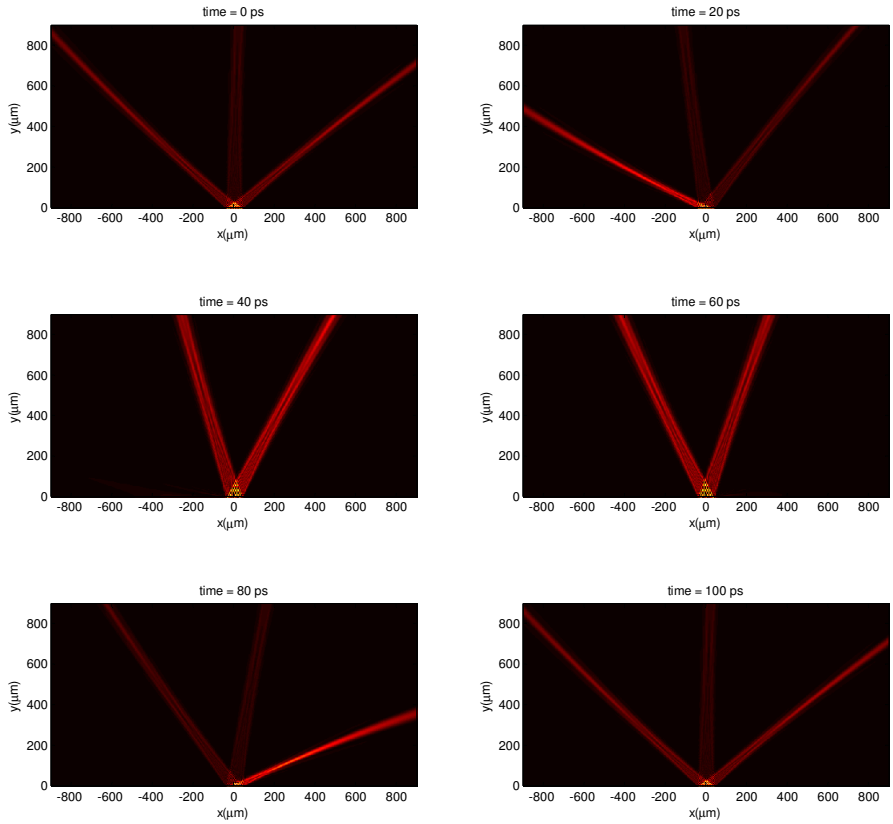

Fig. 7.9. Simulation result for beam steering with $d < \lambda_0 / 2$. In this case, simultaneous beams are generated at the same time at different angles. We have substituted $\lambda_0 = 1.5\mu m$, $d = 500nm$, $\Delta f = 10GHz$, and used 41 frequency comb lines ($2N + 1 = 41$). Simulation results show light intensity at various time instants calculated according to Eq (7.1).

7.4 Possible implementation and experimentation schemes

Ultrashort pulses can provide the source of mode-locked spectral components that interfere together to obtain beam steering. We can utilize the structure of the pulse shaper in which the first stage is composed of a blazed grating and a focusing lens used to decompose the spectral component in space at the focal plane. We will not use the second stage of the pulse shaper which refocuses all the spectral components at the same spot. Instead, we place a nano-slit array at the focal plane, so that each spectral component scatters and plays as a new omni-directional point source (cylindrical source)

independent on the previous beam direction. The interference of these cylindrical waves will obtained the rotating laser beam.

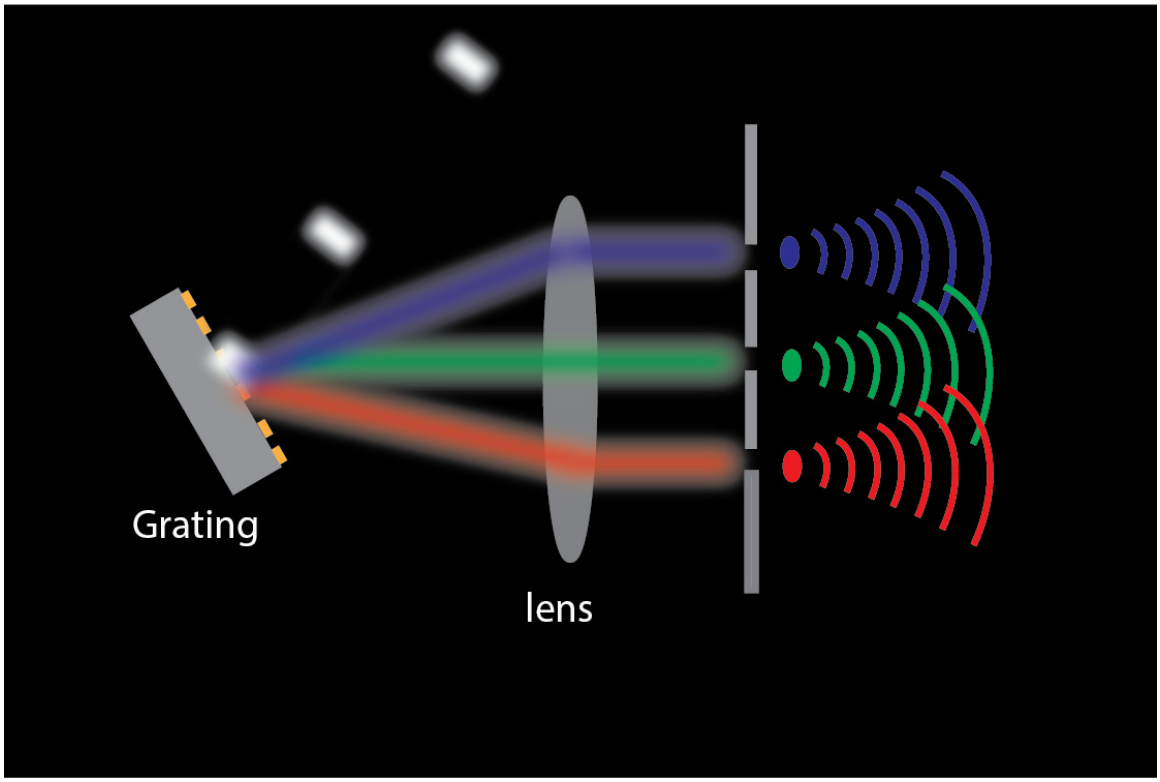

Fig. 7.10. Possible implementation of a beam steering setup. An incident ultrashort pulse is spectrally resolved using a grating, and a lens is used to direct focus spectral components to an array of nano-slits that operate as a secondary sources of omni-directional cylindrical waves.

As a consequence, we redistribute the interference of the spectral components. For the input ultrashort pulse, these components are interfering in time only to compose the ultra-narrow time pulse, but for the output, the interference is in space and time together to generate laser beam steering.

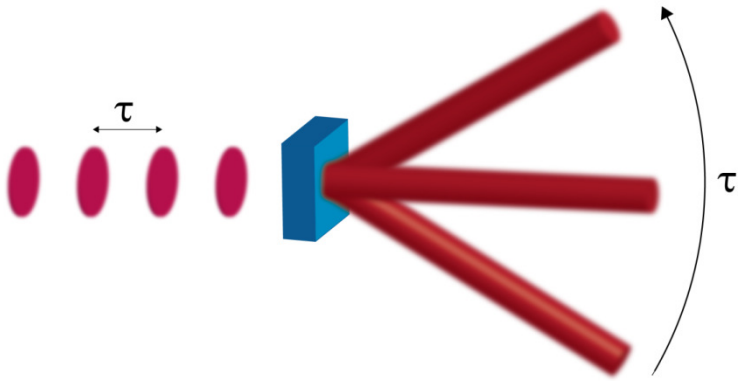

Fig. 7.11. Conceptual schematic of an ultrafast laser beam steering device. Spectral components of incident ultrashort pulse are redistributed to interfere in space and time together to produce a rotating beam.

Experimentation of the beam steering action can be done using a cross-correlator setup (or $g^{(2)}(t)$ measurement) as shown in the figure below.

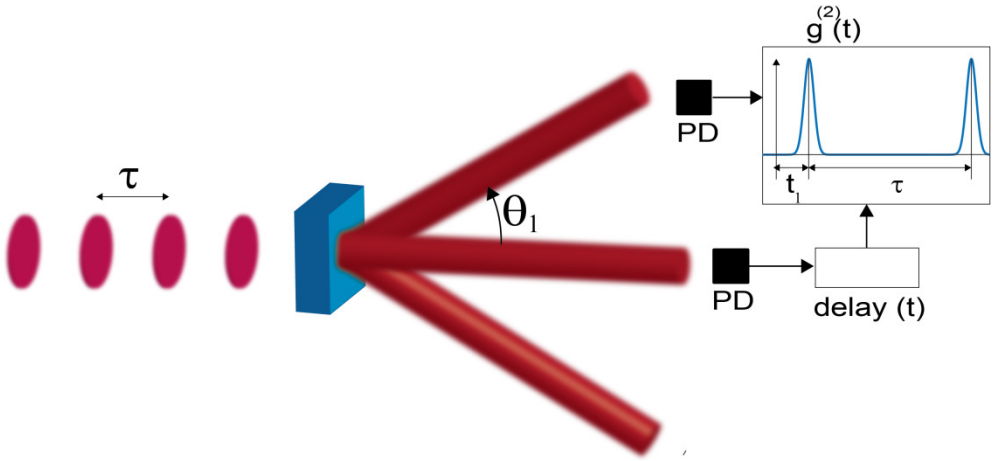

Fig. 7.12. Possible experimentation of the beam steering action. The correlation between the two detectors is maximum when the tuned delay is matched to the time the beam takes to rotate between the two detectors. The location of the maximum should be periodic with a period τ.

We should fix one of the 2 detectors at the normal direction ($\theta = 0^0$) and the other beam at an arbitrary angle θ_1, and we change the delay τ_1 in one of the arm until we obtain a maximum correlation at a specific delay t_1 corresponding to the equation:

$$\sin\theta_1 = \left(\frac{\Delta\omega}{k_0 d}\right) t_1 \tag{7.6}$$

In addition, the correlation peak should be repeated at values $t_1+n\tau$ where n is an integer and τ is the repetition period of the ultrashort pulses. Experimentation is then repeated for several values of θ_1. For each of these values, the corresponding value of t_1 is obtained, and then we fit the data to Eq (7.6) to check that it holds and that it is periodic with the period τ.

7.5 Conclusion

A novel methodology of generating an ultrafast steering beam is introduced. It integrates spatial intereference obtained with nano-structured metasurfaces with temporal interference technique used in pulse shaping of utrafast pulses. A mathematical formulation is derived with supporting numerical simulations. Proposed schemes for implementation and experimentation are introduced.

8. CONCLUSION

To summarize, we have studied various topics in photonic metasurfaces. Several contributions to the field of space-gradient and time-gradient metasurfaces have been done in this thesis, including

1. Bianisotropic models of plasmonic nano-antennas are developed to understand the light-matter interaction inside the metasurface. The model also accounts for the role of symmetry breaking inside the nanostructure and its effect on the waves. It has also been implemented to develop an FDFD solver. A simulation is performed to a phase gradient metasurface with the bianisotropic approximation, and good agreement is obtained with a finite element simulation of the exact nano-sturucture.
2. Metasurfaces utilizing photonic spin Hall effect are implemented to operate as a circular dichroism spectrometer. These operations are obtained through phase gradient metasurfaces which have a differential response to right and left circularly polarized incident light. To overcome the power efficiency limitation, gap-plasmonic antennas are used. Their dimensions are optimized such that all the reflected power of circularly polarized light is controlled by the geometric phase induced by the orientation of the antennas. This has enhanced the power efficiency by an order of magnitude. A circular dichroism spectrometer is also implemented using this technology with 40% power efficiency in the NIR region.
3. We designed and implemented a metasurface based optical rotator. The chiral response in these metasurfaces is not achieved using chiral antennas, but rather obtained through the coherent response of the array. Successful rotation of linearly polarized light by 45^0 is achieved using a metasurface with $\lambda/50$ thickness. The structure is also implemented using gap-plasmonic antennas to

enhance the power efficiency by an order of magnitude. A circular dichroism spectrometer is also implemented using this technology with 40% power efficiency in the NIR region.

4. We design novel nano-cavities with metasurface based mirrors. This novel approach dramatically changes the constraints on the size and capabilities of conventional cavities. This effect is important for enhancement of spontaneous emission enabled by Purcell's effect
5. The impact of time-gradient metasurfaces in developing non-reciprocal Snell's relation of light flow is studied. Snell's law relates the angles of incidence and refraction for light passing through an interface between two media. It is built on two fundamental constraints: the conservation of tangential momentum and the conservation of energy. By relaxing the classical Snell's law photon momentum conservation constraint when using space-gradient phase discontinuities, optical metasurfaces enabled an entirely new class of ultrathin optical devices. Here, we show that by eradicating the photon energy conservation constraint when introducing time-gradient phase discontinuities, we can further empower the area of flat photonics and obtain a new genus of optical devices. With this approach, classical Snell's relations are developed into a more universal form not limited by Lorentz reciprocity, hence, meeting all the requirements for building magnetic-free optical isolators. Furthermore, photons experience inelastic interaction with time-gradient metasurfaces, which modifies photonic energy eigenstates and results in a Doppler-like wavelength shift. Consequently, metasurfaces with both space- and time-gradients can have a strong impact on a plethora of photonic applications and provide versatile control over the physical properties of light.
6. We introduced a novel technique of integrating metasurface based devices with ultrafast technology to enable ultrafast laser beam steering. We integrate spatial interference methodology delivered by metasurfaces and temporal interference of phase-locked frequency-comb provided by ultrafast technology to obtain a time-dependent metasurface response which is ultrafast. This methodology enables

beam steering with a hundred picosecond period which is four orders of magnitude faster than state-of-the-art beam steering technologies based on phase-modulating array elements.

LIST OF REFERENCES

LIST OF REFERENCES

[1] R. Shelby, D. Smith, and S. Schultz, "Experimental verification of a negative index of refraction," *Science,* vol. 292, pp. 77-79, 2001.

[2] V. M. Shalaev, W. Cai, U. K. Chettiar, H.-K. Yuan, A. K. Sarychev, V. P. Drachev, and A. V. Kildishev, "Negative index of refraction in optical metamaterials," *Optics Letters,* vol. 30, pp. 3356-3358, 2005.

[3] S. Zhang, W. Fan, N. Panoiu, K. Malloy, R. Osgood, and S. Brueck, "Experimental demonstration of near-infrared negative-index metamaterials," *Physical review letters,* vol. 95, p. 137404, 2005.

[4] G. Dolling, M. Wegener, C. M. Soukoulis, and S. Linden, "Negative-index metamaterial at 780 nm wavelength," *Optics Letters,* vol. 32, pp. 53-55, 2007.

[5] W. Cai, U. K. Chettiar, H.-K. Yuan, V. C. de Silva, A. V. Kildishev, V. P. Drachev, and V. M. Shalaev, "Metamagnetics with rainbow colors," *Optics Express,* vol. 15, pp. 3333-3341, 2007.

[6] S. Gennady and A. U. Yaroslav, "Negative index meta-materials based on two-dimensional metallic structures," *Journal of Optics A: Pure and Applied Optics,* vol. 8, p. S122, 2006.

[7] J. B. Pendry, "Negative refraction makes a perfect lens," *Physical review letters,* vol. 85, pp. 3966-3969, 2000.

[8] D. Schurig, J. Mock, B. Justice, S. A. Cummer, J. Pendry, A. Starr, and D. Smith, "Metamaterial electromagnetic cloak at microwave frequencies," *Science,* vol. 314, pp. 977-980, 2006.

[9] W. Cai, U. K. Chettiar, A. V. Kildishev, and V. M. Shalaev, "Optical cloaking with metamaterials," *Nature photonics,* vol. 1, pp. 224-227, 2007.

[10] Z. Jacob, L. V. Alekseyev, and E. Narimanov, "Optical Hyperlens: Far-field imaging beyond the diffraction limit," *Optics Express,* vol. 14, pp. 8247-8256, 2006.

[11] A. Salandrino and N. Engheta, "Far-field subdiffraction optical microscopy using metamaterial crystals: Theory and simulations," *Physical Review B,* vol. 74, p. 075103, 2006.

[12] Z. Liu, H. Lee, Y. Xiong, C. Sun, and X. Zhang, "Far-field optical hyperlens magnifying sub-diffraction-limited objects," *Science,* vol. 315, pp. 1686-1686, 2007.

[13] E. E. Narimanov and A. V. Kildishev, "Optical black hole: Broadband omnidirectional light absorber," *Applied Physics Letters,* vol. 95, p. 041106, 2009.

[14] D. A. Genov, S. Zhang, and X. Zhang, "Mimicking celestial mechanics in metamaterials," *Nature Physics,* vol. 5, pp. 687-692, 2009.

[15] Z. Jacob, J.-Y. Kim, G. Naik, A. Boltasseva, E. Narimanov, and V. Shalaev, "Engineering photonic density of states using metamaterials," *Applied Physics B,* vol. 100, pp. 215-218, 2010.

[16] A. Poddubny, I. Iorsh, P. Belov, and Y. Kivshar, "Hyperbolic metamaterials," *Nature photonics,* vol. 7, pp. 948-957, 2013.

[17] V. P. Drachev, V. A. Podolskiy, and A. V. Kildishev, "Hyperbolic metamaterials: new physics behind a classical problem," *Optics Express,* vol. 21, pp. 15048-15064, 2013.

[18] A. V. Kildishev, A. Boltasseva, and V. M. Shalaev, "Planar photonics with metasurfaces," *Science,* vol. 339, 2013.

[19] N. Yu, P. Genevet, M. A. Kats, F. Aieta, J.-P. Tetienne, F. Capasso, and Z. Gaburro, "Light propagation with phase discontinuities: generalized laws of reflection and refraction," *Science,* vol. 334, pp. 333-337, 2011.

[20] X. Ni, N. K. Emani, A. V. Kildishev, A. Boltasseva, and V. M. Shalaev, "Broadband light bending with plasmonic nanoantennas," *Science,* vol. 335, pp. 427-427, 2012.

[21] Z. e. Bomzon, G. Biener, V. Kleiner, and E. Hasman, "Space-variant Pancharatnam-Berry phase optical elements with computer-generated subwavelength gratings," *Optics Letters,* vol. 27, pp. 1141-1143, 2002.

[22] E. Hasman, V. Kleiner, G. Biener, and A. Niv, "Polarization dependent focusing lens by use of quantized Pancharatnam–Berry phase diffractive optics," *Applied Physics Letters,* vol. 82, pp. 328-330, 2003.

[23] N. Yu, P. Genevet, M. A. Kats, F. Aieta, J. P. Tetienne, F. Capasso, and Z. Gaburro, "Light propagation with phase discontinuities: generalized laws of reflection and refraction," in *Science* vol. 334, ed, pp. 333-337, 2011

[24] P. R. West, S. Ishii, G. V. Naik, N. K. Emani, V. M. Shalaev, and A. Boltasseva, "Searching for better plasmonic materials," *Laser & Photonics Reviews,* vol. 4, pp. 795-808, 2010.

[25] U. Guler, A. V. Kildishev, A. Boltasseva, and V. M. Shalaev, "Plasmonics on the slope of enlightenment: the role of transition metal nitrides," *Faraday discussions,* vol. 178, pp. 71-86, 2015.

[26] C. Pfeiffer, N. K. Emani, A. M. Shaltout, A. Boltasseva, V. M. Shalaev, and A. Grbic, "Efficient Light Bending with Isotropic Metamaterial Huygens' Surfaces," *Nano Letters,* vol. 14, pp. 2491-2497, 2014.

[27] F. Aieta, P. Genevet, M. A. Kats, N. Yu, R. Blanchard, Z. Gaburro, and F. Capasso, "Aberration-free ultra-thin flat lenses and axicons at telecom wavelengths based on plasmonic metasurfaces," *Nano Letters,* 2012.

[28] X. Ni, S. Ishii, A. V. Kildishev, and V. M. Shalaev, "Ultra-thin, planar, Babinet-inverted plasmonic metalenses," *Light: Science & Applications,* vol. 2, p. e72, 2013.

[29] X. Chen, L. Huang, H. Mühlenbernd, G. Li, B. Bai, Q. Tan, G. Jin, C.-W. Qiu, S. Zhang, and T. Zentgraf, "Dual-polarity plasmonic metalens for visible light," *Nature Communications,* vol. 3, p. 1198, 2012.

[30] W. T. Chen, K.-Y. Yang, C.-M. Wang, Y.-W. Huang, G. Sun, I. D. Chiang, C. Y. Liao, W.-L. Hsu, H. T. Lin, S. Sun, L. Zhou, A. Q. Liu, and D. P. Tsai, "High-Efficiency Broadband Meta-Hologram with Polarization-Controlled Dual Images," *Nano Letters,* vol. 14, pp. 225-230, 2014.

[31] S. Larouche, Y.-J. Tsai, T. Tyler, N. M. Jokerst, and D. R. Smith, "Infrared metamaterial phase holograms," *Nature materials,* vol. 11, pp. 450-454, 2012.

[32] J. Lin, P. Genevet, M. A. Kats, N. Antoniou, and F. Capasso, "Nanostructured holograms for broadband manipulation of vector beams," *Nano Letters,* vol. 13, pp. 4269-4274, 2013.

[33] Y. Montelongo, J. O. Tenorio-Pearl, C. Williams, S. Zhang, W. I. Milne, and T. D. Wilkinson, "Plasmonic nanoparticle scattering for color holograms," *Proceedings of the National Academy of Sciences,* vol. 111, pp. 12679-12683, 2014.

[34] X. Ni, A. V. Kildishev, and V. M. Shalaev, "Metasurface holograms for visible light," *Nature Communications,* vol. 4, 2013.

[35] Y. Yang, W. Wang, P. Moitra, I. I. Kravchenko, D. P. Briggs, and J. Valentine, "Dielectric meta-reflectarray for broadband linear polarization conversion and optical vortex generation," *Nano Letters,* vol. 14, pp. 1394-1399, 2014.

[36] N. Yu, F. Aieta, P. Genevet, M. A. Kats, Z. Gaburro, and F. Capasso, "A broadband, background-free quarter-wave plate based on plasmonic metasurfaces," *Nano Letters,* vol. 12, pp. 6328-6333, 2012.

[37] A. Pors and S. I. Bozhevolnyi, "Efficient and broadband quarter-wave plates by gap-plasmon resonators," *Optics Express,* vol. 21, pp. 2942-2952, 2013.

[38] Z. Zhu, C. Guo, K. Liu, W. Ye, X. Yuan, B. Yang, and T. Ma, "Metallic nanofilm half-wave plate based on magnetic plasmon resonance," *Optics Letters,* vol. 37, pp. 698-700, 2012.

[39] F. Ding, Z. Wang, S. He, V. M. Shalaev, and A. V. Kildishev, "Broadband High-Efficiency Half-Wave Plate: A Supercell-Based Plasmonic Metasurface Approach," *ACS nano,* vol. 9, pp. 4111-4119, 2015.

[40] J. Liu, A. M. Shaltout, X. Ni, V. M. Shalaev, and A. V. Kildishev, "Experimental validation of a new bianisotropic parameter retrieval technique using plasmonic metasurfaces made of V-shape antennas," in *SPIE NanoScience+ Engineering*, pp. 88060F-88060F-10, 2013.

[41] C. Pfeiffer and A. Grbic, "Bianisotropic Metasurfaces for Optimal Polarization Control: Analysis and Synthesis," *Physical Review Applied,* vol. 2, p. 044011, 2014.

[42] A. Shaltout, V. Shalaev, and A. Kildishev, "Homogenization of bi-anisotropic metasurfaces," *Optics Express,* vol. 21, pp. 21941-21950, 2013.

[43] A. Papakostas, A. Potts, D. Bagnall, S. Prosvirnin, H. Coles, and N. Zheludev, "Optical manifestations of planar chirality," *Physical review letters,* vol. 90, p. 107404, 2003.

[44] E. Plum, X.-X. Liu, V. Fedotov, Y. Chen, D. Tsai, and N. Zheludev, "Metamaterials: optical activity without chirality," *Physical review letters,* vol. 102, p. 113902, 2009.

[45] E. Plum, J. Zhou, J. Dong, V. Fedotov, T. Koschny, C. Soukoulis, and N. Zheludev, "Metamaterial with negative index due to chirality," *Physical Review B,* vol. 79, p. 035407, 2009.

[46] S. Prosvirnin and N. Zheludev, "Polarization effects in the diffraction of light by a planar chiral structure," *Physical Review E,* vol. 71, p. 037603, 2005.

[47] S. L. Prosvirnin and N. I. Zheludev, "Analysis of polarization transformations by a planar chiral array of complex-shaped particles," *Journal of Optics A: Pure and Applied Optics,* vol. 11, p. 074002, 2009.

[48] Y. Svirko, N. Zheludev, and M. Osipov, "Layered chiral metallic microstructures with inductive coupling," *Applied Physics Letters,* vol. 78, pp. 498-500, 2001.

[49] A. Shaltout, J. Liu, V. M. Shalaev, and A. V. Kildishev, "Optically Active Metasurface with Non-Chiral Plasmonic Nanoantennas," *Nano Letters,* 2014.

[50] M. V. Berry, "Quantal phase factors accompanying adiabatic changes," in *Proceedings of the Royal Society of London A: Mathematical, Physical and Engineering Sciences*, pp. 45-57, 1984.

[51] N. Shitrit, I. Bretner, Y. Gorodetski, V. Kleiner, and E. Hasman, "Optical spin Hall effects in plasmonic chains," *Nano Letters,* vol. 11, pp. 2038-2042, 2011.

[52] N. Shitrit, I. Yulevich, E. Maguid, D. Ozeri, D. Veksler, V. Kleiner, and E. Hasman, "Spin-optical metamaterial route to spin-controlled photonics," *Science,* vol. 340, pp. 724-726, 2013.

[53] X. Ling, X. Zhou, W. Shu, H. Luo, and S. Wen, "Realization of tunable photonic spin Hall effect by tailoring the Pancharatnam-Berry phase," *Scientific reports,* vol. 4, 2014.

[54] A. Pors, M. G. Nielsen, and S. I. Bozhevolnyi, "Plasmonic metagratings for simultaneous determination of Stokes parameters," *Optica,* vol. 2, pp. 716-723, 2015.

[55] J. Müller, K. Leosson, and F. Capasso, "Ultra-compact In-Line Scattering Polarimetry," *arXiv preprint arXiv:1509.05484,* 2015.

[56] A. Shaltout, J. Liu, A. Kildishev, and V. Shalaev, "Photonic spin Hall effect in gap-plasmon metasurfaces for on-chip chiroptical spectroscopy," *Optica,* vol. 2, pp. 860-863, 2015.

[57] C. Pfeiffer and A. Grbic, "Metamaterial Huygens' surfaces: tailoring wave fronts with reflectionless sheets," *Physical review letters,* vol. 110, p. 197401, 2013.

[58] S. Sun, Q. He, S. Xiao, Q. Xu, X. Li, and L. Zhou, "Gradient-index meta-surfaces as a bridge linking propagating waves and surface waves," *Nat Mater,* vol. 11, pp. 426-431, 2012.

[59] S. Sun, K.-Y. Yang, C.-M. Wang, T.-K. Juan, W. T. Chen, C. Y. Liao, Q. He, S. Xiao, W.-T. Kung, and G.-Y. Guo, "High-Efficiency Broadband Anomalous Reflection by Gradient Meta-Surfaces," *Nano Letters,* vol. 12, pp. 6223-6229, 2012.

[60] A. Pors, O. Albrektsen, I. P. Radko, and S. I. Bozhevolnyi, "Gap plasmon-based metasurfaces for total control of reflected light," *Scientific reports,* vol. 3, 2013.

[61] A. Pors, M. G. Nielsen, R. L. Eriksen, and S. I. Bozhevolnyi, "Broadband Focusing Flat Mirrors Based on Plasmonic Gradient Metasurfaces," *Nano Letters,* vol. 13, pp. 829-834, 2013.

[62] A. Pors, M. G. Nielsen, G. D. Valle, M. Willatzen, O. Albrektsen, and S. I. Bozhevolnyi, "Plasmonic metamaterial wave retarders in reflection by orthogonally oriented detuned electrical dipoles," *Optics Letters,* vol. 36, pp. 1626-1628, 2011.

[63] A. E. Krasnok, A. E. Miroshnichenko, P. A. Belov, and Y. S. Kivshar, "All-dielectric optical nanoantennas," *Optics Express,* vol. 20, pp. 20599-20604, 2012.

[64] D. S. Filonov, A. E. Krasnok, A. P. Slobozhanyuk, P. V. Kapitanova, E. A. Nenasheva, Y. S. Kivshar, and P. A. Belov, "Experimental verification of the concept of all-dielectric nanoantennas," *Applied Physics Letters,* vol. 100, p. 201113, 2012.

[65] P. R. West, J. L. Stewart, A. V. Kildishev, V. M. Shalaev, V. V. Shkunov, F. Strohkendl, Y. A. Zakharenkov, R. K. Dodds, and R. Byren, "All-dielectric subwavelength metasurface focusing lens," *Optics Express,* vol. 22, pp. 26212-26221, 2014.

[66] W. E. Nelson, "Electrostatically controlled beam steering device and method," ed: Google Patents, 1993

[67] D. Resler, D. Hobbs, R. Sharp, L. Friedman, and T. Dorschner, "High-efficiency liquid-crystal optical phased-array beam steering," *Optics Letters,* vol. 21, pp. 689-691, 1996.

[68] D. F. Sievenpiper, J. H. Schaffner, H. J. Song, R. Y. Loo, and G. Tangonan, "Two-dimensional beam steering using an electrically tunable impedance surface," *Antennas and Propagation, IEEE Transactions on,* vol. 51, pp. 2713-2722, 2003.

[69] N. R. Smith, D. C. Abeysinghe, J. W. Haus, and J. Heikenfeld, "Agile wide-angle beam steering with electrowetting microprisms," *Optics Express,* vol. 14, pp. 6557-6563, 2006.

[70] O. T. Von Ramm and S. W. Smith, "Beam steering with linear arrays," *Biomedical Engineering, IEEE Transactions on,* pp. 438-452, 1983.

[71] L. Wu, M. Mazilu, and T. F. Krauss, "Beam steering in planar-photonic crystals: from superprism to supercollimator," *Journal of Lightwave Technology,* vol. 21, p. 561, 2003.

[72] K. Scholle, E. Heumann, and G. Huber, "Single mode Tm and Tm, Ho: LuAG lasers for LIDAR applications," *Laser Physics Letters,* vol. 1, p. 285, 2004.

[73] T. Fujii and T. Fukuchi, *Laser remote sensing*: CRC press, 2005.

[74] G. N. Hounsfield, "Computerized transverse axial scanning (tomography): Part 1. Description of system," *The British journal of radiology,* vol. 46, pp. 1016-1022, 1973.

[75] M. E. Durst, G. Zhu, and C. Xu, "Simultaneous spatial and temporal focusing for axial scanning," *Optics Express,* vol. 14, pp. 12243-12254, 2006/12/11 2006.

[76] J.-Y. Ou, E. Plum, L. Jiang, and N. I. Zheludev, "Reconfigurable photonic metamaterials," *Nano Letters,* vol. 11, pp. 2142-2144, 2011.

[77] M. Lapine, D. Powell, M. Gorkunov, I. Shadrivov, R. Marqués, and Y. Kivshar, "Structural tunability in metamaterials," *Applied Physics Letters,* vol. 95, p. 084105, 2009.

[78] Y. H. Fu, A. Q. Liu, W. M. Zhu, X. M. Zhang, D. P. Tsai, J. B. Zhang, T. Mei, J. F. Tao, H. C. Guo, X. H. Zhang, J. H. Teng, N. I. Zheludev, G. Q. Lo, and D. L. Kwong, "A Micromachined Reconfigurable Metamaterial via Reconfiguration of Asymmetric Split-Ring Resonators," *Advanced Functional Materials,* vol. 21, pp. 3589-3594, 2011.

[79] J.-Y. Ou, E. Plum, J. Zhang, and N. I. Zheludev, "An electromechanically reconfigurable plasmonic metamaterial operating in the near-infrared," *Nat Nano,* vol. 8, pp. 252-255, 2013.

[80] K. W. Cheah and G. Li, "Highly Flexible Near-infrared Metamaterials," ed: Google Patents, 2012

[81] A. Di Falco, M. Ploschner, and T. F. Krauss, "Flexible metamaterials at visible wavelengths," *New Journal of Physics,* vol. 12, p. 113006, 2010.

[82] R. Melik, E. Unal, N. K. Perkgoz, C. Puttlitz, and H. V. Demir, "Flexible metamaterials for wireless strain sensing," *Applied Physics Letters,* vol. 95, p. 181105, 2009.

[83] R. Ortuño, C. García-Meca, and A. Martínez, "Terahertz metamaterials on flexible polypropylene substrate," *Plasmonics,* vol. 9, pp. 1143-1147, 2014.

[84] H. Ahn, J.-H. Park, S.-B. Kim, S. H. Jee, Y. S. Yoon, and D.-J. Kim, "Vertically aligned ZnO nanorod sensor on flexible substrate for ethanol gas monitoring," *Electrochemical and Solid-State Letters,* vol. 13, pp. J125-J128, 2010.

[85] A. Di Falco, Y. Zhao, and A. Alú, "Optical metasurfaces with robust angular response on flexible substrates," *Applied Physics Letters,* vol. 99, p. 163110, 2011.

[86] H. Kang, C.-J. Heo, H. C. Jeon, S. Y. Lee, and S.-M. Yang, "Durable Plasmonic Cap Arrays on Flexible Substrate with Real-Time Optical Tunability for High-Fidelity SERS Devices," *ACS applied materials & interfaces,* vol. 5, pp. 4569-4574, 2013.

[87] P. Reader-Harris, A. Ricciardi, T. Krauss, and A. Di Falco, "Optical guided mode resonance filter on a flexible substrate," *Optics Express,* vol. 21, pp. 1002-1007, 2013.

[88] S. Dhar, D. M. Miller, and N. M. Jokerst, "High responsivity, low dark current, heterogeneously integrated thin film Si photodetectors on rigid and flexible substrates," *Optics Express,* vol. 22, pp. 5052-5059, 2014.

[89] L. Zhu, J. Kapraun, J. Ferrara, and C. J. Chang-Hasnain, "Flexible photonic metastructures for tunable coloration," *Optica,* vol. 2, pp. 255-258, 2015/03/20 2015.

[90] Q. Liu, Y. Cui, D. Gardner, X. Li, S. He, and I. I. Smalyukh, "Self-alignment of plasmonic gold nanorods in reconfigurable anisotropic fluids for tunable bulk metamaterial applications," *Nano Letters,* vol. 10, pp. 1347-1353, 2010.

[91] B. J. Roxworthy, A. M. Bhuiya, X. Yu, E. K. Chow, and K. C. Toussaint Jr, "Reconfigurable nanoantennas using electron-beam manipulation," *Nature Communications,* vol. 5, 2014.

[92] J. A. Gordon, C. L. Holloway, J. Booth, S. Kim, Y. Wang, J. Baker-Jarvis, and D. R. Novotny, "Fluid interactions with metafilms/metasurfaces for tuning, sensing, and microwave-assisted chemical processes," *Physical Review B,* vol. 83, p. 205130, 2011.

[93] P. C. Wu, L. Yan, Q. Song, W. Zhu, Z. Wu, D. P. Tsai, F. Capasso, and A.-Q. LIU, "Ultra-broadband Tunable Polarization Converter for Micro-fluidic-meta-surfaces," in *CLEO: Science and Innovations*, p. STh1M. 6, 2015.

[94] L. Yan, P. C. Wu, Q. Song, W. Zhu, Z. Wu, D. P. Tsai, F. Capasso, and L. Ai-Qun, "Dynamic Beam Steering in Micro-fluidic-meta-surface," in *CLEO: QELS_Fundamental Science*, p. FTu1C. 3, 2015.

[95] W. Zhu, Q. Song, L. Yan, W. Zhang, P. Wu, L. Chin, Z. Yang, Z. Shen, T. Deng, and S. Ting, "Tunable flat lens based on microfluidic reconfigurable metasurface," in *Solid-State Sensors, Actuators and Microsystems (TRANSDUCERS), 2015 Transducers-2015 18th International Conference on*, pp. 1989-1992, 2015.

[96] G. Hart, "Modular kirigami," *Proceedings of Bridges Donostia,* 2007.

[97] Y. Hou, R. Neville, F. Scarpa, C. Remillat, B. Gu, and M. Ruzzene, "Graded conventional-auxetic Kirigami sandwich structures: Flatwise compression and edgewise loading," *Composites Part B: Engineering,* vol. 59, pp. 33-42, 2014.

[98] K. Saito, F. Agnese, and F. Scarpa, "A cellular kirigami morphing wingbox concept," *Journal of intelligent material systems and structures,* vol. 22, pp. 935-944, 2011.

[99] S. Sareh and J. Rossiter, "Kirigami artificial muscles with complex biologically inspired morphologies," *Smart Materials and Structures,* vol. 22, p. 014004, 2013.

[100] T. C. Shyu, P. F. Damasceno, P. M. Dodd, A. Lamoureux, L. Xu, M. Shlian, M. Shtein, S. C. Glotzer, and N. A. Kotov, "A kirigami approach to engineering elasticity in nanocomposites through patterned defects," *Nature materials,* 2015.

[101] K. Virk, A. Monti, T. Trehard, M. Marsh, K. Hazra, K. Boba, C. Remillat, F. Scarpa, and I. Farrow, "SILICOMB PEEK Kirigami cellular structures: mechanical response and energy dissipation through zero and negative stiffness," *Smart Materials and Structures,* vol. 22, p. 084014, 2013.

[102] I. V. Shadrivov, A. B. Kozyrev, D. W. van der Weide, and Y. S. Kivshar, "Tunable transmission and harmonic generation in nonlinear metamaterials," *Applied Physics Letters,* vol. 93, p. 161903, 2008.

[103] J. Han, A. Lakhtakia, and C.-W. Qiu, "Terahertz metamaterials with semiconductor split-ring resonators for magnetostatic tunability," *Optics Express,* vol. 16, pp. 14390-14396, 2008.

[104] S. Burokur, J.-P. Daniel, P. Ratajczak, and A. De Lustrac, "Tunable bilayered metasurface for frequency reconfigurable directive emissions," *Applied Physics Letters,* vol. 97, p. 064101, 2010.

[105] J. Chen, M. Badioli, P. Alonso-González, S. Thongrattanasiri, F. Huth, J. Osmond, M. Spasenović, A. Centeno, A. Pesquera, and P. Godignon, "Optical nano-imaging of gate-tunable graphene plasmons," *Nature,* vol. 487, pp. 77-81, 2012.

[106] N. K. Emani, T.-F. Chung, A. V. Kildishev, V. M. Shalaev, Y. P. Chen, and A. Boltasseva, "Electrical modulation of Fano resonance in plasmonic nanostructures using graphene," *Nano Letters,* vol. 14, pp. 78-82, 2013.

[107] N. K. Emani, T.-F. Chung, X. Ni, A. V. Kildishev, Y. P. Chen, and A. Boltasseva, "Electrically tunable damping of plasmonic resonances with graphene," *Nano Letters,* vol. 12, pp. 5202-5206, 2012.

[108] L. Ju, B. Geng, J. Horng, C. Girit, M. Martin, Z. Hao, H. A. Bechtel, X. Liang, A. Zettl, and Y. R. Shen, "Graphene plasmonics for tunable terahertz metamaterials," *Nature Nanotechnology,* vol. 6, pp. 630-634, 2011.

[109] F. Wang, Y. Zhang, C. Tian, C. Girit, A. Zettl, M. Crommie, and Y. R. Shen, "Gate-variable optical transitions in graphene," *Science,* vol. 320, pp. 206-209, 2008.

[110] H. Yan, X. Li, B. Chandra, G. Tulevski, Y. Wu, M. Freitag, W. Zhu, P. Avouris, and F. Xia, "Tunable infrared plasmonic devices using graphene/insulator stacks," *Nature Nanotechnology,* vol. 7, pp. 330-334, 2012.

[111] Y. Yao, M. A. Kats, P. Genevet, N. Yu, Y. Song, J. Kong, and F. Capasso, "Broad electrical tuning of graphene-loaded plasmonic antennas," *Nano Letters,* vol. 13, pp. 1257-1264, 2013.

[112] Y. Yao, M. A. Kats, R. Shankar, Y. Song, J. Kong, M. Loncar, and F. Capasso, "Wide wavelength tuning of optical antennas on graphene with nanosecond response time," *Nano Letters,* vol. 14, pp. 214-219, 2013.

[113] Y. Zhang, T.-T. Tang, C. Girit, Z. Hao, M. C. Martin, A. Zettl, M. F. Crommie, Y. R. Shen, and F. Wang, "Direct observation of a widely tunable bandgap in bilayer graphene," *Nature,* vol. 459, pp. 820-823, 2009.

[114] H.-T. Chen, W. J. Padilla, J. M. Zide, A. C. Gossard, A. J. Taylor, and R. D. Averitt, "Active terahertz metamaterial devices," *Nature,* vol. 444, pp. 597-600, 2006.

[115] W. J. Padilla, A. J. Taylor, C. Highstrete, M. Lee, and R. D. Averitt, "Dynamical electric and magnetic metamaterial response at terahertz frequencies," *Physical review letters,* vol. 96, p. 107401, 2006.

[116] E. Feigenbaum, K. Diest, and H. A. Atwater, "Unity-order index change in transparent conducting oxides at visible frequencies," *Nano Letters,* vol. 10, pp. 2111-2116, 2010.

[117] H.-T. Chen, W. J. Padilla, J. M. O. Zide, S. R. Bank, A. C. Gossard, A. J. Taylor, and R. D. Averitt, "Ultrafast optical switching of terahertz metamaterials fabricated on ErAs/GaAs nanoisland superlattices," *Optics Letters,* vol. 32, pp. 1620-1622, 2007.

[118] D. J. Cho, W. Wu, E. Ponizovskaya, P. Chaturvedi, A. M. Bratkovsky, S.-Y. Wang, X. Zhang, F. Wang, and Y. R. Shen, "Ultrafast modulation of optical metamaterials," *Optics Express,* vol. 17, pp. 17652-17657, 2009.

[119] N. Kinsey, C. DeVault, J. Kim, M. Ferrera, V. M. Shalaev, and A. Boltasseva, "Epsilon-near-zero Al-doped ZnO for ultrafast switching at telecom wavelengths," *Optica,* vol. 2, pp. 616-622, 2015.

[120] A. Shaltout, A. Kildishev, and V. Shalaev, "Time-varying metasurfaces and Lorentz non-reciprocity," *Optical Materials Express,* vol. 5, pp. 2459-2467, 2015.

[121] Y. Hadad, D. L. Sounas, and A. Alu, "Space-time gradient metasurfaces," *Physical Review B,* vol. 92, p. 100304, 2015.
[122] Y. Zhao, M. Belkin, and A. Alù, "Twisted optical metamaterials for planarized ultrathin broadband circular polarizers," *Nature Communications,* vol. 3, p. 870, 2012.
[123] J. Hao, Y. Yuan, L. Ran, T. Jiang, J. A. Kong, C. Chan, and L. Zhou, "Manipulating electromagnetic wave polarizations by anisotropic metamaterials," *Physical review letters,* vol. 99, p. 63908, 2007.
[124] A. Drezet, C. Genet, and T. W. Ebbesen, "Miniature plasmonic wave plates," *Physical review letters,* vol. 101, p. 43902, 2008.
[125] Y. Zhao and A. Alù, "Manipulating light polarization with ultrathin plasmonic metasurfaces," *Physical Review B,* vol. 84, p. 205428, 2011.
[126] A. Shaltout, J. Liu, V. M. Shalaev, and A. V. Kildishev, "Optically Active Metasurface with Non-Chiral Plasmonic Nanoantennas," *Nano Letters,* vol. 14, pp. 4426-4431, 2014.
[127] D. Smith, S. Schultz, P. Markoš, and C. Soukoulis, "Determination of effective permittivity and permeability of metamaterials from reflection and transmission coefficients," *Physical Review B,* vol. 65, p. 195104, 2002.
[128] A. Alù, "First-principles homogenization theory for periodic metamaterials," *Physical Review B,* vol. 84, p. 075153, 2011.

[129] A. V. Kildishev, J. D. Borneman, X. Ni, V. M. Shalaev, and V. P. Drachev, "Bianisotropic Effective Parameters of Optical Metamagnetics and Negative-Index Materials," *Proceedings of the IEEE,* vol. 99, pp. 1691-1700, 2011.
[130] A. Alù, "Restoring the physical meaning of metamaterial constitutive parameters," *Physical Review B,* vol. 83, p. 081102, 2011.
[131] I. V. Lindell and A. J. Viitanen, "Eigenwaves in the general uniaxial bianisotropic medium with symmetric parameter dyadics," *Report No. 148 Helsinki Univ. of Technology, Espoo (Finland). Electromagnetics Lab.,* vol. 1, 1993.
[132] O. Luukkonen, S. I. Maslovski, and S. A. Tretyakov, "A stepwise Nicolson–Ross–Weir-based material parameter extraction method," *Antennas and Wireless Propagation Letters, IEEE,* vol. 10, pp. 1295-1298, 2011.
[133] D.-H. Kwon, D. H. Werner, A. V. Kildishev, and V. M. Shalaev, "Material parameter retrieval procedure for general bi-isotropic metamaterials and its application to optical chiral negative-index metamaterial design," *Optics Express,* vol. 16, pp. 11822-11829, 2008.
[134] R. C. Rumpf, "Simple implementation of arbitrarily shaped total-field/scattered-field regions in finite-difference frequency-domain," *Progress In Electromagnetics Research B,* vol. 36, pp. 221-248, 2012.
[135] N. Berova, K. Nakanishi, and R. Woody, *Circular dichroism: principles and applications*: John Wiley & Sons, 2000.
[136] L. Whitmore and B. A. Wallace, "Protein secondary structure analyses from circular dichroism spectroscopy: methods and reference databases," *Biopolymers,* vol. 89, pp. 392-400, 2008.

[137] T. B. Freedman, X. Cao, R. K. Dukor, and L. A. Nafie, "Absolute configuration determination of chiral molecules in the solution state using vibrational circular dichroism," *Chirality,* vol. 15, pp. 743-758, 2003.
[138] W. C. Johnson Jr, "A circular dichroism spectrometer for the vacuum ultraviolet," *Review of Scientific Instruments,* vol. 42, pp. 1283-1286, 1971.
[139] D. Tsankov, T. Eggimann, and H. Wieser, "Alternative design for improved FT-IR/VCD capabilities," *Applied spectroscopy,* vol. 49, pp. 132-138, 1995.
[140] M. Decker, M. Klein, M. Wegener, and S. Linden, "Circular dichroism of planar chiral magnetic metamaterials," *Optics Letters,* vol. 32, pp. 856-858, 2007.
[141] J. K. Gansel, M. Thiel, M. S. Rill, M. Decker, K. Bade, V. Saile, G. von Freymann, S. Linden, and M. Wegener, "Gold helix photonic metamaterial as broadband circular polarizer," *Science,* vol. 325, pp. 1513-1515, 2009.
[142] S. Zhang, Y.-S. Park, J. Li, X. Lu, W. Zhang, and X. Zhang, "Negative refractive index in chiral metamaterials," *Physical review letters,* vol. 102, p. 023901, 2009.
[143] M. Liu, D. A. Powell, I. V. Shadrivov, and Y. S. Kivshar, "Optical activity and coupling in twisted dimer meta-atoms," *Applied Physics Letters,* vol. 100, p. 111114, 2012.
[144] X. Yin, Z. Ye, J. Rho, Y. Wang, and X. Zhang, "Photonic spin Hall effect at metasurfaces," *Science,* vol. 339, pp. 1405-1407, 2013.
[145] J. Lin, J. B. Mueller, Q. Wang, G. Yuan, N. Antoniou, X.-C. Yuan, and F. Capasso, "Polarization-controlled tunable directional coupling of surface plasmon polaritons," *Science,* vol. 340, pp. 331-334, 2013.
[146] M. Kang, T. Feng, H.-T. Wang, and J. Li, "Wave front engineering from an array of thin aperture antennas," *Optics Express,* vol. 20, pp. 15882-15890, 2012.
[147] S. Sun, K.-Y. Yang, C.-M. Wang, T.-K. Juan, W. T. Chen, C. Y. Liao, Q. He, S. Xiao, W.-T. Kung, G.-Y. Guo, L. Zhou, and D. P. Tsai, "High-Efficiency Broadband Anomalous Reflection by Gradient Meta-Surfaces," *Nano Letters,* vol. 12, pp. 6223-6229, 2012.
[148] G. Zheng, H. Mühlenbernd, M. Kenney, G. Li, T. Zentgraf, and S. Zhang, "Metasurface holograms reaching 80% efficiency," *Nat Nano,* vol. 10, pp. 308-312, 2015.
[149] W. Luo, S. Xiao, Q. He, S. Sun, and L. Zhou, "Photonic Spin Hall Effect with Nearly 100% Efficiency," *Advanced Optical Materials,* 2015.
[150] X. Li, S. Xiao, B. Cai, Q. He, T. J. Cui, and L. Zhou, "Flat metasurfaces to focus electromagnetic waves in reflection geometry," *Optics Letters,* vol. 37, pp. 4940-4942, 2012.
[151] R. C. Jones, "A New Calculus for the Treatment of Optical Systems. IV," *JOSA,* vol. 32, pp. 486-493, 1942.
[152] P. B. Johnson and R.-W. Christy, "Optical constants of the noble metals," *Physical Review B,* vol. 6, p. 4370, 1972.
[153] M. Bosman, L. Zhang, H. Duan, S. F. Tan, C. A. Nijhuis, C. W. Qiu, and J. K. W. Yang, "Encapsulated Annealing: Enhancing the Plasmon Quality Factor in Lithographically–Defined Nanostructures," *Sci. Rep.,* vol. 4, 2014.
[154] L. D. Barron, *Molecular light scattering and optical activity*: Cambridge University Press, 2004.

[155] M. M. Green, C. Andreola, B. Munoz, M. P. Reidy, and K. Zero, "Macromolecular stereochemistry: a cooperative deuterium isotope effect leading to a large optical rotation," *Journal of the American Chemical Society,* vol. 110, pp. 4063-4065, 1988.

[156] G. D. Fasman, *Handbook of Biochemistry and Molecular Biology: Physical and Chemical Data* vol. 2: CRC press, 1976.

[157] A. Glazer and K. Stadnicka, "On the origin of optical activity in crystal structures," *Journal of applied crystallography,* vol. 19, pp. 108-122, 1986.

[158] C. H. Bennett and G. Brassard, "Quantum cryptography: Public key distribution and coin tossing," in *Proceedings of IEEE International Conference on Computers, Systems and Signal Processing*, p. 8, 1984.

[159] B. Wang, J. Zhou, T. Koschny, and C. M. Soukoulis, "Nonplanar chiral metamaterials with negative index," *Applied Physics Letters,* vol. 94, pp. 151112-151112-3, 2009.

[160] T. Li, H. Liu, T. Li, S. Wang, F. Wang, R. Wu, P. Chen, S. Zhu, and X. Zhang, "Magnetic resonance hybridization and optical activity of microwaves in a chiral metamaterial," *Applied Physics Letters,* vol. 92, pp. 131111-131111-3, 2008.

[161] S. Zhang, J. Zhou, Y.-S. Park, J. Rho, R. Singh, S. Nam, A. K. Azad, H.-T. Chen, X. Yin, and A. J. Taylor, "Photoinduced handedness switching in terahertz chiral metamolecules," *Nature Communications,* vol. 3, p. 942, 2012.

[162] D. K. Gramotnev and S. I. Bozhevolnyi, "Plasmonics beyond the diffraction limit," *Nature photonics,* vol. 4, pp. 83-91, 2010.

[163] V. M. Shalaev, "Optical negative-index metamaterials," *Nature photonics,* vol. 1, pp. 41-48, 2007.

[164] E. M. Purcell, "Spontaneous Emission Probabilities at Radio Frequencies," *Physical Review,* vol. 69, pp. 681-681, 1946.

[165] M. Khajavikhan, A. Simic, M. Katz, J. Lee, B. Slutsky, A. Mizrahi, V. Lomakin, and Y. Fainman, "Thresholdless nanoscale coaxial lasers," *Nature,* vol. 482, pp. 204-207, 2012.

[166] N. Engheta, "An idea for thin subwavelength cavity resonators using metamaterials with negative permittivity and permeability," *Antennas and Wireless Propagation Letters, IEEE,* vol. 1, pp. 10-13, 2002.

[167] C. Holloway, D. Love, E. Kuester, A. Salandrino, and N. Engheta, "Sub-wavelength resonators: on the use of metafilms to overcome the $\lambda/2$ size limit," *IET microwaves, antennas & propagation,* vol. 2, pp. 120-129, 2008.

[168] V. Fedoseyev, "Conservation laws and transverse motion of energy on reflection and transmission of electromagnetic waves," *Journal of Physics A: Mathematical and General,* vol. 21, p. 2045, 1988.

[169] L. D. Landau, J. Bell, M. Kearsley, L. Pitaevskii, E. Lifshitz, and J. Sykes, *Electrodynamics of continuous media* vol. 8: elsevier, 1984.

[170] S. Fan, R. Baets, A. Petrov, Z. Yu, J. D. Joannopoulos, W. Freude, A. Melloni, M. Popović, M. Vanwolleghem, and D. Jalas, "Comment on “Nonreciprocal light propagation in a silicon photonic circuit”," *Science,* vol. 335, pp. 38-38, 2012.

[171] D. Jalas, A. Petrov, M. Eich, W. Freude, S. Fan, Z. Yu, R. Baets, M. Popovic, A. Melloni, and J. D. Joannopoulos, "What is—and what is not—an optical isolator," *Nat. Photonics,* vol. 7, pp. 579-582, 2013.
[172] T. J. Kippenberg and K. J. Vahala, "Cavity optomechanics: back-action at the mesoscale," *Science,* vol. 321, pp. 1172-1176, 2008.
[173] J. Chan, T. M. Alegre, A. H. Safavi-Naeini, J. T. Hill, A. Krause, S. Gröblacher, M. Aspelmeyer, and O. Painter, "Laser cooling of a nanomechanical oscillator into its quantum ground state," *Nature,* vol. 478, pp. 89-92, 2011.
[174] Y. Shi, Z. Yu, and S. Fan, "Limitations of nonlinear optical isolators due to dynamic reciprocity," *Nature photonics,* vol. 9, pp. 388-392, 2015.
[175] Z. Yu and S. Fan, "Complete optical isolation created by indirect interband photonic transitions," *Nature photonics,* vol. 3, pp. 91-94, 2009.
[176] H. Lira, Z. Yu, S. Fan, and M. Lipson, "Electrically driven nonreciprocity induced by interband photonic transition on a silicon chip," *Physical review letters,* vol. 109, p. 033901, 2012.
[177] L. D. Tzuang, K. Fang, P. Nussenzveig, S. Fan, and M. Lipson, "Non-reciprocal phase shift induced by an effective magnetic flux for light," *Nature photonics,* vol. 8, pp. 701-705, 2014.
[178] D. L. Sounas, C. Caloz, and A. Alù, "Giant non-reciprocity at the subwavelength scale using angular momentum-biased metamaterials," *Nature Communications,* vol. 4, 2013.
[179] G. Lerosey, J. De Rosny, A. Tourin, A. Derode, G. Montaldo, and M. Fink, "Time reversal of electromagnetic waves," *Physical review letters,* vol. 92, p. 193904, 2004.
[180] J. Pendry, "Time reversal and negative refraction," *Science,* vol. 322, pp. 71-73, 2008.
[181] A. R. Katko, S. Gu, J. P. Barrett, B.-I. Popa, G. Shvets, and S. A. Cummer, "Phase conjugation and negative refraction using nonlinear active metamaterials," *Physical review letters,* vol. 105, p. 123905, 2010.
[182] G. Lerosey, J. De Rosny, A. Tourin, and M. Fink, "Focusing beyond the diffraction limit with far-field time reversal," *Science,* vol. 315, pp. 1120-1122, 2007.
[183] A. M. Weiner, "Femtosecond pulse shaping using spatial light modulators," *Review of Scientific Instruments,* vol. 71, pp. 1929-1960, 2000.
[184] P. F. McManamon, T. A. Dorschner, D. L. Corkum, L. J. Friedman, D. S. Hobbs, M. Holz, S. Liberman, H. Q. Nguyen, D. P. Resler, and R. C. Sharp, "Optical phased array technology," *Proceedings of the IEEE,* vol. 84, pp. 268-298, 1996.
[185] F. Verluise, V. Laude, Z. Cheng, C. Spielmann, and P. Tournois, "Amplitude and phase control of ultrashort pulses by use of an acousto-optic programmable dispersive filter: pulse compression and shaping," *Optics Letters,* vol. 25, pp. 575-577, 2000.
[186] A. V. Oppenheim, R. W. Schafer, and J. R. Buck, *Discrete-time signal processing* vol. 2: Prentice-hall Englewood Cliffs, 1989.

VITA

VITA

Amr Shaltout received his B.S. degree from Department of Electrical Engineering at Ain Shams University, Cairo Egypt, in 2003, and Diploma and M.Sc. from the Department of Engineering Physics and Mathematics at Ain Shams University, Cairo Egypt, in 2005 and 2008 respectively. He has worked as a teaching and research assistant in Ain Shans University and in American University in Cairo (on part-time basis) from 2003 till 2009. He also worked in Si-Ware systems, Cairo, Egypt in 2009.

He joined Purdue university in 2010, and he has been working as a research assistant with the Shalaev research group at Birck Nanotechnology Center. His research interests include optical metamaterials and metasurfaces, dynamic metadevices, plasmonics, optical signal processing, optical MEMS, remote sensing and mathematical optimization. He has authored and coauthored the following patents, journal articles and conference abstracts.

Amr Shaltout's publications from his research at Purdue University are:

Patents

1. A. M. Shaltout, A. V. Kildishev, V. M. Shalaev, "Ultra-Small Cavity with Reflecting Metasurfaces", US utility patent application 14/61093, filed Jan 2015.
2. A. M. Shaltout, Sajid Choudhury, A. V. Kildishev, V. M. Shalaev, Alexandra Boltasseva "System for Producing Ultra-thin Color Phase Hologram with Metasurfaces", US provisional patent application 62/159762, filed May 2015.
3. A. M. Shaltout, A. V. Kildishev, V. M. Shalaev, Jingjing Liu, "Sub-Millimeter Real-time Circular Dichroism Spectrometer with Metasurfaces", US provisional patent application 62/188727, filed July 2015.

4. A. M. Shaltout, A. V. Kildishev, V. M. Shalaev, "Time-Varying Metasurface Structure", US provisional patent application 62/191705, filed July 2015.

Peer-reviewed Journal Publications

1. A. M. Shaltout, V. M. Shalaev, and A. V. Kildishev, "Homogenization of Bi-anisotropic Metasurfaces," Optics Express 21 (19), pp. 21941 – 21950, 2013.
2. C. Pfeiffer, N. K. Emani, A. M. Shaltout, A. Boltasseva, V. M. Shalaev and A. Grbic, "Efficient Light Bending with Isotropic Metamaterial Huygens' Surfaces," Nano Letters 14 (5), pp 2491-2497, 2014.
3. A. M. Shaltout, J. Liu, V. M. Shalaev, and, A. V. Kildishev, "Optically Active Metasurface with Non-chiral Plasmonic Nanoantennas," Nano Letters 14 (8), pp 4426-4431, 2014.
4. A. M. Shaltout, J. Liu, A. V. Kildishev, and V. M. Shalaev, "Photonic Spin Hall Effect in Gap-plasmon Metasurfaces for On-Chip Chiroptical Spectroscopy," Optica 2 (10), pp 850-853, 2015.
5. A. M. Shaltout, A. V. Kildishev, and V. M. Shalaev, "Time-Varying Metasurfaces and Lorentz Non-Reciprocity," Optical Materials Express 5 (11), pp 2459-2467, 2015.
6. A. M. Shaltout, A. V. Kildishev, and V. M. Shalaev, "Evolution of Photonic Metasurfaces: From Static to Dynamic," under review, since September 2015.
7. A. M. Shaltout, N. Kinsey, J. Kim, R. Chandrasekar, J. C. Ndukaife, A. Boltasseva, and V. M. Shalaev, "Development of Optical Metasurfaces: Emerging Concepts and New Materials", under review, since November 2015.
8. A. M. Shaltout, J. Kim, A. V. Kildishev, A. Boltasseva, and V. M. Shalaev, "Subwavelength Metasurface Based Nano-cavities", manuscript under preparation.

9. A. M. Shaltout, A. Mohammed, N. Kinsey, D. Wang, A. Boltasseva, A. Shakouri, and V. M. Shalaev, "Metal Nitrides as Transparent Conducting Electrodes", manuscript under preparation.
10. A. M. Shaltout, K. McKinzie, A. Weiner and V. M. Shalaev, "Ultrafast Laser Beam Steering", manuscript under preparation.

Conference Presentations or Proceedings

1. A. V. Kildishev, X. Ni, A. Emadeldin, and V. M. Shalaev, "Plasmonic Metasurfaces for Phase Holography: Bianisotropic Characterization," in The 43nd winter Colloquium on the Physics of Quantum Electronics (PQE), Snowbird, Utah, USA, 2013. (invited)
2. A. M. Shaltout, V. M. Shalaev, and A. V. Kildishev, "Bi-Anisotropic Homogenization of Metasurfaces," ACES 2013 Conference, Monterey, CA, USA, 2013.
3. A. M. Shaltout, J. Liu, A. V. Kildishev, and V. M. Shalaev, "Broadband Optical Chirality Using Ultrathin Metasurface," in *2013 Conference on Lasers and Electro-Optics (CLEO) and Quantum Electronics and Laser Science Conference (QELS)*, San Jose, CA, USA, 2013.
4. J. Liu, A. M. Shaltout, X. Ni, V. M. Shalaev, and A. V. Kildishev, "Experimental validation of a new bianisotropic parameter retrieval technique using plasmonic metasurfaces made of V-shape antennas," in *The SPIE Optics+Photonics 2013 Advance*, San Diego, CA, USA, 2013.
5. A. M. Shaltout, A. V. Kildishev, and V. M. Shalaev, "Waveguides with Hyperbolic Metasurface Claddings", ACES 2014 Conference, Jacksonsville, FL, USA, 2014. (student paper award).
6. J. Liu, A. M. Shaltout, X. Ni, V. M. Shalaev, A. V. Kildishev, "Approximating metasurfaces by bianisotropic tiles" ACES 2014 Conference, Jacksonsville, FL, USA, 2014.
7. C. Pfeiffer, N. K. Emani, A. M. Shaltout, A. Boltasseva, V. M. Shalaev and A. Grbic, "Experimental Huygens' Surface for NIR Wavelengths" in *2014*

Conference on Lasers and Electro-Optics (CLEO) and Quantum Electronics and Laser Science Conference (QELS), San Jose, CA, USA, 2014.

8. A. M. Shaltout, A. V. Kildishev, and V. M. Shalaev, "Compact Subwavelength Cavities Using Reflecting Metasurfaces", in *2014 Conference on Lasers and Electro-Optics (CLEO) and Quantum Electronics and Laser Science Conference (QELS)*, San Jose, CA, USA, 2014.
9. A. M. Shaltout, J. Liu, V. M. Shalaev, and A. V. Kildishev, "Gap-plasmon metasurfaces for circular dichroic spectroscopy and broadband optical activity" SPIE Photonics West, San Francisco, CA, USA 2015.
10. V Babicheva, A. M. Shaltout, M. Shalaginov, S. Ishii, A. Boltasseva, and A. V. Kildishev, "Towards practical realization of plasmonic waveguides cladded by hyperbolic metamaterials," SPIE Photonics West, San Francisco, CA, USA 2015.
11. S. Choudhury, A. M. Shaltout, V. M. Shalaev, A. Boltasseva, and A. V. Kildishev, "Color Hologram Generation Using a Pancharatnam-Berry Phase Manipulating Metasurface," in *2015 Conference on Lasers and Electro-Optics (CLEO) and Quantum Electronics and Laser Science Conference (QELS)*, San Jose, CA, USA, 2015.
12. A. M. Shaltout, V. M. Shalaev, and A. V. Kildishev, "Dual-Band Metasurface Based Nano-Cavities," in *2015 Conference on Lasers and Electro-Optics (CLEO) and Quantum Electronics and Laser Science Conference (QELS)*, San Jose, CA, USA, 2015.
13. V. M. Shalaev, A. M. Shaltout, J. Liu, S. Choudhury, A. Boltasseva, and A.V. Kildishev, "Metasurfaces' Solutions for Polarization Spectroscopy, Optical Activity, Colored Phase Holograms and Compact Nano-cavities," Progress in Electromagnetics Research Symposium (PIERS), Prague, Czech Republic, 2015.
14. A. M. Shaltout, J. Liu, V. M. Shalaev, and, A. V. Kildishev, "Chiroptical Sensing with Plasmonic Metasurfaces," 6th international conference on metamaterials, photonic crystals and plasmonics, New York, NY, USA, 2015.

15. A. M. Shaltout, J. Liu, A. V. Kildishev, and V. M. Shalaev, "Super-Cell Chirality in Gap-Plasmonic Metasurfaces," Material Research Society Fall Meeting, Boston, MA, USA, 2015.